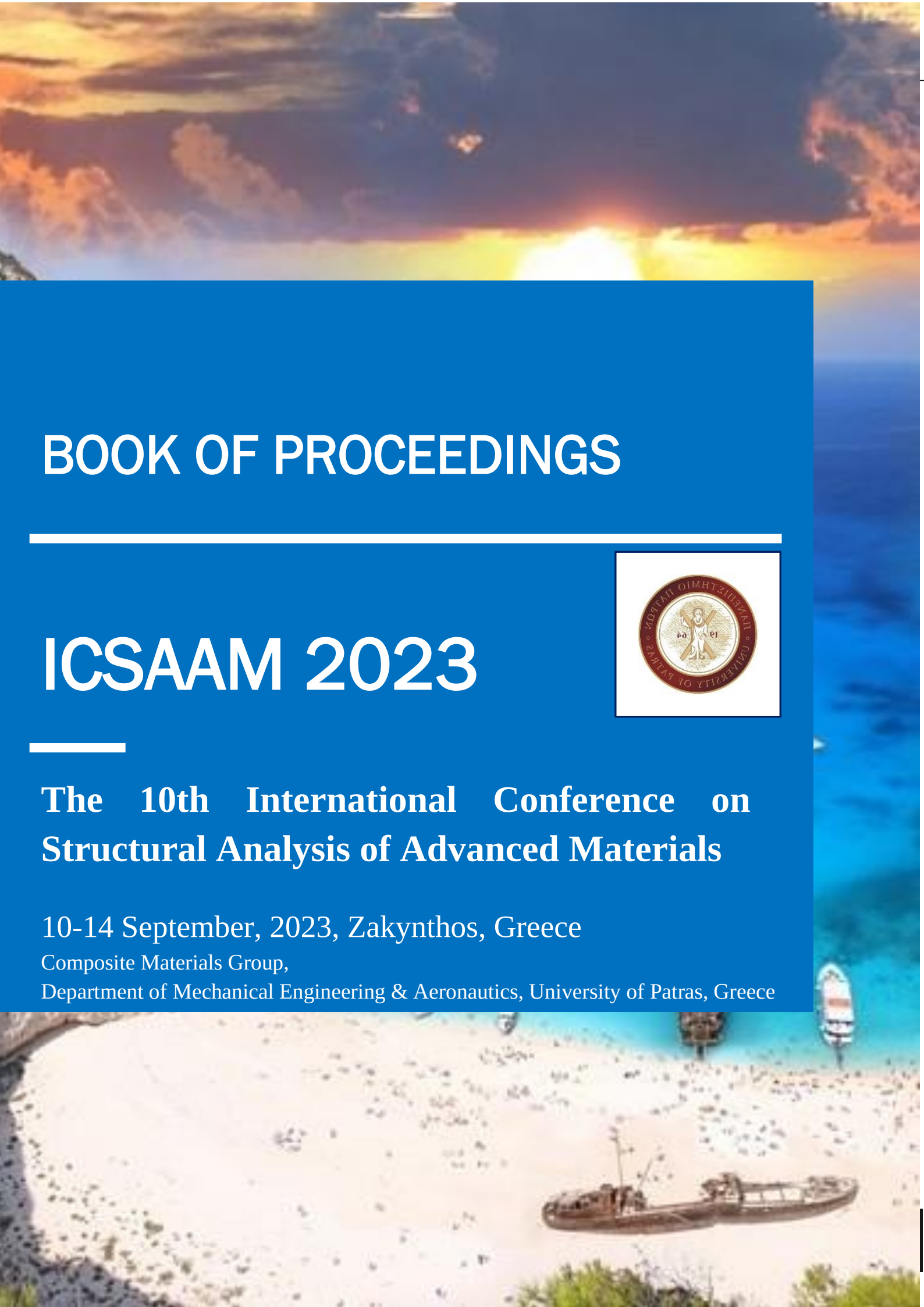

BOOK OF PROCEEDINGS

ICSAAM 2023

The 10th International Conference on Structural Analysis of Advanced Materials

10-14 September, 2023, Zakynthos, Greece

Composite Materials Group,
Department of Mechanical Engineering & Aeronautics, University of Patras, Greece

10th International Conference on Structural Analysis of Advanced Materials

Zakynthos, Greece

Committees

ICSAAM 2023

George C. Papanicolaou
Professor
Chairman of ICSAAM 2023

10-14 September 2023, Island of Zante, Zakynthos, Greece

ORGANIZED by the University of Patras, Greece
Dept. of Mech. Eng. & Aeronautics
COMPOSITE Materials Group

Dionysios E. Mouzakis
Professor
Co-chairman of ICSAAM 2023

In Collaboration with:

Gabriel Jiga
Professor
General Co-Chairman
of *ICSAAM 2023*
The University Politehnica of Bucharest
Romania

Olivier Dalverny
Professor
General Co-Chairman
of *ICSAAM 2023*
National School of Engineers of Tarbes
France

Pedro Moreira
Professor
General Co-Chairman
of *ICSAAM 2023*
Universityof Porto
Portugal

Alberto D'Amore
Professor
General Co-Chairman
of *ICSAAM 2023*
University of Campania "Luigi Vanvitelli"
Italy

Vasileios Drakonakis
Doctor
General Co-Chairman
of *ICSAAM 2023*
University of Nicosia
Cyprus

Local Organizing Committee

General Chairman – George Papanicolaou, Professor Emeritus, Department of Mechanical Engineering and Aeronautics, University of Patras, Greece.

Co-Chairman – Dionysios Mouzakis, Professor, Department of Military Sciences, Hellenic Army Academy, Vari, Greece

General Secretary – Diana Hortensia Portan, MSc, PhD, Department of Mechanical Engineering and Aeronautics, University of Patras, Greece.

Lykourgos Kontaxis, PhD, Department of Mechanical Engineering and Aeronautics, University of Patras, Greece.

Volunteers:

1. **Alexandra Angelopoulou**
2. **Sofia Mamali**
3. **Maria Thabet**
4. **Irene Flower**

International Scientific Committee

Co-Chair of the ISC

***Constantinos Soutis**, Professor, PhD(Cantab), CEng, FRAeS, FIMechE, FIM, AFAIAA, Chair of Aerospace Engineering, Director of Aerospace Research Institute, Research Director of NW Composites Centre/NCCEF, School of Mechanical, Aerospace & Civil Engineering, D41, Sackville Street Building, University of Manchester, Manchester M13 9PL (Sat Nav: M1 3NJ), **U.K.**, e-mail: constantinos.soutis@manchester.ac.uk, Website: www.mace.manchester.ac.uk*

***John Botsis,** Professor Emeritus, Institute of Mechanical Engineering, Laboratory of Applied Mechanics and Reliability Analysis EPFL STI / IGM / LMAF, Lausanne, **Switzerland**, e-mail: john.botsis@epfl.ch*

Members of the ISC
(in alphabetical order by country)

***Ralf Schledjewski**, Christian Dopppler Laboratory for High Efficient Composite Processing, Montanuniversität Leoben, Leoben, Austria; Processing of Composites Group, Department of Polymer Engineering, Leoben, **Austria**, e-mail: Ralf.Schledjewski@unileoben.ac.at*

***Danny Van Hemelrijck,** Department Mechanics of Materials and Constructions (MeMC), Vrije Universiteit Brussel (VUB), Pleinlaan 2, 1050 Brussels, **Belgium**, e-mail: Danny.Van.Hemelrijck@vub.ac.be*

***Vassilis Drakonakis**, Co-founder and Managing Director, Defense and Security Research Institute, University of Nicosia, AmaDema, Advanced Materials Design & Manufacturing Limited, Nicosia, **Cyprus**, e-mail: vassilis@amdmcomposites.com*

***Olivier Dalverny**, University of Toulouse, INP/ENIT, Tarbes, **France**, e-mail: olivier.dalverny@enit.fr*

***Pierre Ouagne,** Laboratoire Génie de Production, LGP, Université de Toulouse, INP-ENIT, Tarbes, **France**, e-mail: pierre.ouagne@enit.fr*

***Hajo Dieringa**, Helmholtz-Zentrum Hereon, Institute of Material and Process Design, Head of Department Hybrid Materials and Processes, Max-Planck-Str. 1, 21502 Geesthacht, **Germany**, e-mail: hajo.dieringa@hereon.de*

***Siegfried Schmauder**, University of Stuttgart, Department Head of Multi-Scale Simulation, Institute for Materials Testing, Materials Science and Strength of Materials (IMWF), **Germany**, e-mail: siegfried.schmauder@imwf.uni-stuttgart.de*

***Dimitris Alexandropoulos**, Department of Materials Science, University of Patras, **Greece**, e-mail: dalexa@upatras.gr*

***Nikolaos Athanasopoulos**, FORTH/ICEHT – Mechanical Engineering and Aeronautics, **Greece**, e-mail: aeronauticsnikos_athanasopoulos@protonmail.com*

***Nektaria Barkoula,** Department of Materials Engineering, University of Ioannina, **Greece**, e-mail: nbarkoul@uoi.gr*

International Scientific Committee

International Scientific Committee

Members of the International Scientific Committee are coming from the following 16 countries:

Austria	***Germany***	***Latvia***	***Portugal***
Belgium	***Greece***	***The Netherlands***	***Romania***
Cyprus	***Israel***	***Norway***	***Switzerland***
France	***Italy***	***Poland***	***U.K.***

Table Of Contents

ICSAAM 2023 SHORT PROGRAM

Sunday 10 Sep. 2023 20:00 pm Reception Party – Leschi of Zakynthos							
	Monday 11 Sep.23		Tuesday 12 Sep.23		Wednesday 13 Sep.23		Thursday 14 Sep.23
8.30-17.00	Conf. Desk Opening Hours		Conf. Desk Opening Hours		Conf. Desk Opening Hours		Conf. Desk Opening Hours
	SESSION 1A		SESSION 5A		SESSION 9A		SESSION 13C
8:30-9:00	OPENING CEREMONY		PL.5A.1		PL.9A.1		SUMMER SCHOOL SEMINAR 3 9:00-10:30
9:00-9:30	PL.1A.1		PL.5A.2		PL.9A.2		
9:30-10:00	PL.1A.2		PL.5A.3		PL.9A.3		
10:00-10:30	PL.1A.3		PL.5A.4		PL.9A.4		
10:30-11:00	Coffee Break		Coffee Break		Coffee Break		Coffee Break
	SESSION 2A		SESSION 6A		SESSION 10A		SESSION 14C
11:00-11:30	PL.2A.1		PL.6A.1		PL.10A.1		SUMMER SCHOOL SEMINAR 4 11:00-12:30
11:30-12:00	PL.2A.2		PL.6A.2		PL.10A.2		
12:00-12:30	PL.2A.3		PL.6A.3		PL.10A.3		
12:30-13:00	PL.2A.4		PL.6A.4		PL.10A.4		Closing Ceremony
13:00-14:00	Lunch Break		Lunch Break		Lunch Break		Lunch
	SESSION 3A	SESSION 3B	SESSION 7A	SESSION 7B	SESSION 11A	SESSION 11C	
14:00-14:20	KNL.3A.1	KNL.3B.1	KNL.7A.1	KNL.7B.1	KNL.11A.1	SUMMER SCHOOL SEMINAR 1 14:00-15:30	
14:20-14:40	KNL.3A.2	KNL.3B.2	KNL.7A.2	KNL.7B.2	KNL.11A.2		
14:40-14:55	3A. P1	3B. P1	7A. P1	7B. P1	11A. P1		
14:55-15:10	3A. P2	3B. P2	7A. P2	7B. P2	11A. P2		
15:10-15:25	3A. P3	3B. P3	7A. P3	7B. P3	11A. P3		
15:30-16:00	Coffee Break		Coffee Break		Coffee Break		
	SESSION 4A	SESSION 4B	SESSION 8A	SESSION 8B	SESSION 12A	SESSION 12C	
16:00-16:20	KNL.4A.1	KNL.4B.1	KNL.8A.1	KNL.8B.1	KNL.12A.1	SUMMER SCHOOL SEMINAR 2 16:00-17:30	
16:20-16:40	KNL.4A.2	KNL.3B.2	KNL.8A.2	KNL.8B.2	KNL.12A.2		
16:40-16:55	4A. P1	4B. P1	8A. P1	8B. P1	12A. P1		
16:55-17:10	4A. P2	4B. P2	8A. P2	8B. P2	12A. P2		
17:10-17:25	4A. P3	4B. P3	8A. P3	8B. P3	12A. P3		
17:25-17:40	4A. P4	4B. P4	8A. P4	8B. P4	12A.P4		
17:30	END OF ORAL SESSIONS		END OF ORAL SESSIONS		END OF ORAL SESSIONS		
17:30-18:30	RAPIDFIRE POSTER SESSION HALL A						
21:00	CHAIR & ICSAAM DINNER* TAVERNA KERI		GALA DINNER** LATAS HOUSE		GREEK TAVERNA NIGHT*** POPOLAROS TAVERN		

NOMENCLATURE		
A: HALL A: Leschi of Zakynthos	**PL:** Plenary Lecture	*PAID BY the CONFERENCE 25-30 Ps max
B: HALL B: Public Historical Library of Zakynthos	**KNL:** Keynote Lecture	**PAID BY the CONFERENCE 250 Ps
C: HALL C: Solomou - Kalvou Museum Library	**P:** Oral Presentation	***PAID BY the DELEGATES ca. 150-200 Ps

Monday 11 Sep. 2023	**SESSION 3A** Oral Presentations **Damage and Failure**
Session 3A Co-Chairmen:	**Alkis Paipetis,** Professor of Experimental Mechanical Behavior and Non-Destructive Testing of Composite Materials, Department of Materials Science & Engineering, University of Ioannina, Greece. **Michalis Georgallas,** Quality Assurance Manager at AmaDema (Advanced Materials Design & Manufacturing Limited), Cyprus.

ENERGY ABSORPTION BEHAVIOR IN BIO-COMPOSITES UNDER IMPACT LOADING: A CASE STUDY

B. Ravindran[1], J.C. Cardenas Velasco[1], M. Feuchter[2], T. Agathocleous[3], B. Oswald-Tranta[3] and R. Schledjewski[1]

[1] Montanuniversität Leoben, Department of Polymer Engineering and Science, Processing of Composites Group, Leoben, Austria, www.kunststofftechnik.at; Corresponding Author: bharath.ravindran@unileoben.ac.at

[2] Montanuniversität Leoben, Department of Polymer Engineering and Science, Chair of Materials Science and Testing of Polymers, Leoben, Austria, www.kunststofftechnik.at

[3] Montanuniversität Leoben, Department of Product Engineering, Chair of Automation, Leoben, Austria, https://coa.unileoben.ac.at/

ABSTRACT

Bio-composite with natural fiber reinforcements, such as flax fibers have found widespread use in engineering materials. However, there is scarce data in the literature regarding the impact behavior of flax fiber composites taking the sustainable matrix into account. In this context, the impact behavior of flax fiber composite is investigated by considering the influence of sustainable matrix systems. The two different types of bio-based thermoset matrices are, (a) partly bio-based matrix Epinal b.poxy IR78.31/ amine hardener IH77.11 and (b) vitrimer matrix based on epoxidized linseed oil/glutaric acid/triazabicyclodecene. This study focuses on an assessment of the low-velocity falling weight impact under three different energy levels (10, 15 and 20 J). The experimental findings reveal that flax-vitrimer resin composite exhibits slightly higher energy absorption than flax-partially bio-based resin composites.

INTRODUCTION

Bio-composite structures may face impact loads from dropped tools, collisions with fixtures, ballast, or cargo during their service life. These impacts can cause internal damage that significantly reduces the residual mechanical properties of the biocomposite. While the number of studies investigating the mechanical behavior of flax fiber composites has been increasing, most research has focused on the impact response of conventional fossil-based thermoplastic and thermoset matrices [1-4]. As a result, the investigation of the impact behavior of flax fiber composites with bio-based matrices is still limited. To address this gap, the present study aims to contribute to the understanding of the impact behavior of flax fiber composites with sustainable matrices. Specifically, two different sustainable matrices are utilized: a partially bio-based epoxy matrix (Epinal IR78.31/IH77.11) and a vitrimer-based matrix (ELSO/Anhydride/TBD). Composite plates are manufactured using the vacuum-assisted resin infusion (VARI) process. Low-velocity impact tests are conducted at various energy levels using a drop tower apparatus. The experimental investigation involves analyzing the peak force, displacement, absorbed energy results for the flax-partly bio-based epoxy and flax-

vitrimer-based epoxy composites, respectively. These analyses provide valuable insights into the energy absorption capacity between the two sustainable matrices.

MATERIALS AND EXPERIMENTAL METHODS

Flax fiber, known as Amplitex 5042 supplied by Bcomp Ltd, Fribourg, Switzerland is used as the reinforcement which is a woven fabric in a balanced 4x4 twill weave architecture with areal density of 500 g/m^2. For the partly bio-based matrix system, Epinal b.poxy IR78.31 (37.58% of bio-based resin content) and Epinal IH77.11 amine hardener supplied by bto-epoxy GmbH (Amstetten, Austria). While the vitrimer based matrix system consist of three parts, the resin (Epinal NFL 10.20 -A4.00 epoxidized linseed oil ELSO) and the catalyst (TBD, 1,5,7-Triazabicyclo [4.4.0] dec-5-ene) are supplied by bto-epoxy GmbH (Amstetten, Austria) and the hardener (Glutaric anhydride) from Sigma-Aldrich Handels GmbH (Vienna, Austria). The composite laminates were processed by VARI method that uses a single sided rigid mold and vacuum bagging where vacuum pressure is applied as depicted in Figure 1. The composite laminates were fabricated with nominal thickness of 5 mm. The specimens measuring 100 x 150 mm were prepared for testing. The impact test tests as shown in Figure 2 were conducted based on standard test method for drop tower impact testing of composite ASTM D7136 using a CEAST 9350 instrumented drop tower (Instron, USA). Impact energy was varied by adding weights, resulting in energy levels of 10 J, 15 J and 20 J.

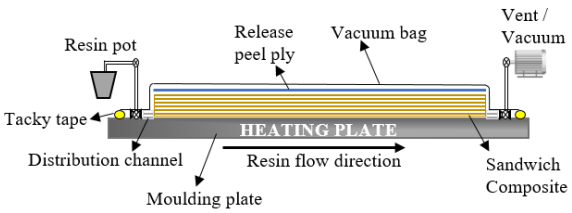

FIGURE 1 Schematic diagram of VARI technique

FIGURE 2 Impact testing method

RESULTS AND DISCUSSION

Table 1 presents the peak force, absorbed energy, and displacement corresponding to different impact energy levels for the two composite materials. The relationship between impact energy and impact parameters is illustrated in the Figure 3. For both the flax-partially bio-based matrix and flax-vitrimer matrix composites, the peak force initially increases with increasing impact energy until 15 J, after which there is a drop in peak force at 20 J. However, the flax-partially bio-based matrix composite exhibits approximately 25 % higher peak forces compared to the flax-vitrimer matrix composite (Fig 3a). On the other hand, the flax-vitrimer matrix composite demonstrates higher absorbed energy than the flax-partially bio-based matrix composite. Specifically, at 10 J and 15 J, the absorbed energy for the vitrimer matrix composite is 50 % higher than that of the partly bio-based matrix composite.

At 20 J, the absorbed energy for the vitrimer matrix composite is slightly higher, approximately 6 %, compared to the partly bio-based matrix composite (Fig 3b). Furthermore, the displacement of specimens from the flax-vitrimer matrix composite is greater than that of the flax-partially bio-based matrix composite across the range of impact energies. The displacement shows a linear trend (Fig 3c), indicating an increase in permanent indentation with higher impact energy.

TABLE 1 Impact mechanical properties

Impact energy, J	Flax-partly bio-based matrix			Flax-vitrimer matrix		
	Peak Force, N	Absorbed Energy, J	Displacement, mm	Peak Force, N	Absorbed Energy, J	Displacement, mm
10	3197.6	4.41	4.54	2575.0	7.48	6.36
15	3523.1	6.41	6.18	2715.9	11.07	9.45
20	3369.3	10.57	8.23	2498.1	11.27	11.48

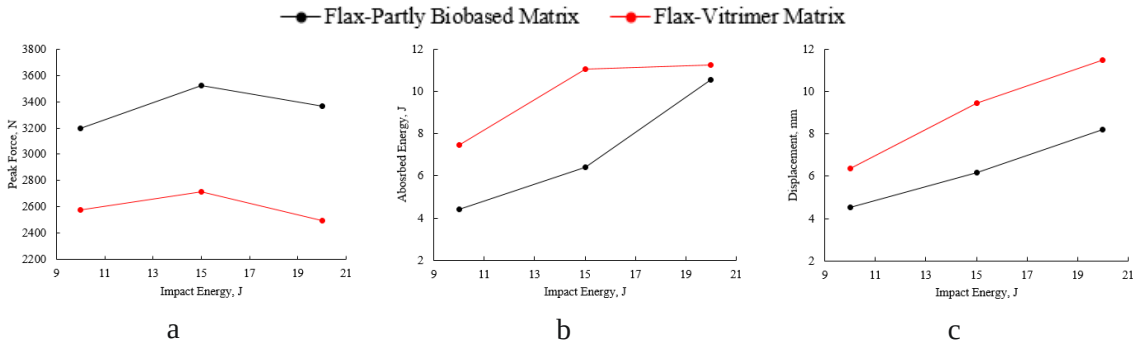

a b c

FIGURE 3 The relationship between impact energy and impact characteristic

CONCLUSIONS

In this study, the energy absorption capacity of flax-partly bio-based matrix composites and flax-vitrimer matrix composite laminates was investigated through low-velocity impact tests. The flax-partially bio-based matrix composite exhibited approximately 25 % higher peak forces compared to the flax-vitrimer matrix composite. The flax-vitrimer matrix composite demonstrated higher absorbed energy compared to the flax-partially bio-based matrix composite. Specifically, at impact energy levels of 10 J and 15 J, the vitrimer matrix composite absorbed nearly 50 % energy than the partly bio-based matrix composite. At an impact energy of 20 J, the vitrimer matrix composite absorbed approximately 6 % more energy. Based on these experimental findings, it can be concluded that the peak force, displacement, and associated energy absorption are primarily influenced by the matrix material and the impact energy level.

ACKNOWLEDGEMENTS

The financial support through project QB3R (project no. FO999889818) provided by the Austrian Ministry for Climate Action, Environment, Energy, Mobility, Innovation and Technology within the frame of the FTI initiative “Kreislaufwirtschaft 2021”, which is administered by the Austria Research Promotion Agency (FFG) is kindly acknowledged.

REFERENCES

1. Yan, L.; Chouw, N.; Jayaraman, K. Flax fibre and its composites – A review, *Composites Part B: Engineering* 2014, 56, 296-317, ISSN 1359-8368, https://doi.org/10.1016/j.compositesb.2013.08.014.

2. Rodriguez, E.; Petruci, R.; Puglia, D.; Kenny, J.M.; Zquez, A.V. Characterization of composites based on natural and glass fibers obtained by vacuum infusion. *J. Compos. Mater.* 2005, 39, 265–283. doi: 10.1177/0021998305046450.

3. Ravandi, M.; Teo, W.S.; Tran, L.Q.N.; Yong, M.S.; Tay T.E. Low velocity impact performance of stitched flax/epoxy composite laminates, *Composites Part B: Engineering* 2017, 117, 89-100, ISSN 1359-8368, https://doi.org/10.1016/j.compositesb.2017.02.003.

4. Dhakal, H; Ghasemnejad, H; Zhang, Z.; Ismail, S; Arumugam, V. The post-impact response of flax/UP composite laminates under low velocity impact loading. *International Journal of Damage Mechanics*. 2019, 28(2), 183-199. doi:10.1177/1056789517751239.

ON THE DECOUPLING OF FRACTURE MODES IN INTERLAMINAR FRACTURE TESTS ON BIMATERIAL SPECIMENS

P. Tsokanas[1], L.F.M. da Silva[2], F. Mujika[3], A. Arrese[3], P. Fisicaro[4], P.S. Valvo[4]

[1] *INEGI, 4200-465 Porto, Portugal; Corresponding Author: panayiotis.tsokanas@gmail.com*

[2] *Faculdade de Engenharia, Universidade do Porto, 4200-465 Porto, Portugal*

[3] *Faculty of Engineering of Gipuzkoa, University of the Basque Country, 20018 San Sebastián, Spain*

[4] *Department of Civil and Industrial Engineering, University of Pisa, IT-56122 Pisa, Italy*

ABSTRACT

We start by reviewing methods for fracture mode decoupling in unconventional laboratory specimens. Then, we propose energetically orthogonal mode decoupling conditions and associated specimen design criteria to obtain pure fracture modes when bimaterial specimens are tested in asymmetric double cantilever beam and asymmetric end-notched flexure test configurations. This work hopefully sheds light on some controversial points in the relevant literature.

INTRODUCTION

We consider laboratory tests for measuring the interlaminar fracture toughness of a delamination specimen. Such tests can generally be modelled by considering the specimen as a plane (two-dimensional) cracked body, while the crack propagates in a mix of the basic fracture modes I (opening) and II (sliding). If this body is symmetrically cracked (Fig. 1a), fracture modes I and II are respectively associated to systems of symmetric and antisymmetric forces with respect to the crack plane. These forces respectively produce only normal stresses, σ_n (or crack-tip normal forces, F_n), and transverse relative displacements, δ_n, or only shear stresses, σ_t (or crack-tip shear forces, F_t), and axial relative displacements, δ_t, on the crack plane around the crack tip (Fig. 1b). These simple pure-mode conditions do not apply in general for asymmetrically cracked bodies (Fig. 1c), such as bimaterial specimens.

In this presentation, we will revisit the problem of fracture mode decoupling and again propose pure-mode conditions and derive associated specimen design criteria, aiming to resolve the controversial points in the literature. We focus on the asymmetric double cantilever beam (ADCB) (Fig. 1d) and asymmetric end-notched flexure (AENF) (Fig. 1e) test configurations, also assuming that both sub-beams are homogeneous and special orthotropic. This work assumes that pure mode I conditions occur when $\delta_t = 0$. Then, by enforcing energetical orthogonality with mode II, it follows that pure mode II conditions occur when $F_n = 0$. Using these pure-mode conditions, and by developing a simple mechanical model using laminated beam theory, Engesser–Castigliano's theorem, and unit-load method —this work was very recently published in Ref. [1]—, we derive the specimen design

criteria for bimaterial specimens loaded using the ADCB and AENF test configurations from scratch. We will show that the two criteria to obtain pure mode I in the ADCB test and pure mode II in the AENF test coincide and are aligned with the criterion used in part of the existing literature. We hope that the present work helps resolve the confusion in the literature regarding the correctness of different mode decoupling conditions.

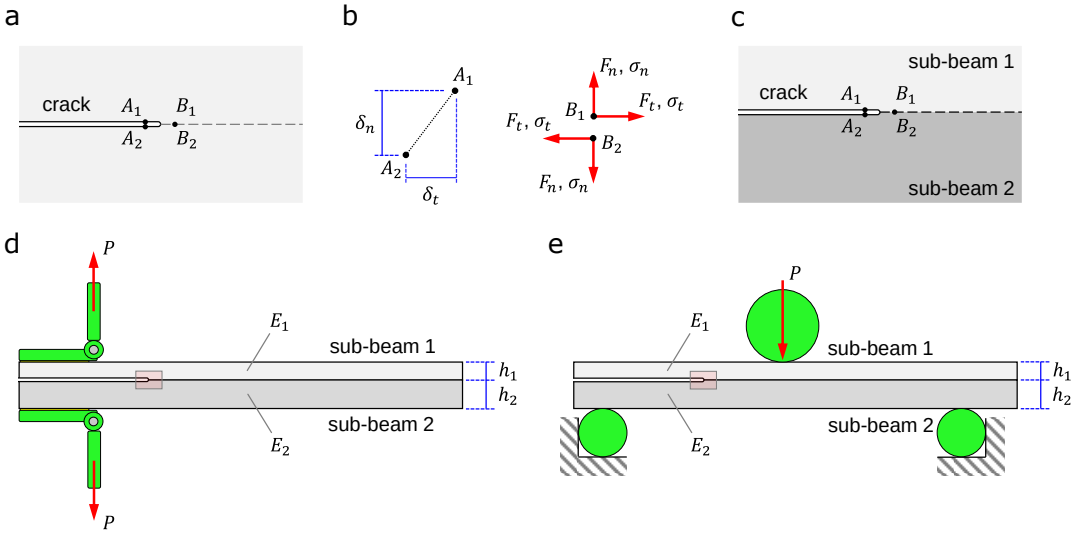

FIGURE 1 (a) Symmetric crack problem; (b) relative displacements, forces, and stresses near the crack tip; (c) asymmetric crack problem; and (d) ADCB and (e) AENF test configurations.

EXISTING PURE-MODE CONDITIONS AND SPECIMEN DESIGN CRITERIA

Energetically orthogonal pure-mode conditions

Valvo [2] demonstrated that the 'standard' virtual crack closure technique (VCCT)—based on the decomposition of the crack-tip nodal forces into symmetric and antisymmetric components—may be inappropriate when analysing problems with highly asymmetric cracks since negative values may be calculated for either mode I, G_I, or mode II, G_{II}, contributions to the energy release rate (ERR), G. To remedy this shortcoming, the author suggested defining pure modes based on energetically orthogonal systems of forces at the crack tip. In this way, always non-negative modal contributions to the ERR are obtained. At first, he proposed to identify pure mode I as the case when $F_t = 0$, and pure mode II as the case when $\delta_n = 0$. In a subsequent work [3], the same author reconsidered his proposal and suggested the following conditions instead: pure mode I occurs when $\delta_t = 0$, and pure mode II occurs when $F_n = 0$. The more recent proposal has a more convincing physical basis, as it assumes that mode I fracture corresponds to a pure opening of the crack faces.

Similarly to Valvo, Harvey and Wang [4, 5] developed an orthogonal pure mode methodology for partitioning the ERR into its modal contributions. They assumed that the mode I loading condition must be orthogonal to the mode II loading condition through the ERR 'space'. Using this, any pure-mode condition can be identified experimentally, theoretically, or numerically, and the orthogonality condition can then be used to find the other pure modes. The authors defined two sets of pure-mode conditions:

- Set 1: Pure mode I exists when $\delta_t = 0$, and pure mode II exists when $F_n = 0$
- Set 2: Pure mode I exists when $F_t = 0$, and pure mode II exists when $\delta_n = 0$

Interestingly, their first and second sets of pure modes respectively correspond to the two pure-mode sets proposed by Valvo in Refs. [3] and [2]. Harvey and Wang derived the pure modes in the contexts of Euler and Timoshenko beam theories for *rigid* interfaces and the ADCB configuration. Euler beam theory can predict negative G_I/G or G_{II}/G components over a certain number of loading conditions. Although Valvo [2] and other authors [6] state that this lacks physical interpretation, Harvey and Wang argue that there is no physical requirement on the modal contributions to the ERR, G_I and G_{II}, and the only physical requirement is that G must be non-negative definite since creating new crack surfaces requires energy.

Specimen design criteria

We now focus on the ADCB test configuration, considering both material and geometric asymmetry (Fig. 1d), as the specimen consists of two sub-beams of different longitudinal Young's moduli, E_i, and thicknesses, h_i, $i \in \{1, 2\}$. A reasonable question is whether we can appropriately design the specimen (e.g. define Young's moduli and thicknesses of both sub-beams) to achieve pure-mode I conditions (at the crack tip). Two mode decoupling conditions can be recognised in the literature:

- Mode decoupling is achieved when the differential equation of the mode I fracture is only governed by σ_n and δ_n (e.g. [7])
- Mode decoupling is achieved when the bending rigidities of the two sub-beams are equal (e.g. [8])

These conditions respectively lead to the following specimen design criteria:

$$E_1 h_1^2 = E_2 h_2^2 \quad \text{and} \quad E_1 h_1^3 = E_2 h_2^3, \tag{1}$$

which although both are used in the literature (e.g. [7, 8]), cannot both be correct. Thus, our work [1] aims to elucidate which one is ultimately correct.

THE PROPOSED SPECIMEN DESIGN CRITERIA

In this presentation, we will revisit the problem of fracture mode decoupling and discuss the various proposed definitions for pure-mode conditions, aiming to clarify which theoretical definitions for pure modes are to be preferred. We will focus on the ADCB and AENF test configurations, assuming that both sub-beams are homogeneous and special orthotropic. The work assumes that under pure mode I conditions, $\delta_t = 0$, while under pure mode II conditions, $F_n = 0$ [3–5]. Using this set of conditions and by developing a mechanical model employing laminated beam theory, Engesser–Castigliano's theorem, and unit-load method [1], we will derive the mode decoupling conditions for bimaterial specimens loaded using the ADCB and AENF test configurations from scratch. We will show that the two conditions to obtain pure mode I in the ADCB test and pure mode II in the AENF test coincide and are the same with the first equation of Eqs. (1) that is being used in part of the literature (e.g. [7]). In addition, we will demonstrate that the analysis of the AENF test may get complicated by the contact phenomena occurring between the two sub-beams. This contact may alter the general rules for fracture mode partitioning [9].

We hope that the present work sheds light on the confusion in the literature regarding the correctness of different mode decoupling conditions and associated specimen design formulae. For more details and insights, we refer the reader to our journal publications [1]. The present work can be extended by deriving specimen design criteria for multidirectional laminated specimens [9].

ACKNOWLEDGEMENTS

PT and LFMdS acknowledge the financial support of FCT through the PTDC/EME-EME/6442/2020 project. FM and AA acknowledge the financial support of UPV/EHU to the GIU20/060 research group.

REFERENCES

1. Mujika, F.; Tsokanas, P.; Arrese, A.; Valvo, P. S.; da Silva, L. F. M. Mode decoupling in interlaminar fracture toughness tests on bimaterial specimens, *Eng. Fract. Mech.* 2023, 290, 109454.

2. Valvo, P.S. A revised virtual crack closure technique for physically consistent fracture mode partitioning, *Int. J. Fract*. 2012, 173, 1-20.

3. Valvo, P.S. A further step towards a physically consistent virtual crack closure technique, *Int. J. Fract*. 2015, 192, 235-244.

4. Wang, S.; Harvey, C.M. Mixed mode partition theories for one dimensional fracture, *Eng. Fract. Mech.* 2012, 79, 329-352.

5. Harvey, C.M.; Wang, S. Mixed-mode partition theories for one-dimensional delamination in laminated composite beams, *Eng. Fract. Mech*. 2012, 96, 737-759.

6. Maimí, P.; Gascons, N.; Ripoll, L.; Llobet, J. Mixed mode delamination of asymmetric beam-like geometries with cohesive stresses, *Int. J. Solids Struct*. 2018, 155, 36-46.

7. Ouyang, Z.; Ji, G.; Li, G. J. On Approximately Realizing and Characterizing Pure Mode-I Interface Fracture Between Bonded Dissimilar Materials, *Appl. Mech.* 2011, 78 (3), 031020.

8. Jiang, Z.; Wan, S.; Wu, Z. Calculation of energy release rate for adhesive composite/metal joints under mode-I loading considering effect of the non-uniformity, *Compos. B Eng*. 2016, 95, 374-385.

9. Garulli, T.; Catapano, A.; Fanteria, D.; Jumel, J.; Martin, E. J. Design and finite element assessment of fully uncoupled multi-directional layups for delamination tests, *Compos. Mater.* 2020, 54 (6), 773-790.

DETECTABILITY OF NOTCHES IN PLATES USING MULTI-MODAL LAMB WAVES

A.D. Griguța[1], M.V. Predoi [2*], C.C. Petre[3]

[1]M.Sc. stud., Department of Mechanics, University Politehnica of Bucharest, Splaiul Independenței, 313, 060042, Bucharest, ROMANIA

[2]Prof., Department of Mechanics, University Politehnica of Bucharest, Splaiul Independenței, 313, 060042, Bucharest, ROMANIA – (*) corresponding author (mihai.predoi@upb.ro)

[3]Prof., Department of Strength of Materials, University Politehnica of Bucharest, Splaiul Independenței, 313, 060042, Bucharest, ROMANIA

ABSTRACT

Notches in plates can be detected using classical nondestructive testing, with ultrasonic waves sent perpendicular to the surface. However, considering the long-range propagation of the Lamb waves, inspection can be made by sending the ultrasonic waves along the plate. There are many prior researches which state the above idea. In this paper, the interest is to correlate the central frequency of the transducer in use, with the capacity to detect different sizes of notches. The choice of adequate parameters has been done by developing finite elements simulations in COMSOL [1], on a specific plate. The results show that the manufactured notch is detected at every frequency in the proposed range (1 - 2MHz).

Nonetheless, it is important to determine graphics in which are shown the propagative modes with high accuracy.

INTRODUCTION

Ultrasonic testing is a principal technique in non-destructive testing, being applied in the majority of industrial branches. The use of this technique is an important step ahead in aerospace structure testing for fatigue cracks/notches detection. This technique is used in a wide range of part testing in different other domains.

Prior studies have shown that the classic technique in which the wave is applied perpendicular to the surface of the structure provides good results. However, the application of this specific technique for a wide structure is time consuming. The guided waves technique has been developed by using ultrasonic waves applied directly along the thin layer of the planar structure. Nonetheless by applying the waves in this manner, the inspection covers a long distance, but the theoretical aspects and the raw data analysis are more complex for these guided Lamb waves. Papers and books regarding the guided wave theory [2], [3], numerical simulations [4], [5] and experiments have been proposed mostly for the propagation of Lamb waves [6] and some had studied the edge reflection [7] and detection of defects too, e.g. [8].

This paper is focused on the correlation between the dimension of the surface defects and their possible detection, using different central frequencies of the longitudinal waves transducer, which sends several Lamb modes simultaneously. The results are obtained using COMSOL Multiphysics Finite Element Method (FEM) simulations. The obtained results provide a graphic visualization as the Position-Time plots of the FEM results, which are then post-processed in MATLAB [9].

The proposed simulation is according to the geometry and material of a specific plate. Different applications were proposed for each of the considered frequencies in order to have both, the correlation between the maximal size of the finite element and the frequency and the favorable graphic time dependent transducer pulse impulse (mathematical expression regarding the Gaussian envelope).

In order to present these results, it is important to understand the concept of ultrasonic Lamb waves. Therefore, theoretical knowledge is mandatory to be understood with the multimode propagation concept presented in more details in [6]. In the case of Lamb waves two different modes of propagation appear, symmetrical and asymmetrical. The expression of displacements for each case are as follows:

Symmetrical:

$$\begin{aligned} u &= [iS_L k_x \cos(k_{Lz} z) - S_T k_{Tz} \cos(k_{Tz} z)] e^{i(k_x x - \omega t)} \\ w &= [-S_L k_{Lz} \sin(k_{Lz} z) + iS_T k_x \sin(k_{Tz} z)] e^{i(k_x x - \omega t)} \end{aligned} \quad (1)$$

Asymmetrical:

$$\begin{aligned} u &= [iA_L k_x \cos(k_{Lz} z) + A_T k_{Tz} \cos(k_{Tz} z)] e^{i(k_x x - \omega t)} \\ w &= [A_L k_{Lz} \sin(k_{Lz} z) + iA_T k_x \sin(k_{Tz} z)] e^{i(k_x x - \omega t)} \end{aligned} \quad (2)$$

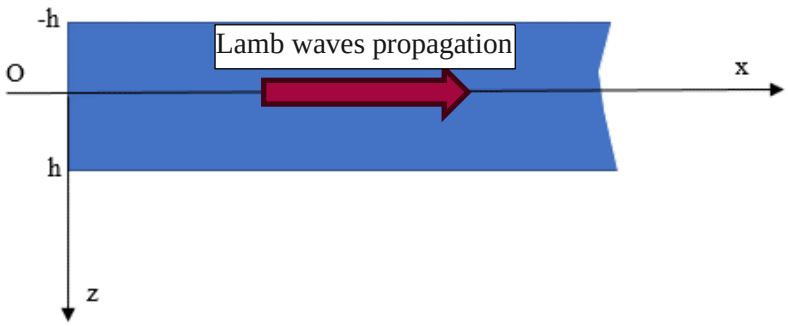

FIGURE 1 Semi-infinite plate of 2h thickness

The displacements are written based on the scalar and vectorial potential and in their expression several variables and constants may be found, f - frequency, c – velocity of the Lamb wave, c_T and c_L – transversal and longitudinal wave velocities, k_i – wavenumbers, S_T, S_L, A_T and A_L – values of the complex amplitudes.

As for the angular frequency and wavenumbers, the following formulas are considered:

$$\begin{aligned} &\omega = 2\pi f; \\ &k_x = \frac{\omega}{c}; k_T = \frac{\omega}{c_T}; k_L = \frac{\omega}{c_L}; \\ &k_{Tz} = \sqrt{{k_T}^2 - {k_x}^2}; k_{Lz} = \sqrt{{k_L}^2 - {k_x}^2} \end{aligned} \tag{3}$$

Following the expression of displacements (1), (2) for each case and considering elasticity theory [2], the expressions of dispersion curves may be found as:

Symmetrical:

$$C_s(k_x, \omega) = 4k_x^2 k_{Lz} k_{Tz} \tan(k_{Lz} h) + (2k_x^2 - k_T^2)^2 \tan(k_{Tz} h) = 0; \tag{4}$$

Asymmetrical:

$$C_a(k_x, \omega) = 4k_x^2 k_{Lz} k_{Tz} \tan(k_{Tz} h) + (2k_x^2 - k_T^2)^2 \tan(k_{Lz} h) = 0; \tag{5}$$

where *h* is the semi-thickness of the plate (FIGURE 1) and the other terms had been explained above.

SIMULATIONS IN COMSOL

First results provided by the FEM simulations represent the longitudinal and transversal displacements which are determined in a large range of points, selected both in the middle of the plate and on its surface. These FEM results have been processed in MATLAB as Position-Time plots. The most important results which are obtained in this research are the Position-Time plots of the FEM results for the transversal displacements at the surface (Figure 2). Such plots [6] indicate the group velocities and modal scattering by the 0.55 mm deep notch in a 3mm thick aluminum plate.

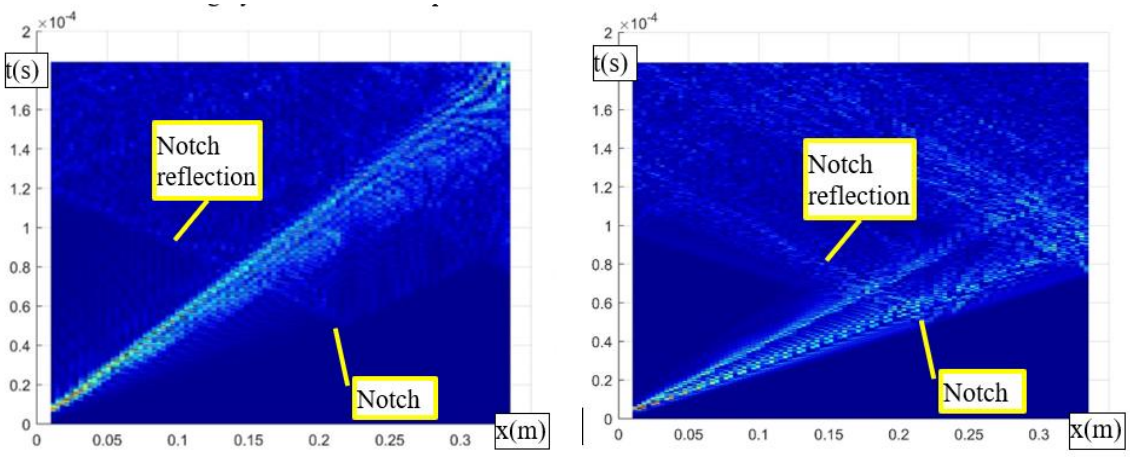

FIGURE 2 Position-Time plots of the FEM solution for the transversal displacements located on the surface of a plate with a defect for 1 MHz (left) and 2 MHz (right)

On both plots can be seen the detection of the notch, by the multimodal signal. Important is the first returning echo generated by the notch, proving that this method is adequate.

EXPERIMENTAL PART

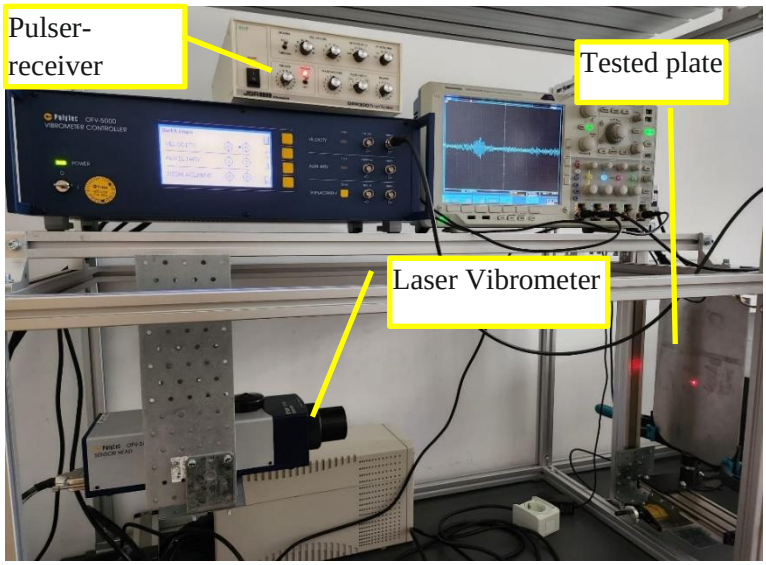

FIGURE 3 Experimental setup

The experimental setup is intended to compare the results extracted from the measurements with the ones from the simulation. Main components in use are a transducer with 1MHz central frequency, pulser-receiver, an oscilloscope, and laser-vibrometer.

Displacements on the surface of the plate were determined using a mobile platform controlled by a stepper motor. The displacements have been measured with the laser vibrometer for positions in the range of 145 mm with the distance between the steps of 0.11mm. There have been considered points of measurements, both before and after the defect positioning as to be comparable to the results from the simulation. All the configurations for pulser-receiver, oscilloscope and vibrometer laser were imposed to optimize the measurements displayed on the oscilloscope.

RESULTS AND DISCUSSION

Both simulated results in COMSOL and experimental results have been processed through the same MATLAB code for each set of data, providing the graphical representation of Position-Time plots. Results are presented in FIGURE 4.

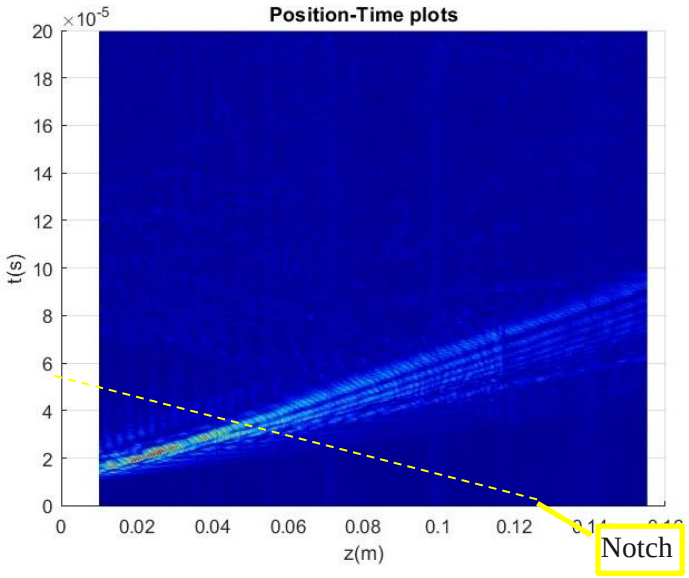

FIGURE 4 Position-Time plots for 1MHz from experimental measurements

The multimodal wave propagation is clearly visible as a set of lines originating at the transducer's position, at the left side of the plot. Having different group velocities, it is normal to see a spread of Lamb modes as the time and position increase. On FIGURE 4 was marked for better visibility, the thin dotted line, corresponding to the dominant reflected Lamb mode.

Although the position range in the experimental part is different, it can be stated that the graphics present similar slopes for the most prominent mode of propagation, indicating the same group velocities. The defect location is less visible, but the experiment confirms the simulation.

In FIGURE 5 the range of data for the experimental part have been changed to have the same resolution for both graphical representations (experimental and FEM simulation). In order to present the extreme values of errors between the results obtain from experiment and FEM simulation, there have been elaborated a MATLAB code through which the slope of the graph may be read from an image. The results obtained for these errors are not including the possible read errors of pixel positions, since these positions are selected by the mouse pointer on the computer monitor. This is a highly efficient method being rapid to apply and robust in terms of accuracy especially of the plots have a certain scatter and wobble. In these specific computations, the error for the maximum group velocity is near 0.2% and for the minimum group velocity is near 3.1%.

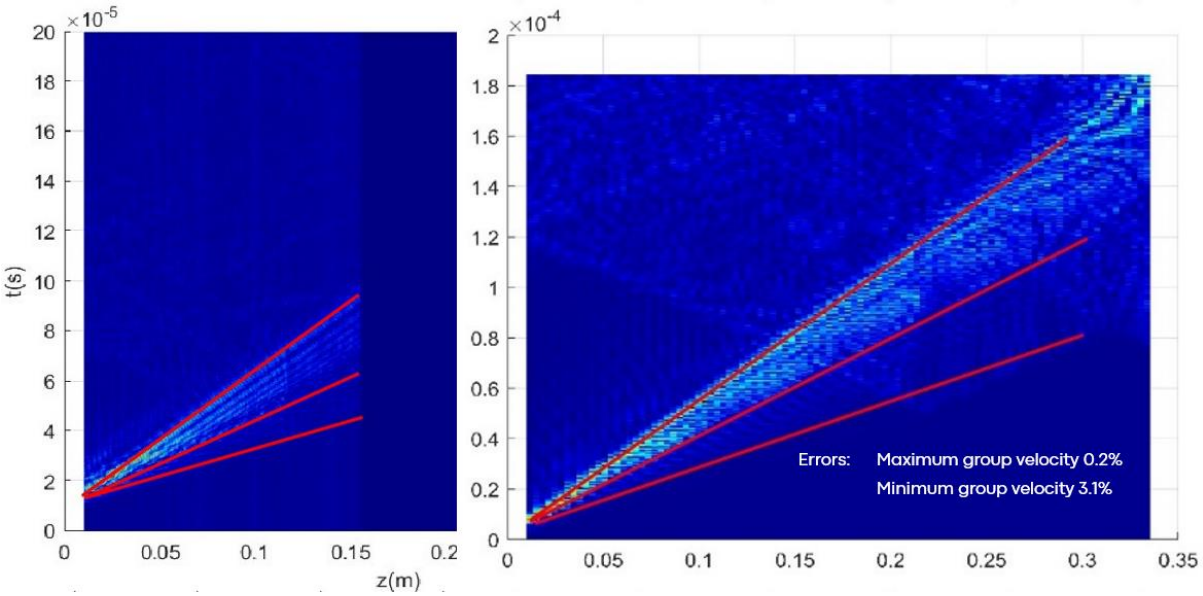

FIGURE 5 Position-Time plots 1 MHz Experiment Results (left) and FEM simulation results (right). Modal scattering is marked by the red lines.

CONCLUSIONS

The use of multimodal Lamb guided waves has been proven to be a useful approach in notch detection. The FEM simulation has provided useful results in predicting the sensitive modes for this purpose. The experimental part is at a preliminary stage. However, the results are encouraging in detecting the presence of a thin notch at a relatively large distance.

It can be emphasized that the detection was done at relatively low frequencies (1 and 2 MHz) which is an important advantage in industrial applications.

As research perspectives are mentioned the determination of the depth of the notch by changing the central frequency of the transducer producing the guided waves. Comparing the amplitudes of the reflected modes for at least two frequencies and based on corresponding FEM simulations, it is expected that the depth of the notch could be deduced.

Moreover, it is known that such asymmetric notch produces a strong dispersion among all the propagating modes, especially at higher frequencies. This dispersion depends on the notch depth and provides another research direction, keeping a single transducer of a fixed central frequency.

REFERENCES

1. *** COMSOL Multiphysics User Manual, “COMSOL - Software for Multiphysics Simulation,” COMSOL AB, 2023. [Online]. Available: http://www.comsol.com/.
2. Achenbach, J.D. Wave propagation in elastic solids, Amsterdam: North Holland, 1973.
3. Graff, K.F., Wave Motion in Elastic Solids, New York: Dover Publ., 1975.
4. Predoi, M.V.; Petre, C.C. Controle par ultrasons des plaques soudees, Bucharest: Ed. Printech, 2003, p. 150.
5. Predoi, M.V.; Griguța, A.D.; Petre, C.C. Similarities between guided and longitudinal ultrasonic waves, *U.P.B. Scientific Bulletin, Series A* 2022, 84(4).

6. Griguța, A.D.; Predoi, M.V. Generation of multi-modal Lamb waves for the inspection of thin aeronautical structures, *U.P.B. Scientific Bulletin, Series A* 2021, 83(4).
7. Predoi, M.; Rousseau, M. Recent results about lamb waves reflection at the free edge of an elastic layer, *Acta Acustica (Stuttgart)* 2003, 89(4).
8. Grondel, S.; Delebarre, C.; Assaad, J.; Dupuis, J.P.; Reithler L. Fathigue crack monitoring of riveted aluminium strap joints by Lamb wave analysis and acoustic emission measurement technique, *NDT&E International* 2003, 137-146.
9. MATLAB, 1994-2017 The MathWorks, Inc.," 2017. [Online]. Available: https://www.mathworks.com/products/matlab.html. [Accessed 20 11 2017].

Monday 11 Sep. 2023	**SESSION 3B** Oral Presentations **Exoprostheses and Exoskeletron Applications – The Nerve Repack Project**
Session 3B Co-Chairmen:	**Carmen Moldovan,** National Institute for Research and Development in Microtechnology – IMT, Bucharest, Romania **Andrei Costin Bratan,** Research Institute for Artificial Intelligence "Mihai Drăgănescu", Bucharest, Romania

METHODOLOGY AND BIOMATERIALS FOR THE UPPER LIMB STUMP WIRELESS CONNECTION TO A NEURAL EXOPROSTHESIS

V. Carbunaru[1], W. Bahaa-Eddin*[1], S. Lazarescu[1,2], A. Barbilian[1,2], E. Franti[3,4], M. Dascalu[4,5], A.M. Oproiu[5], Mark Pogarasteanu[1,2], M. Daniel Teleanu[1], R.I. Teleanu[1], R. Costea[6]

[1] University of Medicine and Pharmacy "Carol Davila", Bucharest, Romania

[2] Military Hospital "Carol Davila", Bucharest, Romania

[3] National Institute for Research and Development in Microtechnology, Bucharest, Romania

[4] Research Institute for Artificial Intelligence "Mihai Drăgănescu", Bucharest, Romania

[5] University POLITEHNICA of Bucharest, Romania

[6] University of Agricultural Sciences and Veterinary Medicine of Bucharest,

ABSTRACT

This article proposes a new methodology for preparing the stump from the forearm amputation stage, to facilitate its subsequent wireless connection to a neural exoprosthesis. This method will also allow the creation of exoprostheses capable of making movements of the thumb similar to those of a healthy hand. The article also presents a set of biomaterials needed in the amputation stage for affixing the motor nerve branches of the median and ulnar nerves to the muscles left in the amputation stump.

INTRODUCTION

Despite advances in medicine and surgery, amputation continues to be a large problem in the world. The World Health Organization statistics revealed that more than 50 million people (0.5% - 0.8% of world population) had limb loss [1] in the last ten years, and this number increases by at least one million every year [2]. The highest number of Upper Limbs amputations are in East central Asia (10 million lower limb, 7 million upper limb) followed by Europe (10 million lower limb, 4 million upper limb), South Asia (7 million upper limb, 4 million upper limb), Africa (3 million upper limb, 2 million upper limb), North America (3 million lower limb, 2 million upper limb) and the Middle East (4 million lower limb, 1 million upper limb), etc [3]. Most exoprostheses on the market have myoelectric control and offer only a few predefined functions which do not help patients carry out their basic daily activities: personal hygiene, food, maintenance, agreement, etc. The neural exoprostheses' finger movements are achieved with acquired neural signals from those parts of the median and ulnar nerves that remain in the amputation stump. The acquisition of distinct neural signals from these portions of the median and ulnar nerve, for the separate movement of each exoprosthesis finger is difficult to achieve as most of the motor branches of the two nerves (median and ulnar) are removed from the stump during amputation. What remain in the stump of these two nerves after amputation are only their main trunks, containing all of the motor fascicles, as these are difficult to identify and so, acquiring separate neural signals from each of them is difficult (fig. 1)

[4]-[5]. The global 3D structure of the ulnar nerve with all motor and sensory branches is presented in Figure 1.

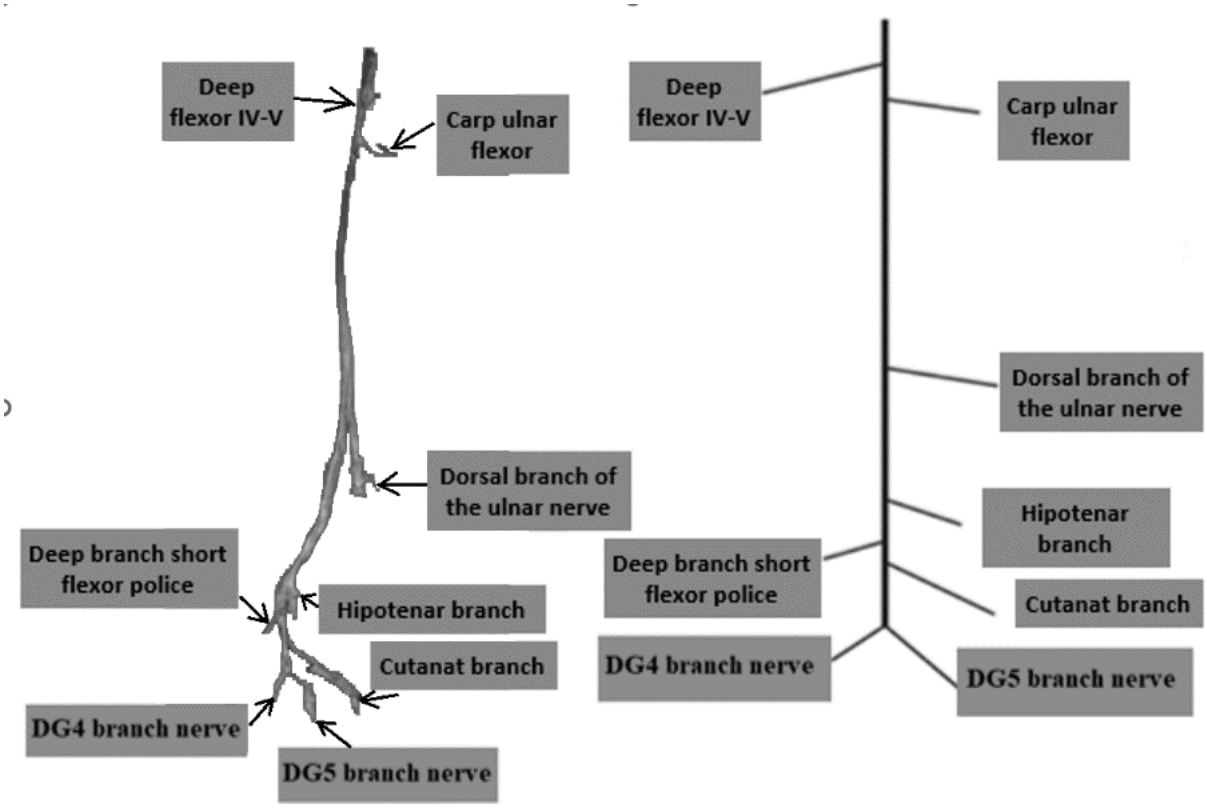

FIGURE 1 a) Fascicular Topography of the ulnar nerve in the forearm and palm for Neuroexoprostheses (left); b) The 3D modelling of ulnar nerve topography (right) [5]

EXPERIMENTAL

A domestic pig (Sus Scrofa Domesticus) experimental model was used due to its nerve similarities to humans regarding diameter, conduction, and impulse transmission. The experiment's methodology adhered to the guidelines outlined in the Public Health Service Policy on the Humane Care and Use of Laboratory Animals (2015). All surgical procedures were performed under general anesthesia, as follows: rapid administration of the premedication in the dorsolateral area of the gluteal muscle, using Ketamine 20 mg/kg and Xylazine 1 mg/kg for deep sedation and immobilization. After 10 minutes, venous access was performed using an 18-gauge catheter in the left lateral auricular vein. For induction of anesthesia, Propofol 3 mg/kg was administered intravenously, followed by intubation using a long-bladed laryngoscope, stylet, and 5.5 cuffed endotracheal tube. After obtaining an appropriate level of anesthesia, the experimental animal was positioned in lateral recumbency, in order to facilitate the approach to the deep peroneal nerve. Anesthesia was maintained on 1.5-2% isoflurane in 2 l/min oxygen. All the procedures from the animal experiments were approved by the Romanian Sanitary Veterinary Directorate (Protocol no. 20 from 9 July 2023) for studies involving animals and adhered to the guidelines outlined in the Directive 2003/65/EC of the European Parliament and of the Council of 22 July 2003 amending Council Directive 86/609/EEC on the approximation of laws, regulations and administrative provisions of the Member States regarding the protection of animals used for experimental and other scientific purposes [6].

Under general anesthesia, we scrubbed the area with antiseptic solutions and draped the hind limb with sterile towels. Starting from the medial aspect of the knee and extending towards the ankle, a 14 cm longitudinal incision was performed and followed up with blunt dissection to the fascial layer. A small section of the fascia was removed using fine forceps and retracted medially the long peroneal muscle underneath in order to expose the common peroneal nerve and further the deep peroneal nerve. Taking care not to injure the nerve and its blood supply, its dissection was continued towards the hoof maintaining its length as much as possible. After dissecting the nerve free from surrounding tissue, while carefully preserving epineuriem, a distal neurolysis was performed and the nerve was gently folded without creating tension. The nerve was secured and positioned in the septum between the long peroneal muscle and the peroneus tertius muscle to ensure protection by minimizing future exposure to fibrosis and neural tissue loss. Additionally, we anticipate the use of "wrap around" conduits (biodegradable such as collagen based or more active hydrogels made of poly(ethylene glycol)-poly(lactic acid) (PEG-PLA)46 that can release neurotrophin, which may aid in nerve viability.

Major vessels were ligated with non-absorbable suture to ensure hemostasis while preserving enough collateral branches at the stump level for soft tissue vascularization and skin flaps. The tibial and the fibular bone were then transected and smoothed using a rasp. The skin was sutured using skin flaps and a non-adherent dressing and soft padded bandage was applied. Routine post operative treatment (including pain management and antibiotic prophylaxis) followed with monitoring signs of wound healing complications.

Following complete healing of the stump, the pig was anesthetized in the same fashion and euthanised.

RESULTS AND DISCUSSION

The surgical technique explored in this study offers an approach to maximize nerve protection for the prospect of neuronal electrode implantation. One of the critical outcomes is the strategic placement of the nerve stump within muscle masses, which can potentially guard the nerve from mechanical injuries and other exogenous factors.

Additionally, the technique plans to adapt to current advancements in bioengineering by incorporating a 3D printed nerve conduit. This conduit, which can be formulated either from biodegradable collagen or hydrogels made of poly(ethylene glycol)-poly(lactic acid) (PEG-PLA)46, is not merely a passive protective layer, as it is designed to provide a sustained release of neurotrophins. Neurotrophins, as known growth factors, can potentially promote nerve health and regeneration.

This dual approach serves multiple purposes. First, by wrapping the nerve end with the specialized conduit, the technique actively attempts to minimize fibrosis and the adhesion of the nerve to adjacent muscular structures. Fibrosis and adhesions can pose significant challenges in nerve functionality and can complicate subsequent surgical interventions.

Furthermore, the overarching hope of this technique is to minimize, or potentially eliminate, the need for future surgical resecting the nerve end. Resection is typically necessitated to expose viable, healthy nerve tissue, especially before the implantation of an electrode. By preserving the health and

integrity of the nerve end through this novel technique, we might significantly reduce the necessity of such invasive procedures in future electrode implantations.

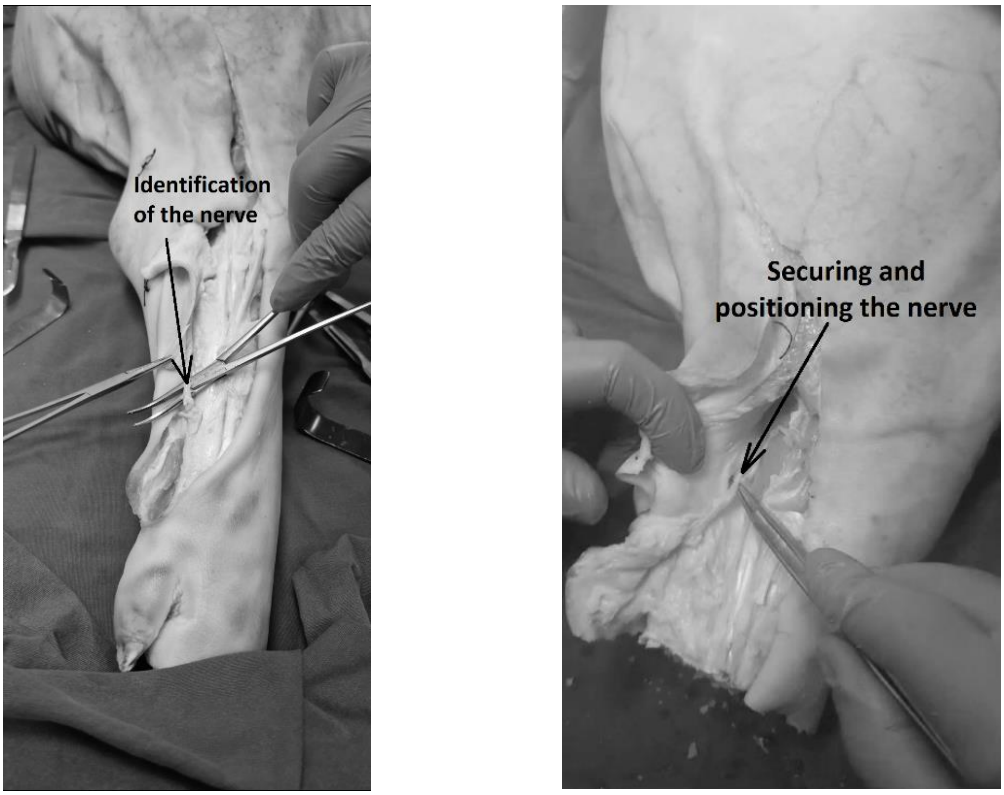

a) b)

FIGURE 2 a) Identification of the nerve before amputation; b) stump preparation with peripheral nerve preservation.

CONCLUSIONS

The new methodology implies that even from the amputation phase, the surgical team may identify the motor neural branches of the median and ulnar nerves that are functional and that can be kept in the stump. These motor nerve branches may be identified and integrated in the muscle masses in the amputation stump with appropriate medical methods and biomaterials. The methodology cannot be applied to all patients who are going to have a forearm amputation but it must be customized for each individual case. This method will facilitate the electrodes' implantation in the motor nerve branches from the patient's stump and their wireless connection to a neural exoprosthesis that will be able to perform movements similar to a healthy hand. The movements of the thumb in a healthy hand are made with 8 muscles, and if during the amputation as many nerve motor branches as possible, that stimulate these 8 muscles, are preserved then even more distinct neural signals will be able to be acquired from the amputation stump and many distinct movements of the thumb of the exoprosthesis will be ensured.

ACKNOWLEDGEMENTS

The work of this paper was done with financial support from NerveRepack project (Intelligent neural system for bidirectional connection with exoprostheses and exoskeletons), ID no. 101112347, Key Digital Technologies Joint Undertaking, 2023-2027.

REFERENCES

1. Jibby E. Kurichi, Barbara E. Bates, MD, Margaret G. Stineman, Amputation, *International Encyclopedia of Reabilitation* 2010.

2. A Market Landscape and Strategic Approach to Increasing Access to Prosthetic Devices and Related Services in Low - and Middle - Income Countries, AT2030 programme, Global Partnership for assistive technology, Clinton Health Access Initiative, April 2020.

3. McDonald, C.L.; Westcott-McCoy, S.; Weaver, M.R.;, Haagsma, J.; Kartin, D. Global prevalence of traumatic non-fatal major limb amputation, *Prosthetics and Orthotics International* 2021, 45(2), 105-114.

4. Delgado-Martínez, I.; Badia, J.; Pascual-Font, A.; Rodríguez-Baeza, A.; Navarro, X. Fascicular Topography of the Human Median Nerve for Neuroprosthetic Surgery, *Front Neurosci*. 2016, 10:286doi: 10.3389/fnins.2016.00286.

5. Oproiu, A.M.; Lascar, I.; Dontu, O.; Florea, C.; Scarlet, R.; Sebe, I.; Dobrescu, L.; Moldovan, C.; Niculae, C.; Cergan, R.; Besnea, D.; Cismas, S.; David, D.; Muraru, D.; Neagu, T.; Pogarasteanu M.E.; Stoica, C.; Edu, A.; Ifrim, C.F. Topography of the Human Ulnar Nerve for Mounting a Neuro-Prosthesis with Sensory Feedback, *REV. CHIM.* (Bucharest) 2018, 69(9), 2494-2497.

6. Directive 2003/65/EC of the European Parliament and of the Council of 22 July 2003 Amending Council Directive 86/609/EEC on the Approximation of Laws, Regulations, and Administrative Provisions of the Member States Regarding the Protection of Animals Used for Experimental and Other Scientific Purposes. Available online: https://eur-lex.europa.eu/legal-content/ENG/TXT/HTML/?uri=CELEX:32003L0065&from=NL (accessed on 12 July 2023).

ENHANCING PROSTHESIS FUNCTIONALITY USING FPGA CONTROL LOGIC

F. Istudor[1], D.C. Dragomir[1,2], C.A. Bratan[1,3], M. Dascălu[1,3], O. Datcu[1]

[1] University Politehnica of Bucharest, Splaiul Independentei 313, 060042 Bucharest, Romania, Corresponding Author : bratanandrei97@gmail.com

[2] IMT Bucharest, Erou Iancu Nicolae 126A, 77190 Bucharest, Romania

[3] RACAI, Romanian Academy Center for Artificial Intelligence, 13 September Boulevard, 050711 Bucharest, Romania

ABSTRACT

To contribute to the important research field aiming to offer patients with amputated limbs a life as close as possible to the one lived prior to the operation, this work implements and tests the control block for the forearm prosthesis equipped with DC motors and pressure *Velostat* sensors on an FPGA platform to ensure a controllable method of movement of the fingers and the possibility of incorporating haptic feedback into the algorithm. The five types of movement that the prosthesis can execute due to new algorithms are illustrated, the goal of the project being attained. Compared to previous microcontroller-based implementation, the FPGA platform enhances the functionality of the prosthesis due to the parallel operation of all fingers. Nevertheless, some hardware and software limitations are reported.

INTRODUCTION

The paper presents a reconfigurable logic implementation for the control block of a hand prothesis. The research in this area is motivated by the large number of patients with upper limb amputations and has direct social and economic interest [1, 2]. The goal of research in this field is to offer patients a pleasant appearance of prostheses, as much as possible many movements and functions achievable, mobility and reliability. Taking into consideration the products available on the market and/or presented in scientific literature, there is a significant interest in improving the functionality of protheses in affordable range of costs. Solutions reported in scientific literature for the control block of prostheses include hybrid actuation and myoelectric control [3], advanced signal processing techniques [4] and embedded deep learning-based control [5].

This project implements and verifies the viability of five basic functional movements using a prototype of a forearm prosthesis presented in previous papers [6, 7]. The forearm prosthesis is equipped with DC motors and pressure *Velostat* sensors. In previous work, the control was based on a microcontroller implementation using the Arduino development tools [7]. The most significant limitations of the control block are due to the sequential operation of the actuators. This paper presents an alternative FPGA implementation that enhances the functionality of the control block.

IMPLEMENTATION

The scheme of the control logic is shown in Figure 1. The sensor block receives and transmits informative signals regarding the environment and the current state of the prosthesis. The Analogue-to-Digital converter (ADC) transmits the digital state associated with each *Velostat* sensor. The signal generator provides the decision block with signals necessary for operation. The central block of this project, the decision block, aims to retrieve external information, generate, and propagate command signals for subsequent blocks. The movement controller transmits the signals necessary for the motion of the fingers, after accessing the signals of the decision block. Depending on the signals received from previous blocks, it will/ will not continue transmitting control signals. The signals necessary for a valid movement are transmitted through the finger controller. The actuation system block transforms electrical power into mechanical power. The devices used in this project are the DE1-SoC development board (with Cyclone V family FPGA device), DC motors 250:1 HPCB, drivers for DC motors, the magnetic encoder kit, *Velostat* sensors and the prosthesis prototype.

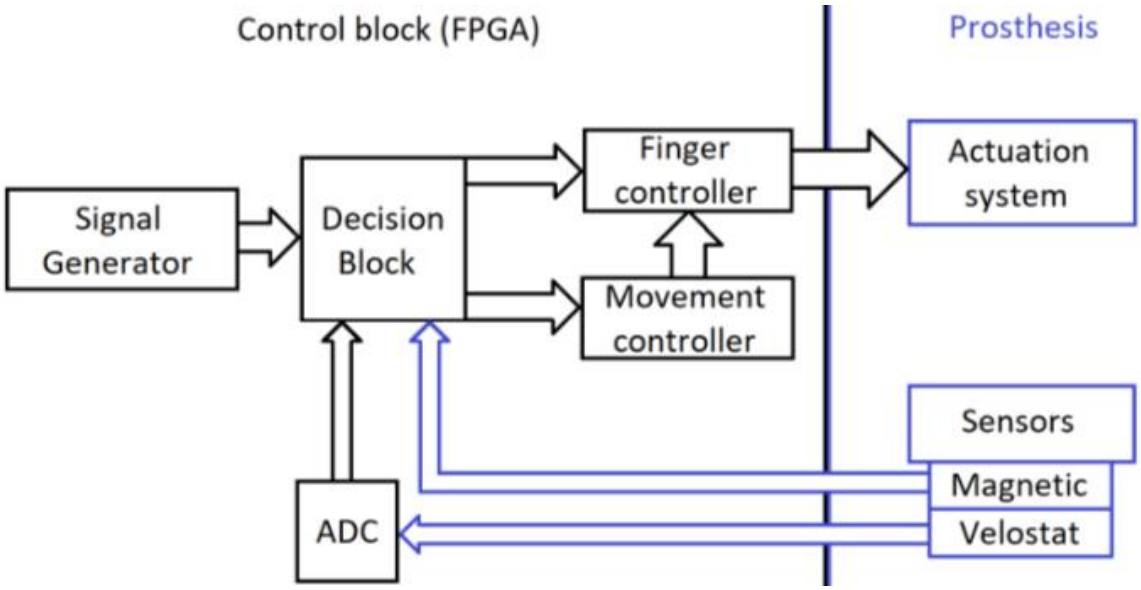

FIGURE 1 The scheme of the project.

RESULTS AND DISCUSSION

The digital design was done using Quartus Prime IDE and System Verilog HDL. The algorithms used in this project are implemented in different modules and the main TOP module was the control block for the prosthesis. An important step right after the implementation of the algorithms was to test them. The control block presents a wide range of adjustable parameters, the optimal value of which can only be determined by experimentation.

FIGURE 2 Practical examples of grabbing different objects.

An important impact on the operation of the prosthesis is to find the best combination for a series of adjustable parameters - the fill factor for the PWM signal transmitted to the drivers, initialization parameters for the control block of a finger and the parameters for the five movements. For this task, the utilized modules are adjusted such that the parameters can be modified using the mechanical inputs.

Eventually, the five types of movement that the prosthesis is able to execute are the full extension of the hand, two grabbing movements, seven sequential movements - sequential flexion of the little, ring, middle and index fingers, followed by the sequential stretching of the little, ring and middle fingers, movements for testing the parameters and movements needed to operate a mouse - 'click' and 'double-click'. Examples of grabbing movements are shown in Figure 2.

Comparing to previous implementations [6, 7], the parallelism of the FPGA-based control block offers the possibility to drive all 5 DC motors and therefore improves the mobility and speed of reaction.

CONCLUSIONS

The objective of this project has been achieved: the FPGA can control with good accuracy the prosthesis. Nevertheless, from the point of view of speed, the main limitations were mainly the supply and the fact that the FPGA and the prosthesis support a higher speed but, due to the algorithm, a part of the accuracy of movements is lost. If the movement speed is maintained at the tested values, movement accuracy is satisfactory and the internal finger position counters reflect reality in a good measure. There are some limitations from the hardware point of view: the limits of movement of the fingers, the reduced functionality of the little finger and the thumb. Moreover, some limitations come from the software: e.g. inaccurate stop motion conditions, the impossibility of calibration of some parameters.

ACKNOWLEDGMENTS

The prototype used in this research was developed during the ARMIN Grant (Arm Neuroprosthesis equipped with artificial skin and sensorial feedback) EEA, ctr. 8/2019. The control block was developed with financial support from the NerveRepack HORIZON KDT- JU-2022-2-RIA Project no. 1011120347/2023.

REFERENCES

1. Ziegler-Graham, K; MacKenzie, E.J.; Ephraim, P.L; Travison, T.G, Brookmeyer R. Estimating the prevalence of limb loss in the United States: 2005 to 2050, *Archives of Physical Medicine and Rehabilitation* 2008, 89(3), 422-429. doi: 10.1016/j.apmr.2007.11.005. PMID: 18295618.

2. McDonald, C.L.; Westcott-McCoy, S.; Weaver, M.R.; Haagsma, J.; Kartin, D. Global prevalence of traumatic non-fatal limb amputation, *Prosthetics and Orthotics International* 2020, 0(0). doi:10.1177/0309364620972258.

3. Guey, B.L. An Intelligent Prosthetic Hand using Hybrid Actuation and Myoelectric Control, PhD thesis, University of Leeds, January 2009.

4. Nguyen, A.T.; Drealan, M.W.; Luu, S.K.; Jiang, M.; Xu, J.; Cheng, J.; Zhao, Q.; Keefer, E.W.; Yang, Z. A Portable, Self-Contained Neuroprosthetic Hand with Deep Learning-Based Finger Control, *Journal of Neural Engineering* 2021, 1-20.

5. Dunai, L.; Novak, M.; García Espert, C. Human Hand Anatomy-Based Prosthetic Hand, *Sensors* 2020, 137-149.

6. Gheorghe, M.I: Dascălu, M; Vasiliu, F.C.; Dragomir, D; Franti, E. Tactile Feedback Through Velostat and Motion Algorithm for a Neural Prosthesis, CAS 2021 Proceedings, Octombrie 2021, Sinaia, Romania, pp.78-81, WOS:000853482700035.

7. Gheorghe, M.I: Dascălu, M; Opriș, C.O; Vasiliu, F.C.; Dragomir, D; Franti, E, Motion Algorithms for a Neuroprosthesis Equipped with Velostat Sensors, *Romanian Journal of Information Science and Technology*, ROMJIST 2022, 25(2), 246–259, WOS:000823109400010.

Monday 11 Sep. 2023	**SESSION 4A** Oral Presentations **Experimental and Manufacturing Techniques**
Session 4A Co-Chairmen:	**Evi Kontou,** Professor Emeritus, Mechanics Department, School of Applied Mathematical and Physical Sciences, National Technical University of Athens, Greece. **Olivier Dalverny,** 1LGP, INP/ENIT, University of Toulouse, France

COMPARISON OF MECHANICAL PERFORMANCE OF MULTI-MODIFIED CEMENTITIOUS MORTARS AND PASTES SENSORS

A.K. Thomoglou, M.G. Falara, F.I. Gkountakou, A. Elenas, C. E. Chalioris

Department of Civil Engineering Democritus University of Thrace, Xanthi, Greece

ABSTRACT

This comparative analysis focuses on evaluating the mechanical performance of nano-, micro-, and hybrid-reinforced cement mortars and pastes. Specifically, the flexural strength, compressive strength, and flexural toughness of multi-modified cementitious composites strengthened with single-walled carbon nanotubes (SWCNTs), micro-scale carbon fibers (CFs), and their hybrid combination are assessed. The investigation examines the impact of different scales of matrices (mortars and pastes) and varying amounts of nano-modified (0.1, 0.2, and 0.3 wt.% of cement) and micro-modified specimens (0.05, 0.1, and 0.5 wt.% of cement) in conjunction with the collaborative effect of carbon fibers. The comparison of the cement mortars and pastes' mechanical strength and toughness was assessed through 3-point bending and compressive tests on 4 cm × 4 cm × 16 cm and notched 2 cm × 2 cm × 8 cm prisms, respectively. The results reveal that even small quantities of nanotubes and CFs (0.1 wt.% SWCNTs and 0.5% CFs) significantly enhance the mechanical properties and energy absorption of plain cement paste and mortar. Subsequently, this research highlights the strong correlation of carbon multi-reinforcement of cementitious materials and provides new perceptions for the design of advanced multi-scale structural applications.

INTRODUCTION

The excellent mechanical properties of multi-modified cementitious pastes and mortars, attract the interest of researchers worldwide applying them in civil engineering constructions and applications. However, the functionalities of cement-based materials can be enhanced by incorporating carbon nanotubes, graphene, nanoparticles, and chemical additives with sensing abilities to monitor structural health and supplementary factors [1,2].

Previous studies have already revealed the beneficial enhancement of the mechanical performance of cement pastes and mortars by incorporating the optimal concentration of nanotubes (SWCNTs or MWCNTs) in the cement matrix [3,4]. Additionally, the influence of the different surfactants on carbon fiber dispersion as it turned out played an essential role in the mechanical performance and is still an open field for investigation [5,6]. However, the most impressive results are observed in the case of the synergistic effect of the hybrid incorporation of nano and micro reinforcement. Nevertheless, it is essential to simultaneously investigate the microstructure of the modified composites with non-destructive methods such as X-ray micro-CT [7-9].

This research aims to focus on evaluating crucial mechanical properties, such as compressive strength, flexural strength, and flexural toughness of the cement pastes and mortars. A correlation and regression analysis aims to highlight the relations between the mechanical properties of the two different materials, leading to a comprehensive analysis of their interdependencies. On the one hand,

correlation analysis is used to assess the relationship between compressive strength, flexural strength, and flexural toughness, by estimating the degree of association between these properties and consequently giving valuable evidence for material characterization. On the other hand, beyond correlation, regression analysis develops mathematical models which predict one variable in connection with the other variables' value [7,10,11]. These models beneficially evaluate the mechanical performance of cementitious materials in terms of different quantities of incorporated nanotubes, micro-fibers, and hybrid additives.

The results of these analyses will provide valuable tools for material characterization, performance prediction, and structural design in cementitious materials. By conducting this comparative analysis and providing the impact of advantages and limitations of the multi-modified composites, the researchers' community is leading to improve the design regulations for more effective and reliable engineering constructions.

MATERIALS AND METHODS

In this study, the cementitious materials mortars were cast using a type I standard Portland cement of 42.5 R. To ensure effective dispersion of the carbon nanotubes, nanotube suspensions were prepared in deionized mixing water containing the anionic surfactant sodium dodecyl benzenesulfonate (SDBS). The composition of the SDBS solution is as follows: $C1_2H_{25}C_6H_4SO_3Na$, which is a colorless salt consisting of various organic compounds. Aldrich and TBP (Tri-n-butyl phosphate) were used to obtain the aqueous/SWCNT/SDBS solutions [4,5]. The dispersion of SWCNTs is achieved using 60 minutes of ultrasonic energy, while CFs are incorporated through a dry-mix method (Figures 1 and 2).

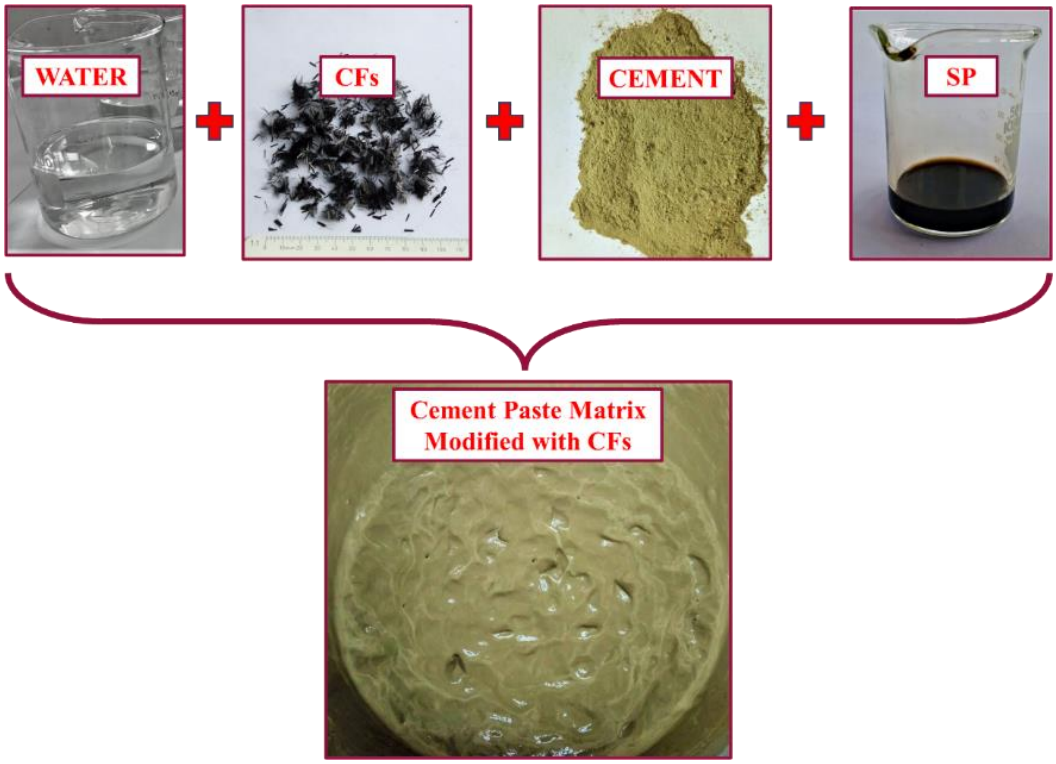

FIGURE 1 Dry mixing method of CFs incorporation into the cement paste matrix with the included materials.

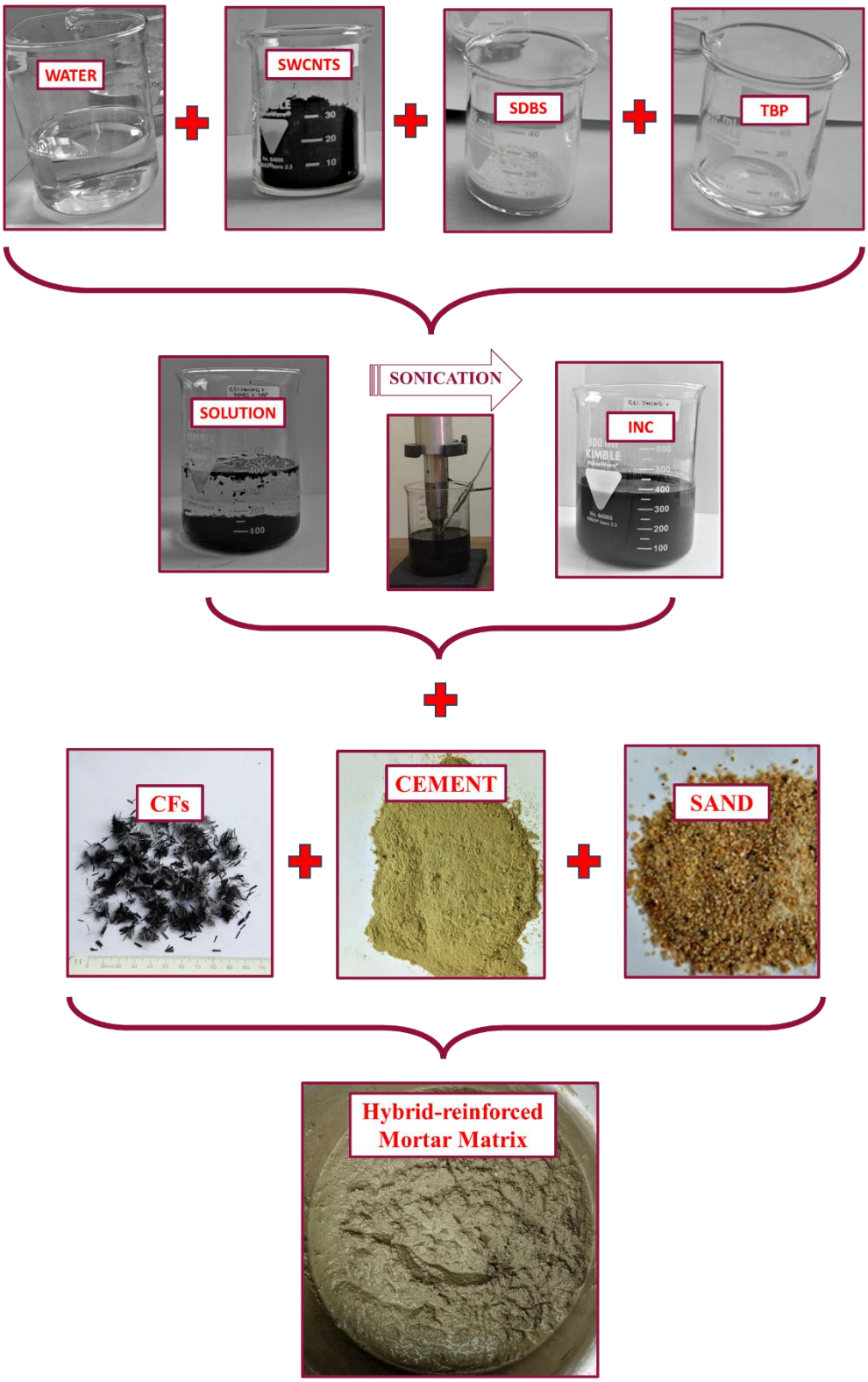

FIGURE 2 Hybrid reinforcement mixing with micro-fibers (CFs) and nanotubes (SWCNT).

The methodology of this study involved the development of mechanically advanced mortars with nano- and micro-enhancement using SWCNTs and CFs or hybrid, respectively, in varying concentrations. The best combination of nano- and micro-scale enhancements led to the creation of

a hybrid mortar with exceptional performance. Mechanical testing techniques were employed to characterize the flexural and compressive strength of the specimens. Three-point bending tests were conducted on 4 cm × 4 cm × 16 cm prisms according to EN 1015–11 standard, and flexural toughness was determined using notched 2 cm x 2 cm x 8 cm prisms based on the Linear Elastic Fracture Mechanics theory [3-5,7]. Compression tests were also performed on the halves of the prisms produced by the bending test. The mechanical testing was carried out using servo-hydraulic and closed-loop testing machines. Overall, this methodology enabled the assessment of the mechanical properties of the multi-modified cement pastes and mortars, providing valuable insights into their performance.

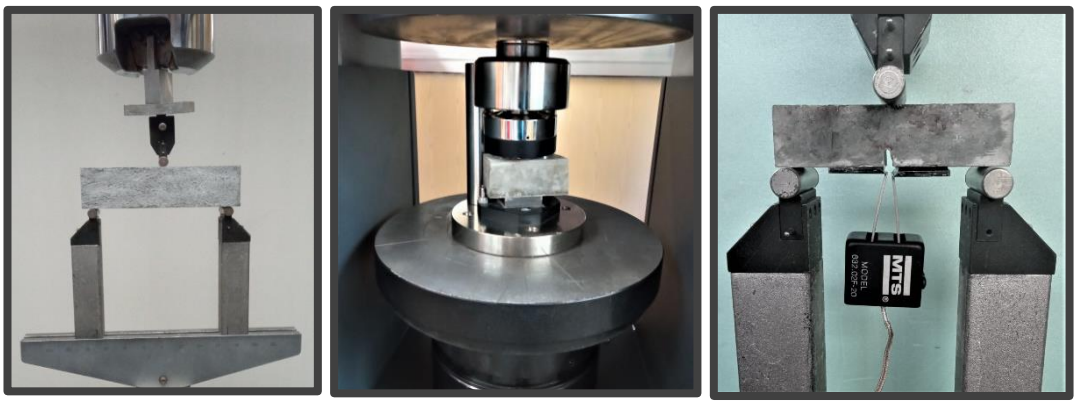

(a) (b) (c)

FIGURE 3 Experimental test set-up of a) 3-point bending of cementitious composite prisms, b) prism pieces compression, and c) mid-span notched prisms.

RESULTS AND DISCUSSION

The statistical analysis shows a strong relationship between the mechanical properties of mortars and cement pastes in terms of nano, micro, and hybrid reinforcement incorporated in the matrix. Correlation and linear regression analysis were performed to determine the best-fit relationship between the measured compressive, flexural strengths, and flexural toughness of the cement pastes and mortars.

The correlation analysis is illustrated in sub-Figures 4 a), c), and e). The results expose that the correlation coefficient between variables of flexural strength of the cement pastes and mortars is 0.98, indicating a positive correlation between the strengths (Figure 4a) with the augmentation of nanotube amount. The correlation coefficient between the compressive strength of the two types of cementitious composites demonstrates a good correlation with a coefficient of about 0.90 (Figure 4c) as the SWCNTs amount was improved. This indicates a negative correlation between these variables. The relationship between the flexural toughness of cement pastes and mortars is depicted in Figure 4 e). Specifically, it should be noted that there is a strong correlation with a coefficient r=0.99 as the reinforcement is enhanced [7].

The regression analysis considered the dependent variables of the mechanical properties with the variation of the reinforcement's concentration. These constants are determined through the regression analysis, along with the regression coefficients (R^2) are presented in Figures 4 b), d), and

f), illustrating the correlation between the flexural, compressive, and flexural toughness of the two different types of cementitious composites, the cement pastes and the mortars. Upon examining the plots, it is important to highlight that the highest R^2 values were observed in the correlation between flexural strengths of the cement pastes and mortars measured by the SWCNTs augmentation (R^2=0.983). Therefore, flexural strength may be considered a more suitable parameter than compression and flexural toughness for accurate predictions of cementitious composite properties. This finding aligns with previous researchers [7].

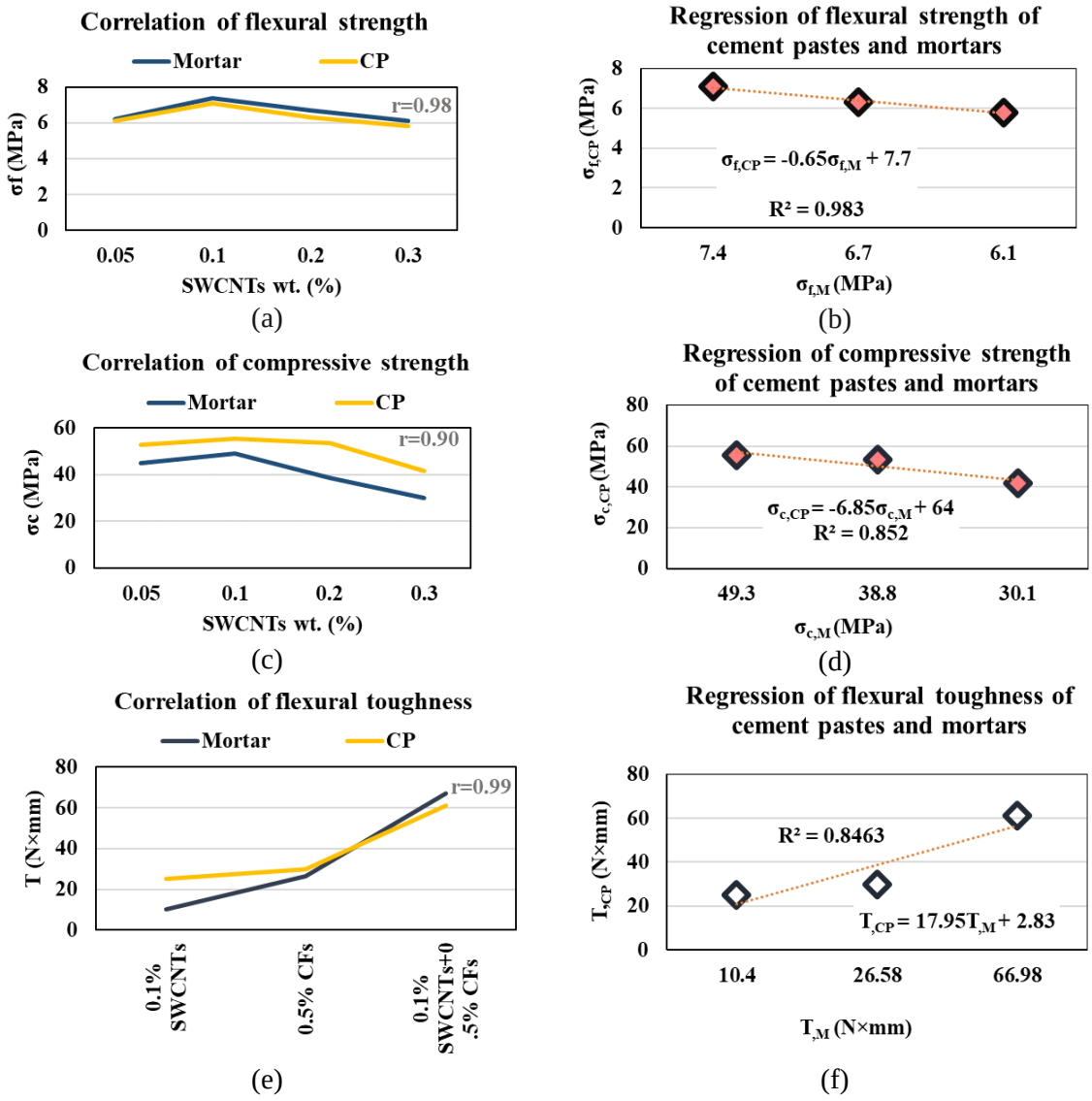

FIGURE 4 Correlation analysis between a), b) flexural strength, c), d) compressive strength, and regression analysis of e), f) flexural toughness of reinforced cement pastes and mortars with SWCNTs, CFs, and hybrid reinforcement.

CONCLUSIONS

This study aims to conduct a comparative analysis to explore the correlation between mechanical performance in two different materials: cement pastes and mortars. Specifically, a correlation and regression analysis gains insights into the flexural strength, compression strength, and flexural toughness of the two cementitious materials strengthened with nano, micro, and hybrid reinforcement. The most important results of this research are the following:

- The correlation analysis demonstrated positive relationships between the flexural strength of the cement pastes and mortars with the simultaneous augmentation of the nanotube amount. The correlation coefficient between these variables was found to be 0.98.
- The compressive strength of the cementitious composites showed a negative correlation with the concentration augmentation of SWCNTs and a correlation coefficient of about 0.90.
- The flexural toughness of cement pastes and mortars exhibited the strongest correlation with a coefficient of 0.99 as the reinforcement was enhanced.
- The highest regression coefficient R^2=0.983 value was presented in the correlation among flexural strengths of cement pastes and mortars, particularly with the SWCNTs concentration increase.
- Results reveal that flexural strength is a more reliable factor compared to compression and flexural toughness when predicting the properties of cementitious composites.

Overall, this comparative analysis contributes to the understanding of the mechanical performance of multi-modified cementitious mortars and paste composites identifying the strong relationship between the mechanical properties of mortars and cement pastes. By understanding the underlying relationships this kind of statistical analysis leads to the development of regression models which can be employed for predicting the parameters influencing the composites' performance.

ACKNOWLEDGMENTS

The European Union and Greek national funds, through the Operational Program Competitiveness, Entrepreneurship, and Innovation, under the call RESEARCH-CREATE-INNOVATE (HICOTEG-T1EDK-03482), have co-financed this research. The authors would like to express their gratitude for the valuable contribution from the collaborators at the Composite & Smart Material Laboratory of the Materials Science and Engineering Department of the University of Ioannina, who provided the carbon fibers.

REFERENCES

1. Tayeh, B.; Hakamy, A.; Fattouh, M.; Mostafa, S. The effect of using nano agriculture wastes on microstructure and electrochemical performance of ultra-high-performance fiber reinforced self-compacting concrete under normal and acceleration conditions. *Case Stud. Constr. Mater*. 2023, 18. e01721.

2. Jagadesh, P.; Nagarajan, V.; Karthik Prabhu, T.; Karthik Arunachalam. Effect of nano-titanium dioxide on mechanical properties of fly ash and ground granular blast furnace slag based geopolymer concrete. *J. Build. Eng*. 2022b, 61: 105235.

3. Thomoglou, A.K.; Falara, M.G.; Gkountakou, F.I.; Elenas, A.; Chalioris, C.E. Smart Cementitious Sensors with Nano-, Micro-, and Hybrid-Modified Reinforcement: Mechanical and Electrical Properties. *Sensors* 2023, 23, 2405.

4. Falara, M.G.; Thomoglou, A.K.; Gkountakou, F.I.; Elenas, A.; Chalioris, C.E. Hybrid smart cementitious materials incorporating ladder scale carbon fiber reinforcement: An experimental investigation, *Case Stud. Constr. Mater* 2023, 18, 2214-5095.

5. Thomoglou, A.K.; Falara, M.G.; Gkountakou, F.I.; Elenas, A.; Chalioris, C.E. Influence of Different Surfactants on Carbon Fiber Dispersion and the Mechanical Performance of Smart Piezoresistive Cementitious Composites. *Fibers* 2022, 10, 49.

6. Metaxa, Z.; Tolkou, A.; Efstathiou, S.; Rahdar, A.; Favvas, E.; Mitropoulos, A.; Kyzas, G. Nanomaterials in Cementitious Composites: An Update. *Molecules* 2021, 26, 1430.

7. Thomoglou, A.K.; Fantidis, J.G.; Voutetaki, M.E.; Metaxa, Z.S.; Chalioris, C.E. Mechanical Characterization of Nano-Reinforced Mortar: X-ray Micro-CT for 3D Imaging of Microstructure. *Eng. Proc*. 2023, 41, 4.

8. Fantidis, J.; Dalakas, A.; Potolias, C.; Karakoulidis, K.; Kogias, P. A Fast Neutron and Gamma Ray System for the Detection of Illicit Materials Based on Simple Isotopic Sources. *J. Eng. Sci. Technol. Rev.* 2016, 9, 52–58.

9. Kavvadias, I.E.; Tsongas, K.; Bantilas, K.E.; Falara, M.G.; Thomoglou, A.K.; Gkountakou, F.I.; Elenas, A. Mechanical Characterization of MWCNT-Reinforced Cement Paste: Experimental and Multiscale Computational Investigation. *Materials* 2023, 16, 5379.

10. Thomoglou, A.K.; Rousakis, T.C.; Achillopoulou, D.V.; Karabinis, A.I. Ultimate shear strength prediction model for unreinforced masonry retrofitted externally with textile reinforced mortar. *Earthq. Struct.* 2020, 19, 4411–4425.

11. Thomoglou, A.K.; Karabini, M.A.; Achillopoulou, D.V.; Rousakis, T.C.; Chalioris, C.E. Failure Mode Prediction of Unreinforced Masonry (URM) Walls Retrofitted with Cementitious Textile Reinforced Mortar (TRM). *Fibers* 2023, 11, 53.

ARTIFICIAL METER SCALE METASURFACES FOR MANIPULATION OF SEISMIC SURFACE WAVES

N. Aravantinos-Zafiris[1], A.G. Chronis[2], D.T.G. Katerelos[3], M.M. Sigalas[2]

[1] Department of Environment, Ionian University, Zakynthos, 29100, Greece. Corresponding Author: nikosaravadinos@gmail.com

[2] Department of Materials Science, University of Patras, Patras 26504, Greece.

[3] Department of Audio and Visual Arts, Laboratory of Applied Mechanics, Acoustics and Musical Instruments, Ionian University, Lixouri 28200, Greece.

ABSTRACT

In this work an artificial metasurface that consists of an arrangement of hollow square steel frames buried up to their half-length into the ground surface is examined numerically. The calculations of the response of the ground surface under the presence of the metasurface were performed by using the Finite Element Method. The numerical findings provide significant evidence of the attenuation of the incoming surface waves by the metasurface. The results of this research indicate that such metasurfaces could be applied for several types of ground vibrations attenuation applications such as seismic surface waves.

INTRODUCTION

Over the past two decades, the increasing scientific and technological interest on manipulation of elastic waves led to the study and fabrication of several types of metamaterials [1]. Among several types of metamaterials, seismic metamaterials in the meter scale have been recently studied and enriched the field of seismic isolation based on metamaterials [2]. In the wide field of metamaterials, metasurfaces provide as a very promising solution on the control of seismic surface waves [3]. At the geophysical scale there have been plenty of artificial and natural structures at the ground surface which could be considered as seismic metasurfaces [4]. Aravantinos-Zafiris and Sigalas recently studied numerically the seismic surface waves attenuation by the terraced slopes, a well-known technical landform [5]. In this work a new type of an artificial metasurface which could be applied for several types of ground vibration attenuations, including seismic surface waves attenuation, is examined numerically. The numerical findings of this research provide evidence that the response of the ground surface under the presence of the metamaterial is significantly affected by the periodic studied arrangement thus reducing the amplitude of the ground surface wave which is transmitted through the surface.

NUMERICAL SCHEME

The examined metasurface consists of an arrangement of hollow square steel frames which are buried up to their half-length into the ground surface as shown in the representative of the computational unit cell in Figure 1(a). The square steel frame has length L and thickness d as indicated in the top

view of the computational unit cell which is presented in Figure 1(b). The wave propagation was examined along the ΓX direction, as indicated in the first Brillouin zone of Figure 1(c).

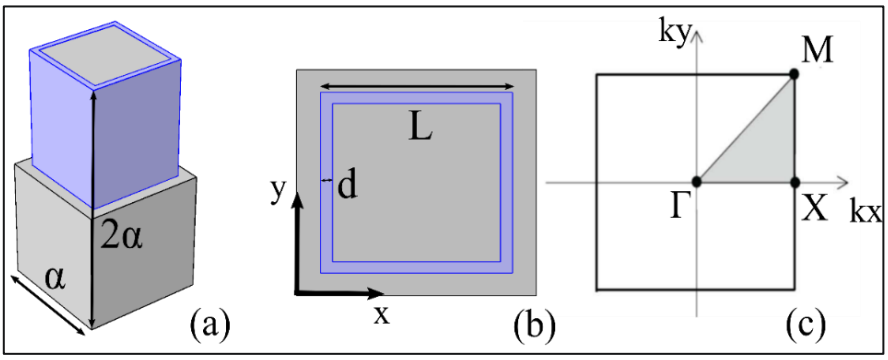

FIGURE 6 (a) The computational unit cell of the examined metamaterial. (b) Top view of the unit cell of the metamaterial where the length L of the square cavity, and d is the thickness of the square steel frame. (c) The first Brillouin zone with the relevant directions in k space

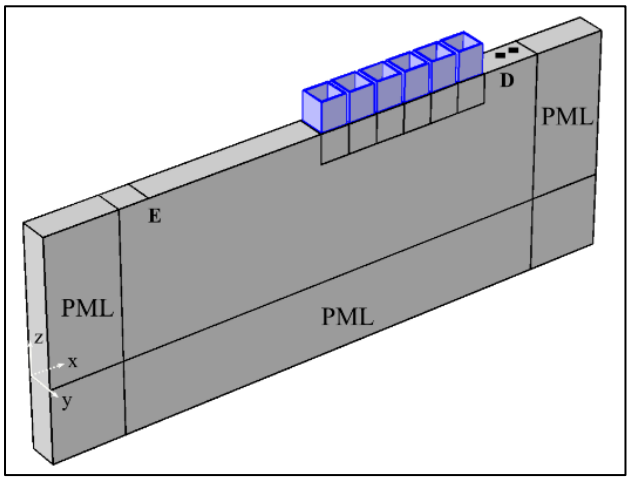

FIGURE 7 The computational half -space

The numerical model was utilized by solving the elastic equations using the Finite Element Method which is included in COMSOL Multiphysics®. The computational half-space which was used for the calculation of the response of the metasurface is presented in Figure 2. Free boundaries were considered at the top of the half-space. As an excitation (E), a prescribed displacement perpendicular to the surface was used and the results were collected from a detection point (D) right after the metasurface. To eliminate side reflections at the boundaries of the computational half-space Perfectly Matched Layers (PML) were considered at the sides and at the bottom of the half space. Small deformations were assumed so the linear elastic model could be applied. For the calculations of the present work the soil type had Young's Modulus $E = 20$ MPa, Poisson ratio $v = 0.3$ and density $\rho = 1800\ \mathrm{Kg/m^3}$ and it has already been used in literature [5]. In addition, the relevant parameters for steel were Young's Modulus $E = 207$ GPa, Poisson ratio $v = 0.3$ and density $\rho = 7784\ \mathrm{Kg/m^3}$.

RESULTS AND DISCUSSION

The numerical research included the calculation of the response of the structure for different geometric parameters of the square steel frame. The results provide significant evidence of the attenuation of the incoming surface waves by the metasurface. For the case where $L = 9$ m, $d = 1$ m, and $\alpha = 10$ m the calculated absolute value of the vertical component of the elastic field which is presented in Figure 3. The presented results show that the reduction on the relevant amplitude could reach two orders of magnitude, for the frequency zone around 4 Hz. Different configurations of the studied metasurface which were also examined show that such structures could stand as a promising solution on seismic surface waves attenuation strategies. It is important to be mentioned at this point that the results can be scaled in any other value of α, assuming that the parameters of the materials which were used in the calculations are independent of frequency. This scaling property of the examined structures is very crucial because it gives them a kind of “scale flexibility" allowing to adjust the lattice constant depended on the usage of each structure.

CONCLUSIONS

In this work a structure that consists of an arrangement of hollow square steel frames buried up to their half-length into the ground surface and could be considered as a seismic metasurfce is examined numerically.

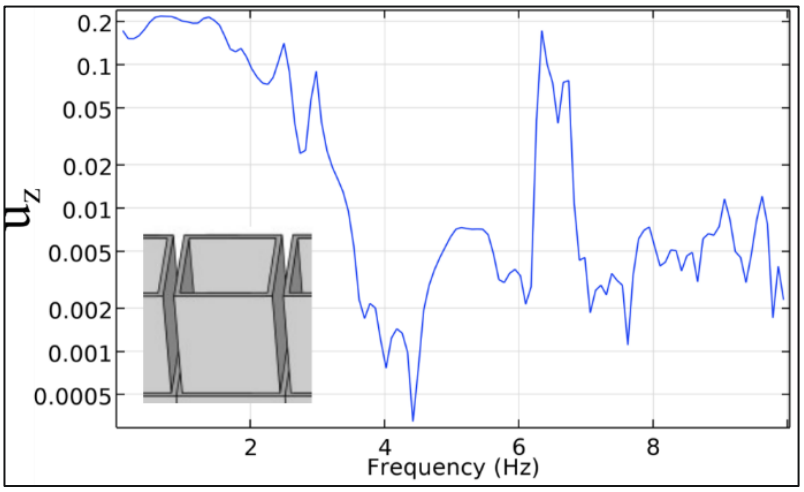

FIGURE 8 The absolute value of the vertical component of the incoming surface wave

The research showed that, for specific geometric parameters of the structure, the incoming elastic wave is significantly attenuated by the periodic arrangement thus leading to the conclusion that the proposed structure could provide a solution in the field of ground vibrations attenuation structures. Due to the "scale flexibility" of the examined structure it could potentially be suitable for several different ground vibration attenuation uses such as railway vibrations and seismic events.

REFERENCES

1. Deymier, P.A. Acoustic Metamaterials and Phononic Crystals, Springer Science & Business Media: Berlin, 2013, Vol. 173.

2. Brûlé, S; Enoch, S; Guenneau, S. Emergence of seismic metamaterials: Current state and future perspectives, *Physics Letters A* 2020, 384, 126034.

3. Assouar, B; Liang, B; Wu, Y; Li, Y.; Cheng, J.-C.; Jing, Y. Acoustic Metasurfaces; *Nature Reviews Materials* 2018, 3, 460.

4. Mu, D; Shu, H; Zhao, L; An, S. A Review of Research on Seismic Metamaterials, *Advanced Engineering Materials* 2020, 22, 1901148.

5. Aravantinos-Zafiris, N; Sigalas, M.M. Terraced slopes as large scale natural seismic metasurfaces; *Journal of Applied Physics* 2021, 130, 154901.

Monday 11 Sep. 2023	**SESSION 4B** Oral Presentations **Durability and Structural Health Monitoring-The AIOLOS project**
Session 4B Co-Chairmen:	**Alkis Paipetis,** Professor of Experimental Mechanical Behavior and Non-Destructive Testing of Composite Materials, Department of Materials Science & Engineering, University of Ioannina, Greece **D. Mouzakis,** Professor, Hellenic Army Academy, Department of Military Sciences Sector of Mathematics and Engineering Applications, Lab. of Applied Mechanics, Greece.

ENVIRONMENTAL AGING OF GNP REINFORCED GFRP: A DURABILITY STUDY

A. Ntaflos[1], D. Sioulas[2], N.M. Melanitis[2], G. Foteinidis[1], A.S. Paipetis[1]

[1] Composite and Smart Materials Laboratory, Department of Materials Science and Engineering, University of Ioannina, 45500, Ioannina, Greece, Corresponding Author A. Ntaflos: a.ntaflos@uoi.gr

[2]Marine Materials Laboratory, Hellenic Naval Academy, Hadjikyriakou Avenue, Piraeus, Greece

ABSTRACT

In this study, 1% wt. Graphene Nanoplatelet reinforced glass fiber epoxy composites were examined after environmental aging in high demand environments. Specimen were immersed in sea water as well as in a humidity chamber of 70 C and 85 % RH for two months and weighted frequently. Subsequently, the effect of GNP reinforcement on the water absorption rate and tensile strength was investigated. GNPs reduce the water uptake of the resin as much as 29 % and have higher retention rate on the mechanical properties after environmental exposure.

INTRODUCTION

Epoxies are some of the most versatile polymers used in almost all high-end industries. Glass Fiber-reinforced plastics (GFRP), with an epoxy matrix find applications in high-demand environments of high temperatures and moisture. Water molecules penetrate the resin and greatly decrease its properties by forming hydrogen bonds with the hydrophilic groups of the epoxy and reducing its durability [1].

Enhancing the epoxy with carbon nanofillers can reduce the degradation effect of the moisture and at the same time improve the mechanical properties, increasing their lifetime. Graphene is the most wanted material for the enhancement of polymeric matrices. The basic building block of all graphitic carbon allotropes (carbon nanotubes, fullerenes, and graphite) graphene as a nanofiller can improve both the mechanical properties of composites as well as its electrical properties due to its high electrical conductivity and high stiffness [2]. Practically, graphene is not suitable to disperse in epoxy, graphene nanoplatelets (GNPs) are commonly used as an alternative. GNPs are small stacks of graphene sheets used as an alternative to single-layer graphene due to their low manufacturing cost, remarkable characteristics, and capabilities for mass production ideal for industrial applications. Enhancing epoxy resins with GNPs can result in epoxy nanocomposites with improved barrier properties [3].

When a network of GNPs forms in the matrix, it can largely decrease the permeation of erosive substances like moisture by creating a “tortuous path’’ [4]. The graphene layers obstruct the water molecules forcing them to follow a complicated pathway rather than pass straight through the polymer. In this study, GNP-Epoxy GFRP will be evaluated in their durability after immersion in high temperature and moisture humidity chamber as well as after immersion in sea water.

EXPERIMENTAL

Materials

Graphene nanoplatelets with a few nanometers thickness, 300 g/m2 surface area (XGNPS C-300) and a Raman ID/IG ratio of 0.85 were provided by XGSciences, USA. Epoxy resin of commercial grade, diglycidyl ether of bisphenol A (DGEBA) Epikote 828 was provided by Hexion, along with complementary Epikure Curing Agent 866 and Epikure Catalyst 101 in a 10:8.3:0.15 mixing ratio. The epoxy's dynamic viscosity at room temperature was 10.000 mPa*s. E-Glass was provided by R&G composites of 240 g/m2. The mixing of the hardener and catalyst to the resin was done by hand and after that 15 minutes of de-gassing was done in a vacuum oven to remove trapped air inside the mixture. There was a two-step polymerization, 1 hour at 90°C and 2 hours at 150°C.

Specimen Preparation

Two types of specimens were manufactured, neat resin GFRPs and nanomodified GFRPs with 1% wt. GNPs. Tensile Strength testing was performed in unidirectional specimens according to ASTM D3039, the specimen dimensions were 200:12:1 mm. Tab dimensions was 4:12:1 mm.

Water Absorption

One set of specimens for each configuration was conditioned in a humidity chamber (hereafter known as "HT"), with static conditions of 70°C and 85% relative humidity and another set was immersed in sea (hereafter known as "IM") at temperatures ranging from 10-25 °C. The water-uptake was measured by frequently weighing the specimens during the immersion until saturation.

The Water Uptake (%) was measured using the equation:

$$WU(\%) = \frac{W_t - W_0}{W_0} * 100$$

W_t = Weight at time "t"

W_0 = Weight at time "0"

RESULTS AND DISCUSSION

Specimen reached saturation in the span of the first month (Fig.1). As expected, due to the elevated temperature, specimen immersed in the humidity chamber absorbed higher amounts of moisture than the specimen immersed in sea water. Despite the higher moisture content, the drop in tensile strength of the composites immersed in the humidity chamber was smaller, this is due to the two main mechanisms taking place during the immersion in the chamber, post-curing of the resin, increasing the crosslinking degree of the polymer. Hence the polymer becomes stiffer but the swelling of the resin due to absorbed moisture, degrades its mechanical properties. On the other hand, for the specimen immersed at sea, sea water corrosion as well as absorbed sea water had a detrimental effect on the mechanical properties (Fig.2).

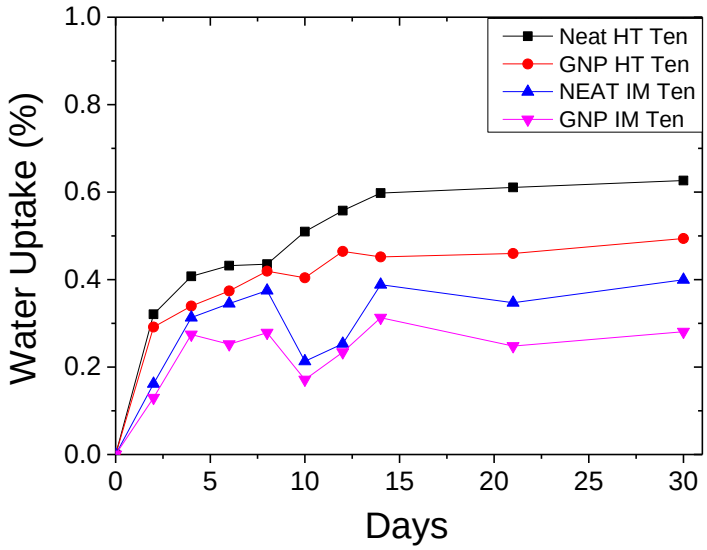

FIGURE 1 Water absorption the investigated matreials

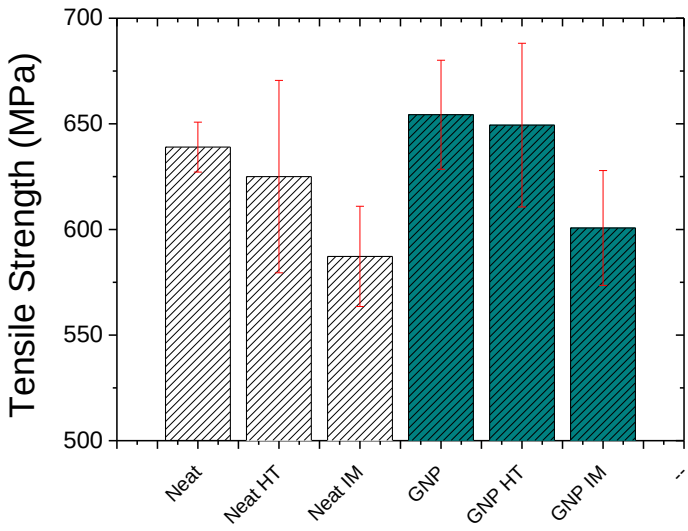

FIGURE 2 Tensile strength of the investigated materials

CONCLUSIONS

GNPs reduce the water uptake of the epoxy composite, reducing their water uptake up to 29 % for specimen immersed at sea and 21 % for specimen immersed in a humidity chamber with elevated temperature. GNP modified GFRP exhibited higher hydrothermal resistance over time compared to pure epoxy/glass composites with better mechanical performance and retention of tensile strength.

ACKNOWLEDGEMENTS

This research has been co-financed by the European Union and Greek national funds through the Operational Program Competitiveness, Entrepreneurship, and Innovation, under the call RESEARCH – CREATE – INNOVATE (project code: AIOLOS T2EDK-02971).

REFERENCES

1. Geim A.K. Graphene: Status and Prospects, *Science* 2009, 324(5934), 1530–34.

2. Baltzis, D.; Bekas, D.; Tsirka, K.; Parlamas, A.; Ntaflos, A.; Zafeiropoulos, N.; Lekatou, A.G.; Paipetis, A.S. Multi-Scaled Carbon Epoxy Composites Underwater Immersion: A Durability Study, *Composites Science and Technology* 2020, 199(July):108373, doi: 10.1016/j.compscitech.2020.108373.

3. Davidson, R.D.; Cubides, Y.; Fincher, C.; Stein, P.; McLain, C.; Xu, B.X.; Pharr, M.; Castaneda, H.; Banerjee, S. Tortuosity but Not Percolation: Design of Exfoliated Graphite Nanocomposite Coatings for Extended Corrosion Protection of Aluminum Alloys, *ACS Applied Nano Materials* 2019, 2(5), 3100–3116, doi: 10.1021/acsanm.9b00451.

4. Yan, L.; Zhang, H.; Huang, Z.; Bilotti, E.; Peijs, T. Graphite Nanoplatelet Modified Epoxy Resin for Carbon Fibre Reinforced Plastics with Enhanced Properties, *Journal of Nanomaterials* 2017, Article ID 5194872, 10 pp, doi: 10.1155/2017/5194872.

Tuesday 12 Sep. 2023	**SESSION 7B** Oral Presentations **Sustainability and Thermoelectric Energy Harvesting-The HICOTEG project**
Session 7B Chairmen:	**Alkis Paipetis,** Professor of Experimental Mechanical Behavior and Non-Destructive Testing of Composite Materials, Department of Materials Science & Engineering, University of Ioannina, Greece. **Alberto Damore,** Professor, Università degli Studi della Campania "Luigi Vanvitelli", Aversa, Campania, Italy,

MULTIFUNCTIONAL CEMENT COMPOSITES: EVALUATION OF THEIR ELECTRICAL, MECHANICAL AND PIEZORESISTIVE PERFORMANCE

A. Gkaravela, I. Vareli, N.-M. Barkoula, A.S. Paipetis

Department of Materials Science & Engineering, University of Ioannina, Ioannina, Greece

ABSTRACT

This research aims to evaluate the influence of different types of conductive additives on the electrical, mechanical and piezoresistive properties of cement- based composite materials. Four different systems reinforced with either 0.1 wt.% of SWCNTs or 0.1 wt.% CFs or with a combination of both fillers are investigated. The CNT/CF fillers can enhance the flexural and compressive strength and endow electrical properties and sensing abilities to the cement composites. Electrochemical Impedance Spectroscopy (EIS) was used to investigate the electrical properties of the cement composites during the hydration process. The hybrid system possessed the lowest values of impedance |Z| after 28 days of the hydration process. Furthermore, mechanical tests were conducted. The addition of 0.1 wt.% of CFs into the cement matrix resulted in 35% increase of the maximum flexural strength. Moreover, the hierarchical composite showed a 31% increase in the maximum compressive strength in relation to the cement paste.

INTRODUCTION

In the past decades, the construction industry is focusing on the development of smart structural materials. Nevertheless, the nature of the traditional cement imposes plenty of limitations on the development of more exploitable materials that could be used in advanced constructions. A smart approach to overcome these limitations and to acquire multifunctionality is the use of materials with high conductivity such as carbon nanotubes and/or carbon fibers as additives in cementitious matrices. The modification of cement pastes with high conductive additives such as carbon nanotubes (CNTs) and/or carbon fibers (CFs) are leading to multifunctional cement – based materials [1, 2]. During the hydration process, the interaction between the conductive filler and the cementitious matrix changes, affecting the properties of the overall composite material. Therefore, the development of these materials requires monitoring of these properties at all stages of the hydration as well as in their final stage. In this study, EIS is used, for monitoring the electrical properties during the structural evolution of cement-based composite materials with different types of fillers [3]. The changes of |Z| magnitude as the hydration process progresses demonstrate the existence of a conductive network from the fillers. Furthermore, mechanical tests were performed. The results confirmed the influence of the fillers in the mechanical properties. Finally, the ability to use these materials as piezoresistive sensors was investigated through the fractional changes of the resistance.

EXPERIMENTAL

In this study single wall CNTs (SWCNTs) are used for the production of the conductive dispersion. SWCNTs were in powder form provided by OCSiAl. For the dispersion of the CNTs a surfactant is required for homogenous dispersion [4]. Sodium dodecylbenzene sulfonate (SDBS), is used as a surfactant, which was purchased from Sigma Aldrich. Also, for the production of the micro-composites, Carbon fibers (CFs) are provided by Toray and finally, TITAN S.A. GREECE has provided the Ordinary Portland cement (OPC) CEM I 42.5 R. Aqueous dispersions are prepared using 0.1 wt.% of SWCNTs by cement weight while the CNTs/SDBS ratio is kept constant at 1:1. The dispersion of the CNTs in the deionized water was performed in a water bath for 60 min under sonication. In the case of hierarchical micro-composites, the same SWCNTs dispersion was coated on the CFs using a slot-die coating system in the Roll-to-Roll line of our laboratory. The cement nano- and/or micro- composites were mixed using the dispersions, the chopped carbon fibers, the hierarchical chopped fibers and Portland cement at a water-to-cement ratio (w/c) of 0.5 by weight. Four different batches of cementitious composites were prepared while keeping constant regardless the type, the percentage of the amount of the filler at 0.1 wt. % by cement weight. The first one contained SWCNTs, the second one CFs, the third batch contained the hierarchical CFs and finally the fourth, the hybrid composites, contained both SWCNTs & CFs. The mixtures were stirred for 10 min for homogenized using an IKA® EUROSTAR control 200P4 equipped with an R1381 propeller stirrer and casted into a polymer-based mold. For monitoring the electrical properties during the hydration process, the EIS measurements are conducted by using two-point electrodes technique. The two electrodes were directly inserted into the fresh mixture to monitor the changes of the parameters from the beginning of the hydration procedure until the age of 28 days. The measurements were conducted by a digital Impedance Analyzer in a frequency range from 10^{-1} Hz to $5*10^{6}$ Hz provided by Zurich Instruments, Switzerland. The mechanical tests as well as the piezoresistive response of the cement composites are performed using a Universal Testing Machine WDW-100 by Jinan S.A.

As far as it concerns the dispersion of the carbon fibers into the cement matrix, a dry mix was carried out. The chopped fibers were incorporated into the cement powder followed by mechanical agitation.

RESULTS AND DISCUSSION

The magnitude of the impedance or |Z| as a function of frequency at the end of the hydration process (28th day) is presented in Fig.1. As it is shown for the micro-composite with 0.1wt.% CFs, the values of |Z| are approximately the same in relation to the cement reference, therefore, there was no formation of a conductive network. On the other hand, the nano-composite with 0.1wt.% SWCNTs presented lower values in the impedance |Z| and the conductive network is achieved. A notable result is that the hierarchical micro-composite with 0.1wt.% of hierarchical CFs showed approximately the same values with the nano-composite. This behavior validates the contribution of the CNTs in the formation of the conductive network. A fact that becomes even more evident in the case of the hybrid composite since the impedance |Z| demonstrated the lowest values in relation to the other nano- and micro- composites.

The type of the reinforcement also affected the mechanical properties of the cement composites. The micro-composite with 0.1 wt.% of CFs presented the highest values while the hybrid composite presented the lowest values of flexural strength. However, in the case of the maximum compressive

strength the hierarchical composite demonstrated the highest values followed by the nanocomposite with 0.1 wt.% of SWCNTs and the hybrid composite. Nevertheless, the addition of the fillers, despite the type of the filler, reduced the nano- and micro- pores of all samples since the mechanical properties are enhanced.

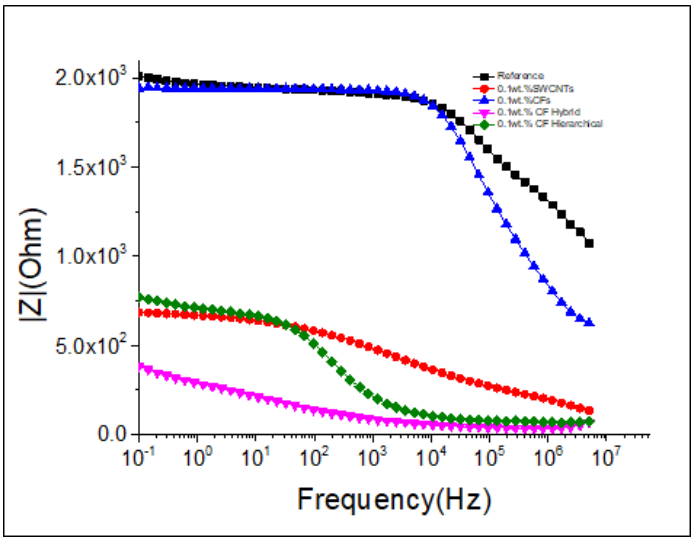

FIGURE 9 Impedance |Z| plots at the end of the hydration process.

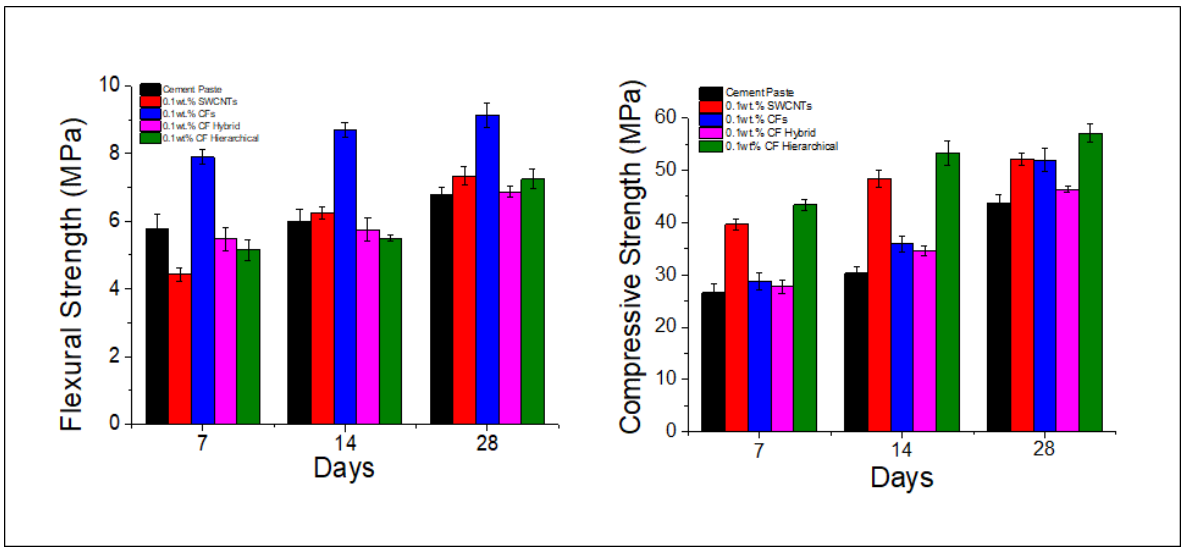

FIGURE 10 Maximum Flexural & Compressive Strength during the hydration process.

CONCLUSIONS

This study experimentally investigated the influence of different types of conductive additives on the electrical, mechanical properties of cement- based composite materials. The results of the EIS measurements showed that the combination of both SWCNTs and CFs as hybrid composite resulted the lowest values of the impedance |Z|. This result confirmed the significant contribution of the CNTs in the formation of a conductive network since the composite enhanced only with CFs did not present any conductive network. Finally, the addition of all fillers increased the mechanical properties in relation to the cement paste. The composite reinforced with CFs presented the highest values of flexural strength while the hierarchical composite presented the highest values of compressive strength.

ACKNOWLEDGEMENTS

This research has been co-financed by the European Union and Greek national funds through the Operational Program Competitiveness, Entrepreneurship and Innovation, under the call RESEARCH – CREATE – INNOVATE (project code: HICOTEG-T1EDK-03482).

REFERENCES

1. Vareli, I.; Tzounis, L.; Tsirka, K.; Kavvadias, I.E.; Tsongas, K.; Liebscher, M.; Elenas, A.; Gergidis, L.N.; Barkoula, N.,-M.; Paipetis, A.S. High-performance cement/SWCNT thermoelectric nanocomposites and a structural thermoelectric generator device towards large-scale thermal energy harvesting, *J Mater Chem C.* 2021, 9(40), 14421–38.

2. Li, V.C. High-Performance and Multifunctional Cement-Based Composite Material, *Engineering* 2019, 5(2), 250–60, https://doi.org/10.1016/j.eng.2018.11.031.

3. Hu, X.; Shi, C.; Liu, X.; Zhang, J.; de Schutter, G. A review on microstructural characterization of cement-based materials by AC impedance spectroscopy, *Cem Concr Compos* 2019, 100(March), 1–14. https://doi.org/10.1016/j.cemconcomp.2019.03.018.

4. Gkaravela, A.; Vareli, I.; Bekas, D.G.; Barkoula, N.M.; Paipetis, A.S. The Use of Electrochemical Impedance Spectroscopy as a Tool for the In-Situ Monitoring and Characterization of Carbon Nanotube Aqueous Dispersions, *Nanomaterials* 2022, 12(24).

SELF-POWERED STRUCTURAL HEALTH MONITORING OF THERMOELECTRICALLY ENABLED CFRP COMPOSITES

L. Koutsotolis, A. Voudouris Itskaras, P. Georgakis, A.S. Paipetis*

*Composite and Smart Materials Laboratory, Department of Materials Science and Engineering, University of Ioannina, GR-45110, Ioannina, Greece, *E-mail: paipetis@uoi.gr*

ABSTRACT

The scope of this study is to exploit the thermal energy harvesting and the self-sending capabilities that multifunctional composites may provide to achieve self-powered Structural Health Monitoring (SHM) in Carbon Fiber Reinforced Polymers (CFRP). To do so Single-Walled Carbon Nanotubes (SWCNT) are used to print Thermoelectric Generators (TEG) onto glass-fiber fabrics. The TEGs are subsequently integrated as a top-ply lamina into CFRPs, from which specimens are extracted. Specimens are subjected to mechanical testing, while their electrical response is simultaneously recorded to fulfil Structural Health Monitoring (SHM). Initially the electrical resistance of the carbon fibers and the TEG is recorded. Then the current generated by the TEG is suppled into the CFRP, while the voltage change is measured. Results reveal that the multifunctional composites can be inherently used to fulfil for SHM purposes. When the generated current is supplied into the material a self-powered SHM process is successfully accomplished.

INTRODUCTION

Composites are being used in various critical applications such as aerospace, due to their outstanding mechanical properties in combination with their low weight. Multifunctional composites are emerging as a promising technology to further reduce their weight and increase their efficiency. Multifunctional materials fulfil more functionalities apart from the primary structural (1). Self-sensing is a feature that electrically conductive composites possess. In the Electrical Resistance Chance Method (ERCM) the relative resistance change is used as an indicator of the material's structural health. The method has been successfully employed to diagnose the structural integrity of CFRPs (2) as well as GFRPs modified with CNTs (3). Thermal energy harvesting is another functionality recently demonstrated on composites. The energy conversion relies on the thermoelectric effect and is achieved through a TEG. Literature reports on various thermoelectric composites including GFRPs (4) and CFRPs (5). This study aims to combine the two aforementioned functionalities to realize self-powered SHM on composites. Results reveal that the herein proposed approach is successfully implemented.

EXPERIMENTAL

To prepare the thermoelectric inks the TUBALL SWCNT from OCSiAL were used, while SDBS from Sigma-Aldrich was employed as surfactant agent. PEI from Sigma-Aldrich and PEDOT:PSS from Agfa were used to appropriately dope the CNTs. To manufacture the laminates a unidirectional glass fiber fabric from FIBERMAX and a unidirectional fabric comprising stitched T700 carbon fiber

tows from Toray were used. The Araldite LY5052/Aradur 5052 resin system was employed as the matrix of the laminate. Stirring and sonication cycles were applied for the homogenization of the inks. Thermoelectric generators (TEGs) were fabricated by alternately depositing p- and n- type ink onto the glass fiber fabric. Laminates with $[0/90]_{2s}$ carbon fiber fabric + $[0]_2$ glass fiber fabric were manufactured by hand and cured in a hot-press. The glass fiber fabric on the surface had the printed TEGs while the other served as an insulator. The laminate and its lay-up are depicted in Figure 1. Specimens were extracted from the laminates and had tabs and electrodes attached to them. Two different electrode configurations were used leading to two different types of measurements. In the first case electrodes were mounted onto the edges of the TEG and the conductive carbon fibers. In the other case the electrodes mounted on the TEG were also attached to the edges of the specimen so that the generated current is supplied into the carbon fibers. Another pair of electrodes was attached to conduct the electrical measurements. The specimens were subsequently subjected to mechanical testing while electrical measurements were simultaneously conducted. In the first case the electrical resistance of both the TEG and the fibers was recorded and correlated to the structural integrity of the laminate. In the second case the electrical voltage was recorded, and the $\Delta V/V_o$ was used as a strain/damage index.

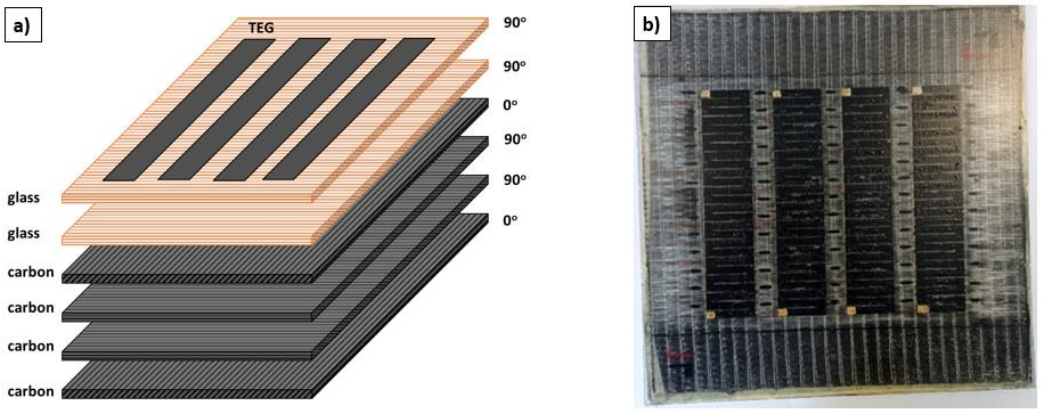

FIGURE 1 Multifunctional laminate. a) lay-up b) top view.

RESULTS AND DISCUSSION

The electrical resistance change is successfully employed to monitor the structural health of the multifunctional composites during tensile, cyclic and fatigue loading. Resistance gradually increases with loading and abruptly increases when damage occurs. The resistance change of the TEG validates and supports the findings of the resistance change of the carbon fibers. However, the electrical signal produced form the carbon fibers is more sensitive than the one produced from the TEG. Furthermore, it provides information about the structural integrity of the whole composite, while the signal from the TEG only reflects the strain of the surface. When the thermoelctrically generated current is supplied into the carbon fibers and the voltage is measured a self-powered SHM process is achieved. The voltage change has the same behavior as the resistance change. Namely it increases with strain and damage. The correlation between the voltage and the external resistor's resistance can be explained by typical thermoelectric output curves.

CONCLUSIONS

The electrical resistance change of the carbon fibers and the TEG, which is a continuous conductive path, is directly related to the structural integrity of the material. Strain of the material manifests as gradual increase of the resistance while damage is indicated by an abrupt increase. Simultaneously recording the resistance of the specimen and the TEG validates the findings. When the generated current is used as a power source self-powered SHM is accomplished. The electrical voltage exhibits behavior similar to the resistance. It increases gradually with the applied load and sharply during failure.

ACKNOWLEDGEMENTS

The research work was supported by the Hellenic Foundation for Research and Innovation (HFRI) under the 3rd Call for HFRI PhD Fellowships (Fellowship Number: 6574).

REFERENCES

1. Chung, D.D.L. A review of multifunctional polymer-matrix structural composites, *Compos Part B Eng*. 2019, 160 (November 2018), 644–60.

2. Grammatikos, S.A.; Paipetis, A.S. On the electrical properties of multi scale reinforced composites for damage accumulation monitoring. *Compos Part B Eng* 2012, 43(6), 2687–96, http://dx.doi.org/10.1016/j.compositesb.2012.01.077.

3. Thostenson, E.T.; Chou, T.W. Carbon nanotube networks: Sensing of distributed strain and damage for life prediction and self healing, *Adv Mater*. 2006, 18(21), 2837–41.

4. Karalis, G.; Tzounis, L.; Tsirka, K.K.; Mytafides, C.; Voudouris, I.A.; Liebscher, M.; Lambrou, E.; Gergidis, L.N.; Barkoula, N.-M.; Paipetis, A.S. Advanced Glass Fiber Polymer Composite Laminate Operating as a Thermoelectric Generator: A Structural Device for Micropower Generation and Potential Large-Scale Thermal Energy Harvesting, *ACS Appl Mater &amp, Interfaces*. 2021 May, 13(20), 24138–53.

5. Karalis, G; Tzounis, L.; Tsirka, K.; Mytafides, C.K.; Liebscher, M; Paipetis, A.S. Carbon fiber/epoxy composite laminates as through-thickness thermoelectric generators, *Compos Sci Technol* 2022, 220, 109291, https://doi.org/10.1016/j.compscitech.2022.109291.

Tuesday 12 Sep. 2023	**SESSION 8B** Oral Presentations **Bioengineering**
Session 8B Co-Chairmen:	**Doina Ramona Manu,** Center for Advanced Medical and Pharmaceutical Research, "George Emil Palade" University of Medicine, Pharmacy, Science and Technology of Targu Mures, Romania **T. Katsila**, Head of the Laboratory of Biomarker Discovery & Translational Research Institute of Chemical Biology, National Hellenic Research Foundation, Greece

3D NON-CONDUCTIVE VS. CONDUCTIVE BIOMEDICAL SCAFFOLDS: BIODEGRADATION AND BIOCOMPATIBILITY STUDY UNDER ELECTRICAL EXPOSURE

D.V. Portan[1*], S. Mamali[1], V. Kostopoulos[2], T. Katsila[3], P. Zoumpoulakis[3,4], P. Mallis[5], E. Michalopoulos[5], A. Koliadima[6]

[1]Department of Mechanical Engineering and Aeronautics, Laboratory of Biomechanics and Biomedical Engineering, University of Patras, 26504 Patras, Greece, [*]E-mail: portan@upatras.gr

[2]Department of Mechanical Engineering and Aeronautics, Applied Mechanics & Vibrations Laboratory, Uni-versity of Patras, 265 04 Patras, Greece

[3]Institute of Chemical Biology, National Hellenic Research Foundation, Athens, Greece

[4]Department of Food Science and Technology, University of West Attica, Athens, Greece

[5]Hellenic Cord Blood Bank, Biomedical Research Foundation Academy of Athens, 4 Soranou Ephessiou Street, 115 27 Athens, Greece

[6]Physical Chemistry Laboratory, Department of Chemistry, University of Patras, 26504 Patras, Greece

ABSTRACT

The scope of the present investigation was to elaborate a multifunctional scaffold that positively impacts the *in vitro* response in human cells, by combining balanced mechanical properties, biocompatibility, growth factor delivery capacity and conductivity. Two types of scaffolds were 3D printed: *(1)* PLA as control material and *(2)* CNTs reinforced PLA as a conductive material. SEM imaging indicated that stem cells migrated in the scaffolds. A 24 hours dynamic stirring experiment with scaffold immersed in cell culture medium demonstrated that the composite filament was more fragile which influenced the biodegradation rate. This means that conductivity was gained, while mechanical resilience was lost to an extent. A current field was applied to human stem cell seeded in the conductive scaffolds. The study showed that the electric field impacted cells communication which resulted in improved extracellular matrix formation, but it did not influence other processes such as adhesion or mineralization.

INTRODUCTION

The electricity generated inside the body serves for the control and operation of nerves, muscles, and organs. Decades ago, it has been found that an electric or a magnetic field applied within appropriate thresholds are tolerated by or even improve the *in vitro* behavior of mammalian cells [1]. Direct current (DC) electrical stimulation has been shown to have remarkable effects on regulating cell behaviors [2]. Without bioelectricity, a DNA molecule could not stay together. Every cell in our body has a membrane potential equivalent to a voltage gradient of some 10,000,000 V/m, a massive force that many proteins therein will feel. Even red blood cells that do not have nuclei possess a membrane potential. So, it seems a cell can exist without genetic material but not without bioelectricity [3].

In vitro fabrication of tissues and the regeneration of internal organs are no longer regarded as science fiction but as potential remedies for individuals suffering from chronic degenerative diseases. Tissue engineering has generated much interest from researchers in many fields, including cell and molecular biology, biomedical engineering, transplant medicine, and organic chemistry. Attempts to build tissues or organs *in vitro* have utilized both scaffold and scaffold-free approaches [4]. However, in order to build an optimum micro-environment that can support the tissue growth process, we need to transfer as many natural parameters of the human body as possible to the *in vitro* setup. The understanding of human cells response to every single parameter and how to enhance the rate of tissue build-up is the key to a successful outcome. The effect of several substrate characteristic on cell populations has been widely studied: *(1)* Topographical cues such as roughness have been used as a culture strategy to improve the secretory capacity and enrich the immunomodulatory phenotype of mesenchymal stem cells [5]; *(2)* Mechanical properties such as stiffness influences cells multiplication and migration; *(3)* Material conductivity under electric stimulation alters protein adsorption and nerve cell interactions [6][7]; and *(4)* Administration of active molecules through a passive or active drug delivery system can substantially impact efficacy and biocompatibility of biomaterials. Multi-functionality by introduction of multiple biomaterial key properties is challenging but necessary. Also, the two-way study of *(i)* material damage in response to cells invasion while in humid environment in correlation with *(ii)* key biomarker analysis of cells when in contact with the biomaterial will offer an overall characterization of this complex *in vitro* system and will elucidate several crucial aspects for the elaboration of innovative biomaterials.

The scope of the present investigation was to study and draw conclusions related to several parameters involved in a complex *in vitro* experimental setup that combined two types of scaffolds, non-conductive PLA and conductive CNTs reinforced PLA scaffolds respectively, in contact with human stem cells, in the presence and without an electric field. The focus was on the biodegradation rate of the scaffold and the release of several cells biomarkers in response to the micro-environment.

EXPERIMENTAL

Manufacturing of the 3D Scaffolds

An Ultimaker 2+ connect 3D printer was used to manufacture the biomedical scaffolds from PLA filaments provided by Ultimaker company and conductive CNTs reinforced PLA filament provided by AlfaOhm. Scaffolds pore sizes were 250 and 500μm. Scaffold parameters were designed using Ultimaker Cura 5.1.1 software. The program has ready-made parameters for PLA printing; however, some parameters were modified. According to the specification of AlfaOhm filament, the printing temperature and the printing platform temperature range from 190^0 to 210^0 C and 0 to 50^0 C respectively. For the successful printing, we have set the temperatures to 260^0 C and 60^0 C, and a maximum allowed printing speed (10 mm/s).

Investigation of scaffolds absorption/ biodegradation

The absorption and the biodegradation capacity of the scaffolds was investigated to estimate the ability of the scaffolds to store antibiotics or to incorporate bioactive agents. According to the preliminary studies, the maximum adsorption/desorption of liquid from PLA scaffolds happened in the first day of immersion. A 24-hour experiment was carried out to better study these behaviors. 24 scaffolds were fabricated for each design: *(i)* 500μm pore size PLA and *(ii)* 500μm pore size CNTs reinforced PLA. Scaffolds were immersed for 24 hours in mesenchymal stem cell culture medium

consisting of water, proteins and salts, namely Alpha Minimal Essential Medium, with 10% Fetal Bovine Serum, 50 μg/mL Amphotericin B, 25 μg/mL Gentamicin, 50 μg/mL L-ascorbic acid.

A dynamic experiment was performed with a magnetic stirrer; scaffolds were placed for 24 h in the aforementioned culture medium at room temperature. The dynamic agitation experiment has been adapted to simulate the *in vivo* environment through induced flow of physiological fluid. Three samples of each scaffold type were extracted every 3 hours. The weight of the scaffolds was measured before and after immersion. Immersed scaffolds were dried for a short time to eliminate the surface fluid before weight measurement.

Cell culture and biomarker analysis

Wharton's Jelly Mesenchymal Stem Cell (WJ-MSCs) were isolated from the human umbilical cords (hUCs) and delivered by the Hellenic Cord Blood Bank (HCBB). Cells were isolated according to a previously described protocol [8],[9]. Cells were further seeded in the scaffolds at a density of ~50,000 cells/cm^3. The seeding procedure consisted in depositing the diluted cells that were floating in medium in the scaffolds (100 μl/ scaffold) through micro-pipetting. Scaffolds with cells were incubated for three hours to allow the adhesion to the substrate. After that, cell culture medium was added to each well until the scaffold was completely immersed. Biomarker measurements (osteopontin - OPN, osteocalcin - OC, alkaline phosphatase – ALP, total protein - TP) were performed for different incubation no. of days (1, 3, 7, 15, 22). For cells imaging with a scanning electron microscope, scaffolds were washed with PBS and cells were fixated with a 1:1 Glutaraldehyde 4% v/v and Paraformaldehyde 4% v/v mixture for 20 minutes. Samples were washed again with PBS, dried and gold sputter coating was applied for the SEM imagining of the cells in the scaffolds. A JSM-6610 Series Scanning Electron Microscope (SEM) model has been used for imaging.

Electrical stimulation of cells

The cells deposited in electrically conductive scaffolds were exposed to the electrical stimulation (100 mV) for 2 hours/ day, for the first 3 consecutive days of incubation. The stimulation device and the experimental setup may be seen in the images in Fig.1.

(a) (b)

FIGURE 1 Setup for electrical exposure of samples: (a) sample container with electrodes and (b) the stimulation device in the incubator, connected with a DC power supply

RESULTS AND DISCUSSION

SEM imaging

The migration of WJ-MSCs on the PLA and the CNTs reinforced PLA scaffolds may be observed in the images in Fig.2. Upon cell attachment to the scaffold, the cells begin to interact with each other and with the environment, creating 'bridges' by growth factors release. The ability to adhere and interface is an indication of the scaffold's ability to contribute to the formation of functional tissues that can integrate with the environment and perform physiological functions. As observed, cells spreading very well on both PLA and CNTs reinforced PLA scaffolds, showing that both are biocompatible.

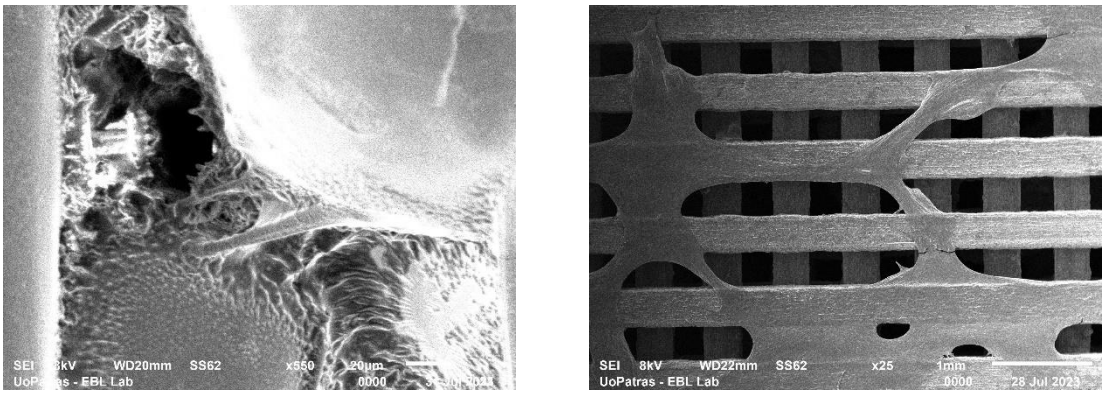

(a) (b)

FIGURE 2 WJ-MSCs spreading on the fiber of the scaffolds: (a) PLA and (b) CNTs reinforced PLA

Investigation of scaffolds absorption/ biodegradation

A representative diagram of the weight loss/ gain of scaffolds may be seen in Fig.3. It may be seen that the weight percentage variation of PLA and CNTs reinforced PLA is different. The reinforced PLA has initially (at 6 hrs immersion) a greater weight comparing to pure PLA. It is known that the presence of carbon nanotubes increases the adsorption and absorption capacity of fluid due to their surface composition that allow chemical interactions at binding sites with molecules and proteins. CNTs are also characterized by hydrophobicity as well as a rough surface, thus favoring protein adsorption. In general, the incorporation of carbon nanotubes favors protein adsorption rather than liquid absorption. This contributes to the faster biodegradation of the scaffold due to filament damage. Furthermore, in terms of robustness of CNTs reinforced PLA scaffold, CNTs contribute to faster degradation since the filament is not compact and presents discontinuities comparing to the pure PLA. Moreover, CNTs form aggregates and affect the overall structure making it more fragile.

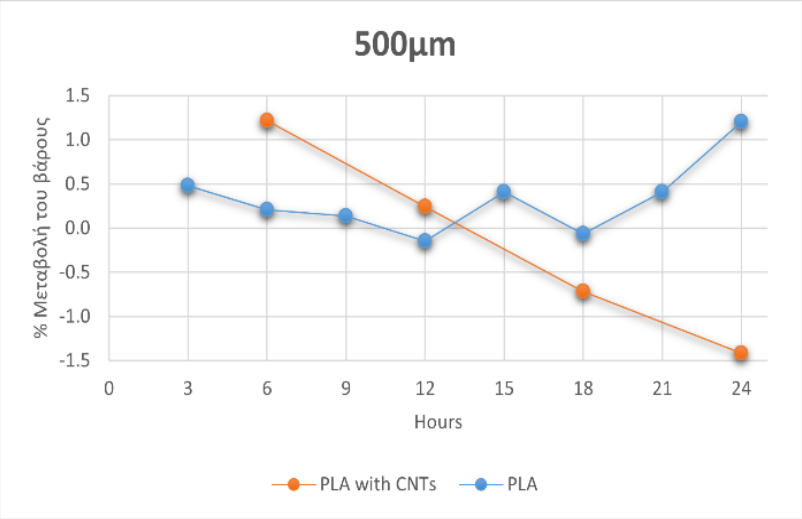

FIGURE 3 Weight loss/ gain profile in PLA vs. CNTs reinforced PLA scaffolds

Cell culture and biomarker analysis

Osteopontin (OPN) is a secreted glycoprotein. that has a variety of roles including cell adhesion, migration, cell signaling, and cell survival [10]. Regulation of OPN expression is consistent with a multiplicity of functions for OPN that involve specific structural motifs in both the synthesis and resorption of bone [11]. Most Osteocalcin (OC) secreted by osteoblasts is incorporated into the organic matrix that will later ossify into bone, however, a small fraction is secreted into the circulation. For this reason, OC was considered a bone formation marker and OC concentration correlates with direct measurement of bone formation [12]. However, it was later found that elevated levels of OC inhibit bone formation and function as a hormone [13]. Alkaline Phosphatase (ALP) increases inorganic phosphate local rates and facilitates mineralization as well as reduces the extracellular pyrophosphate concentration, an inhibitor of mineral formation [14]. Total Protein (TP) is a known marker of osteoblast phenotype and plays a fundamental role for the quality of osteoblasts adhesion on substrates [15].

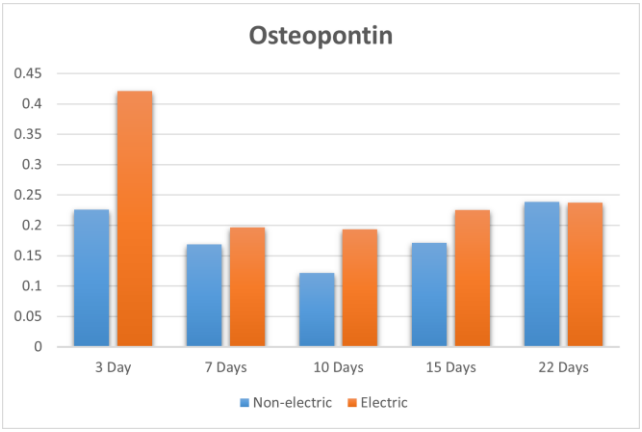

FIGURE 4 OPN levels in cells seeded in non-electrical vs. electrical substrates

In the diagram in Fig.4, we observe the variation of the OPN level in cells when seeded on non-electrical vs. electrical substrates. After 3 days of incubation with a 2 hours daily electrical stimulation of the electrical substrates, cells express quite high levels of osteopontin. This is normal because cells *in vitro* do not have the naturally formed extracellular matrix that exists *in vivo;* after placing them in the synthetic micro-environment, they start building the extracellular matrix around to form tissue.

This process continues with less intensity after the third day of incubation. However, cells activity on electrical substrates is much more pronounced. This can be also observed after 10, 10 and 15 days of incubation. In day 22 the level of OPN is almost similar in cells for both non-electric and electric substrates, which indicates that human cells tend to reach a balance and finally adapt, if the minimal micro-environmental conditions are accomplished. However, the path to reach this state is important in the process of implant biorecognition. *In vivo*, higher amount of OPN can be associated to a more robust connection between the tissues surrounding the biomaterial and the implant itself. This time gap shows that when on a substrate, cells firstly connect between them by building the extracellular matrix and subsequently adhere to the underneath material.

The total protein quantity is related to the cell adhesion process to a substrate. Levels are generally elevated, but they have the tendency to decrease between days 3 and 10 and they finally reach higher values in day 22. This tendency of decreased release of a substance can be also observed in the case of other biomarkers. While OPN level starts decreasing tremendously after day 3 of incubation, the total protein quantity lightly decreases after the third day.

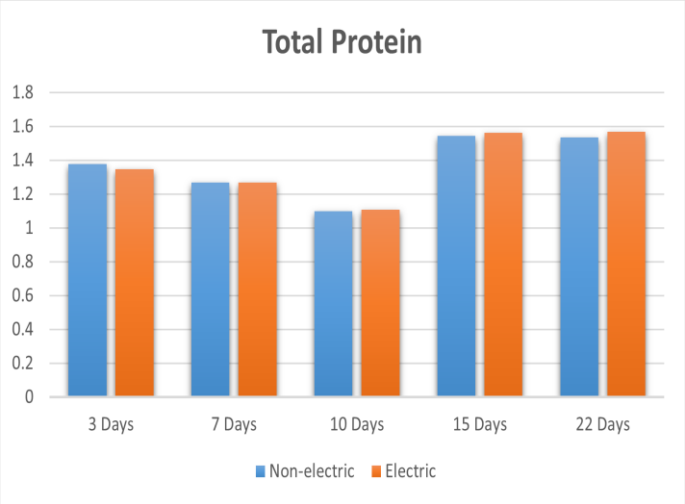

FIGURE 5 TP level in cells seeded
in non-electrical vs. electrical substrates

Related to TP, there is no significant difference between levels in cells on non-electric and electric scaffolds (Fig.5). This indicates that the electric field does not play a key role in the adhesion process. It has been several times proved that the main parameter to influence the adhesion efficiency of cells on an implant is the stiffness [16], while electricity influences other processes of critical importance such as adaptation to substrate material.

It was further found that the electricity does not contribute to raising the OC levels. Actually, electricity is generally related to the nervous tissues, and it is known to be the most important parameter for the communication between cells. Finally, alkaline phosphatase levels increase gradually, and this is expected, being associated to mineralization which is a phase that comes later in the cycle of the cell life. Mineralization is also influenced by the available space for cells multiplication. More precisely, as cells develop and occupy the scaffold, their multiplication rate decreases. Multiplication/ proliferation and mineralization are competitive processes which means. The intense multiplication was detected in the first 3 days of incubation, while mineralization is pronounced after day 7 and levels are higher in day 22. Again, electricity does not influence the mineralization process.

CONCLUSIONS

The study focused on the 3D printing manufacturing of conductive and non-conductive PLA scaffolds with the purpose of using them in biomedical applications. The printing parameters were adjusted to produce scaffolds made of PLA and CNTs reinforced PLA; filaments were provided by European companies. There was no significant difference between the printing parameters for the two types of filaments, showing that the matrix material (PLA) is the basic ingredient in the manufacturing process. The choice of the CNTs reinforced PLA was made to confer multi-functionality to the scaffold by allowing transfer of electricity to human cells when *in vitro*. The profile of the results of a 24 hrs absorption/ biodegradation dynamic stirring experiment performed in cell culture medium showed that the reinforced PLA is structurally more fragile comparing to the pure PLA. Although the fluid uptake is initially higher in the scaffold produced with the composite filament, its degradation rate is considerably accelerated after 6 hours of immersion. The PLA scaffold can be used as a longer-term drug delivery system as it keeps absorbing fluid for 24 hrs comparing to the scaffold made of CNTs reinforced PLA which is less efficient in this direction, and after 6 hrs of immersion starts biodegrading without further absorption.

Wharton's Jelly Mesenchymal Stem Cells were seeded in the two types of scaffolds. In the case of the conductive scaffold exposure to an electric field (100 mV) has been applied for 2 hrs/day for 3 consecutive days. The investigation of several biomarkers demonstrated that the exposure to electricity improved the communication between cells and thus the formation of extracellular matrix especially within the first 3 days, but it had no significant influence on other cellular processes (adhesion and mineralization).

The present investigation shows that the electricity is not directly involved in the process of bone formation but is very important for the communication between cells and for the connection with the biomaterial, and subsequently for the adaptation process of surrounding tissue to an implant.

ACKNOWLEDGEMENTS

This research is supported by the European Regional Development Fund of the European Union and Greek national funds through the Operational Program Competitiveness, Entrepreneurship and Innovation, under the call RESEARCH—CREATE—INNOVATE (project code: T2EDK-03847).

REFERENCES

1. Fiorani, M.; Cantoni, O.; Sestili, P.; Conti, R.; Nicolini, P.; Vetrano, F.; Dachà, M. Electric and/or magnetic field effects on DNA structure and function in cultured human cells, *Mutation Research Letters* 1992, 282(1), 25-29.

2. Zhao, Z.; Zhu, K.; Li, Y.; Zhu, Z.; Pan, L.; Pan, T.; Borgens, RB.; Zhao, M. Optimization of Electrical Stimulation for Safe and Effective Guidance of Human Cells, *Bioelectricity* 2020, 2(4), 372-381.

3. Djamgoz, M.B.A.; Levin, M. Bioelectricity: A Quick Reminder of a Fast-Advancing Discipline!, *Bioelectricity* 2020, 2(3), 208-209.

4. Nakayama, K. In Vitro Biofabrication of Tissues and Organs, *Biofabrication* 2013, 1–21.

5. Rosado-Galindo, H.; Domenech, M. Substrate topographies modulate the secretory activity of human bone marrow mesenchymal stem cells, *Stem Cell Res Ther* 2023, *14*, 208.

6. Kotwal; A.; Schmidt, C.E. Electrical stimulation alters protein adsorption and nerve cell interactions with electrically conducting biomaterials, *Biomaterials* 2001, 22, 1055, 1064.

7. Wang, S.; Guan, S.; Sun, C.; Liu, H.; Liu, T.; Ma, X. Electrical stimulation enhances the neuronal differentiation of neural stem cells in three-dimensional conductive scaffolds through the voltage-gated calcium ion channel, *Brain Research* 2023, 1798, 148163.

8. Chatzistamatiou, T.K.; et al., Optimizing isolation culture and freezing methods to preserve Wharton's jelly's mesenchymal stem cell (MSC) properties: an MSC banking protocol validation for the Hellenic Cord Blood Bank, *Transfusion* 2014, 54(12), 3108-3120.

9. Kozaniti, F.K.; Manara, A.E.; Kostopoulos, V.; Mallis, P.; Michalopoulos, E.; Polyzos, D.; Deligianni, D.D.; Portan, D.V. Computational and Experimental Investigation of the Combined Effect of Various 3D Scaffolds and Bioreactor Stimulation on Human Cells' Feedback, *Appl. Biosci*. 2023, 2, 249-277.

10. Tarrant, J. 4.15 - Emerging Translatable Safety Biomarkers, Editor(s): Chackalamannil, S.; Rotella, D.; Ward, SE. Comprehensive Medicinal Chemistry III, Elsevier, 2017, pp. 255-284.

11. Sodek, J.; Chen, J.; Nagata, T.; Kasugai, S.; Todescan, R Jr.; Li, IW.; Kim, RH. Regulation of osteopontin expression in osteoblasts, *Ann N Y Acad Sci*. 1995, 760, 223-41.

12. Di Medio, L.; Brandi, ML. Chapter Three - Advances in bone turnover markers, Advances in Clinical Chemistry 2021, 105, 101-140.

13. Komori, T. Functions of Osteocalcin in Bone, Pancreas, Testis, and Muscle, *Int J Mol Sci.* 2020, 21(20), 7513, doi: 10.3390/ijms21207513.

14. Vimalraj, S. Alkaline phosphatase: Structure, expression and its function in bone mineralization, *Gene* 2020, 754, 144855, doi: 10.1016/j.gene.2020.144855.

15. Feier, A.M.; Portan, D.; Manu, D.R.; Kostopoulos, V.; Kotrotsos, A.; Strnad, G.; Dobreanu, M.; Salcudean, A.; Bataga, T. Primary MSCs for Personalized Medicine: Ethical Challenges, Isolation and Biocompatibility Evaluation of 3D Electrospun and Printed Scaffolds, *Biomedicines* 2022, 10, 1563.

16. Kozaniti, F.K.; Deligianni, D.D.; Georgiou, M.D.; Portan, D.V. The Role of Substrate Topography and Stiffness on MSC Cells Functions: Key Material Properties for Biomimetic Bone Tissue Engineering, *Biomimetics* 2022, 7, 7.

Wednesday 13 Sep. 2023	**SESSION 11A** Oral Presentations **Interfaces and Interphases**
Session 11A Co-Chairmen:	**Kalliopi Artemi Kalteremidou,** Department of Mechanics of Materials and Constructions (MeMC), Vrije Universiteit Brussel (VUB), Brussels, Belgium. **Olesja Starkova,** Institute for Mechanics of Materials, University of Latvia, Riga, Latvia.

NUMERICAL FINITE ELEMENT ANALYSIS OF THE CHASSIS OF A ROBOTIC EQUIPMENT FOR HANDLING DRILLING PIPES

M. Ciolcă, T.E. Brănescu, Daniel Vlăsceanu

*Department Strength of Materials, Faculty of Industrial Engineering and Robotics, National University of Science and Technology POLITEHNICA Bucharest, ROMANIA, c*orrespondence to: miruna.ciolca@upb.ro

ABSTRACT

Currently, in the drilling equipment development market, several problems are encountered regarding the optimization of the way of working in practical projects. To ensure an optimized, short-term, and useful process for operators, some of the companies specialized in this field propose a series of fixed equipment, whose purpose is to store the pipes used in the drilling process. The problems encountered in these proposals relate to the fact that there is a limit on the capacity of storing and transporting pipes, so if it is necessary to increase the pipes quantity, it will be done manually by the operators. This can affect the operators health because the drilling process requires heavy drilling pipes [1].

INTRODUCTION

The use of mobile drilling wells, for in-depth drilling, represents a challenge for specialized companies because they often work in hard-to-reach areas, and operators can encounter difficulties due to the varied working conditions such as: high or low temperature, wind, rain, snow etc. For these reasons, the companies that manufacture drilling equipment seek to bring to the market proposals that optimize the process carried out in the field. A frequently encountered problem in well drilling is the transport of the equipment from the rig to the drilling site. Drill pipes represent the piping used on drilling rigs. They come in a variety of sizes, with usually large dimensions which make them difficult to handle.

The operators take the pipes from the storing area and insert them with one end into a drill pipe partially inserted into the ground, and with one end into the drilling equipment. A problem encountered in this case is the fact that the weight of each pipe transported manually can endanger the operator's health. Thus, companies come up with proposals to ease the drilling process. The existing solution on the market is the implementation of an equipment that is fixed on the drilling rig to store these heavy objects. To automatize the pipes handling process, specialty companies propose a series of robots attached to this equipment, which will handle the pipe from the area where it is initially stored, into the drilling head [4].

The problems encountered with these systems are related to the fact that the number of stored drill pipes is limited. The drilling rig, although mobile, cannot move during the drilling process, this would be expensive and risky due to the coaxiality between the drilling bit and the drill string. Thus, in this case, the pipes are manually transported by the operators to the drilling site.

The proposed solution consists of the implementation of a mobile system for drill pipes storage, capable of moving to different places, independent of the drilling rig and which also contains a robotic system necessary to handle the pipes (FIGURE 1).

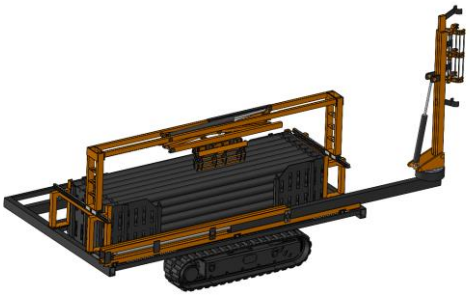

FIGURE 1 Proposed equipment for handling drill pipes.

From a mechanical point of view, the equipment is structured in several systems as follows:

A. The chassis is the basic structure of the assembly. The entire system moves on tracks. The material used is structural steel, with rectangular profiles of the following dimensions: 120x100 mm, 100x80 mm, 60x40 mm, the thickness of the material being 5 mm (Figure 2.a.).

B. The support in which the drill pipes are stored (Figure 2.b.) has a capacity of 49 pieces, each having a diameter of 101.6 mm and a length of 3,110 mm. One drill pipe mass is 60 kg.

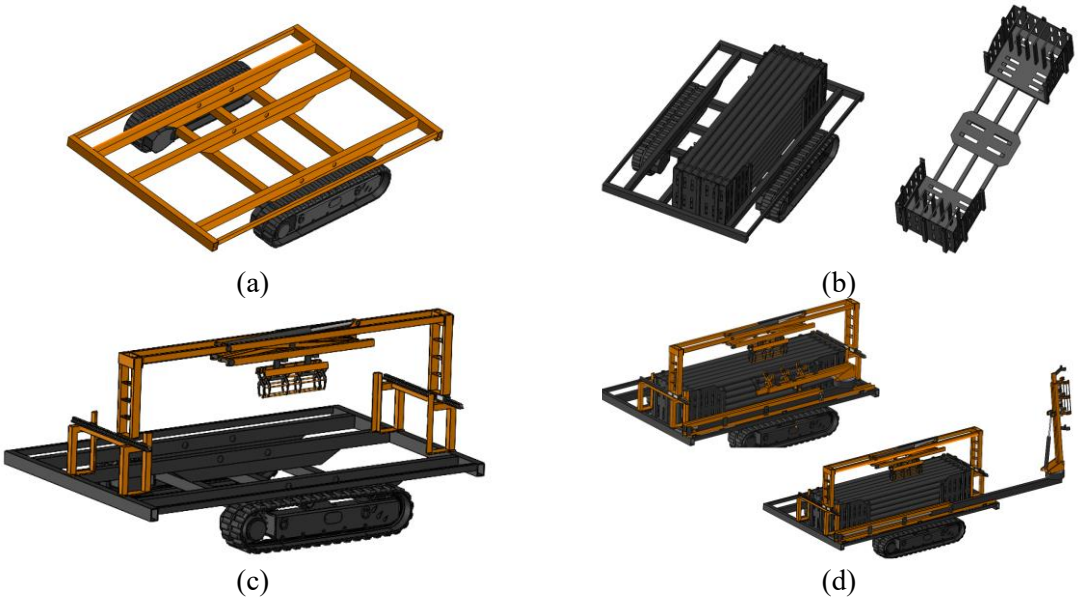

(a) (b) (c) (d)

FIGURE 2: (a) The equipment chassis; (b) Drill pipes stand; (c) The equipment drawbridge; (d) The robotic arm for pipes handling.

C. The drawbridge (Figure 2.c.) moves above the drill pipes support, lifts one pipe, and brings it to the robotic arm for positioning. The drawbridge is hydraulically driven for the movement system above the support (raise/ lower system), as well as for the gripper that handles the pipe.

D. The robotic arm (Figure 2.d.) picks up the pipe from the drawbridge gripper, then extends outside the machine, rises, and positions it in the drill head.

The entire assembly requires finite element method (FEM) numerical analysis to determine whether the structure is sufficiently stable and safe to ensure both good performance during its practical use and safety for operators.

EXPERIMENTAL

Numerical analysis using FEM

One of the most important FEM numerical analyses is that of the chassis, because, from a constructive point of view, it is at the base of the whole system.

To achieve this, it is important to determine the types of requests and the pre-processing and post-processing analytical steps. Thus, the stages are:

I. Type of analysis.
The analysis is of structural static type, and the geometry is made in the SOLIDWORKS 3D CAD modelling program. The numerical analysis using the finite element method is performed in the ANSYS WORKBENCH calculation program [5].

II. Type of material.

The material chosen for each cross member of the chassis is structural steel. The material chosen is C42, with chemical composition in weight: 0.45% C, 0.27% Si, 0.52% Mn, 0.015% P, 0.025% S, 0.05% Cr, 0.01% Mo, 0.12% Ni, 0.13% Cu and austenitizing temperature of 850 C/ 13 minutes [6].

III. Model discretization.

The Patch Conforming Method [7] module was used to perform the discretization, since errors related to the size of the elements may appear on certain crossbars. To avoid this, appropriate discretization was made on the crossbars that may encounter errors. The elements used are tetrahedral. After meshing there were obtained 102,903 nodes and 43,817 elements.

IV. Establishing the stresses to which the entire structure is subjected.

The chassis is welded to the inner faces of the tracks, and the crossbars are assembled by welded joints. This is represented in Ansys by the Connections Module.

Equations regarding loading calculus on the chassis

Each system loads different areas of the chassis structure. Thus, in the following, the values and types of loads were established.

To calculate the loading for each component of the equipment that influences the total stress obtained on the chassis there were used the formulas below (1), (2), (3), (4).

$$G = m\text{g N} \quad (1)$$

where: $g = 10\ mm/s^2$ (2)

$$S = L * l\ mm^2 \quad (3)$$

$$P = \frac{F}{S}\ MPa \quad (4)$$

Pipe stand

The pipe stand was analyzed with the presumption that the centre of mass is positioned in the centre of it.

-Stand mass: m_1=402.15 kg
-Drill pipe mass: m_2=60 kg
-Full stand (49 drill pipes): m_3=2,940 kg
-Total mass: m_{total}= 3,342.15 kg; g=10 mm/s^2
-Total weight: W=33,421.5 N

The load is divided equally on the crossbars (3 surfaces), so pressure will be applied on each crossbar (Figure 3).

P_1=11,140.5 N
The surface of each crossbar is: A_1=192,250 mm^2
The pressure applied on each crossbar on z axis is 0.6 MPa.

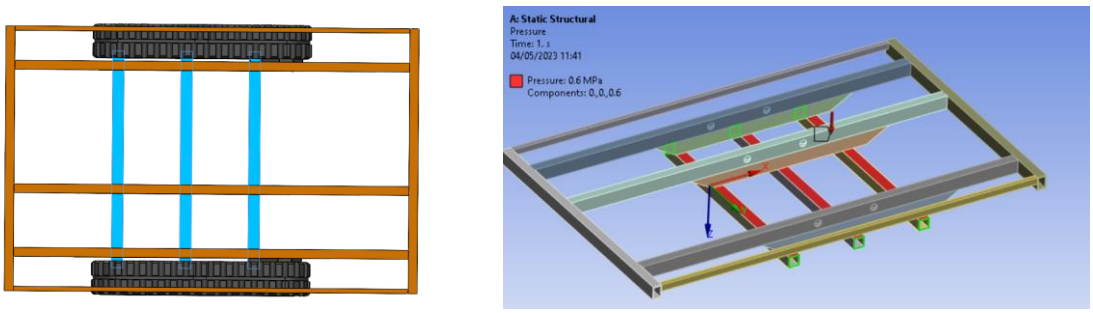

FIGURE 3 Loading on the crossbars.

Drawbridge

Since the drawbridge is a mobile system and loads act complexly depending on where there are located, the ideal case is chosen in the middle of the drill pipe stand. In this case, considering the position symmetry on the support legs and the fact that the centre of gravity of the drawbridge is in the middle of it, the loads are divided equally and symmetrically on the 4 support legs of the system. Figure 4 shows the ideal case positioning for the drawbridge and the support leg geometry.

(a) (b)

FIGURE 4 Drawbridge: (a) ideal case positioning; (b) support leg geometry.

The same calculation formulas are used as in the previous case, namely the determination of the weight of the system, the area of the required area and finally the calculation of the pressure applied to the crossbars.

-System mass: m_1=183.92 kg
-Drill pipe mass: m_2=60 kg
-Support leg mass (4): m_3=42.13 kg
-Auxiliar elements mass: m_4=50 kg
The mass is distributed equally on each support (2 on each crossbar).
-Total mass: m_{total}= 336.05 kg; g=10 mm/s^2
-Total weight: 840.13 N
Crossbar area: 2350mm * 80mm =188,000 mm^2
Pressure (on each crossbar): 0.45 MPa

Robotic arm

As well as the drawbridge, the robotic arm is a mobile system, that enables the drill pipes handling. To allow the pipe to be lifted from the pick-up position (horizontal) and to be placed in the drilling well (vertical), it is necessary for the robotic arm to move towards the chassis end. Regarding the robotic arm loading on the chassis, the arm distributes its weight sequentially across the two crossbars. The load is not distributed equally and at the same time on the two crossbars. To verify the behavior of both structures of different sizes, they were loaded with the same weight, the pressures being different due to their different sizes (Figure 5).

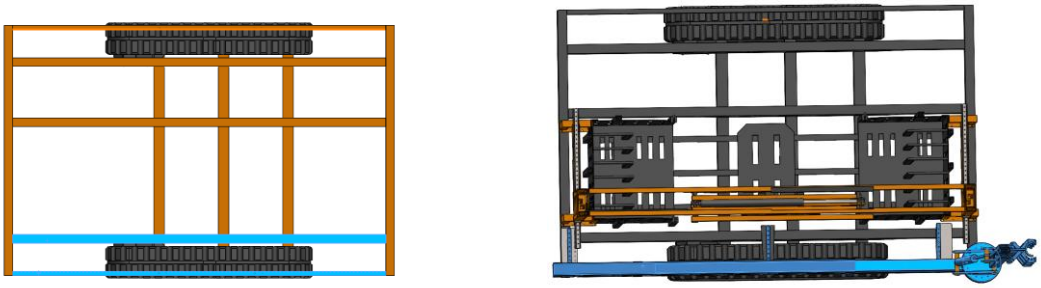

(a) (b)

FIGURE 5 Loading distribution: (a) crossbars loaded by the robotic arm weight; (b) robotic arm positioning.

Using formulas (1), (2), (3), (4), the weights of the robotic arm components are determined. For this, the mass properties module from the SOLIDWORKS program is used. Figure 23 shows the outer crossbar area.

-Total mass (robotic arm, support): m_1=293.684 kg;
-Total mass (auxiliary elements: hydraulic cylinder, bolts, plates and bearings): m_2=150 kg
-Total mass: m_{total}= 443.684 kg; g=10 mm/s^2
-Total weight: 4,436.84 N
Inner crossbar area: 3500mm * 80mm =280,000 mm^2
Pressure: 0.016 Mpa
Outer crossbar area: 3500mm * 40mm =140,000 mm^2
Pressure: 0.032 MPa

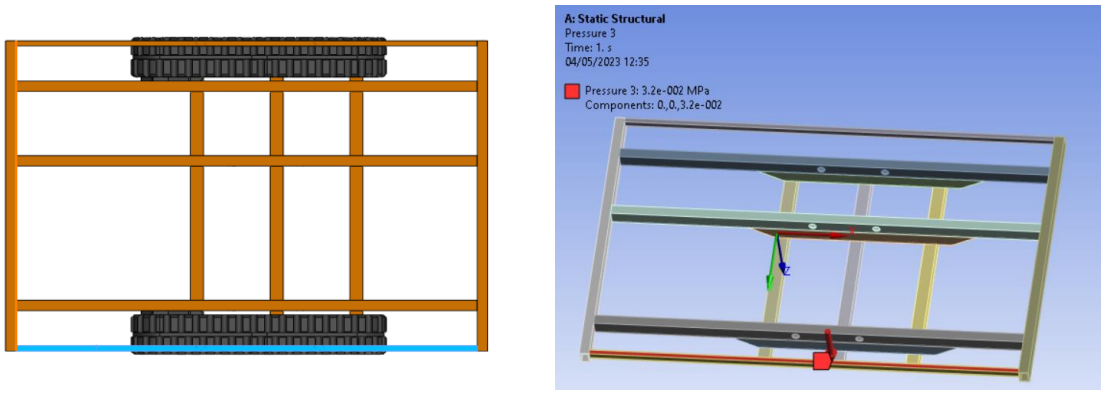

(a) (b)

FIGURE 23 Outer crossbar area of the robotic arm

Hydraulic drive unit

This group is made of components necessary for hydraulic actuation such as engine, hydraulic pump, oil and diesel tanks, etc. It is considered that for the other area of the chassis, the hydraulic pumping group is used, whose weight will be distributed equally on the remaining 3 crossbars to balance the system in terms of distributed weight (Figure 6).

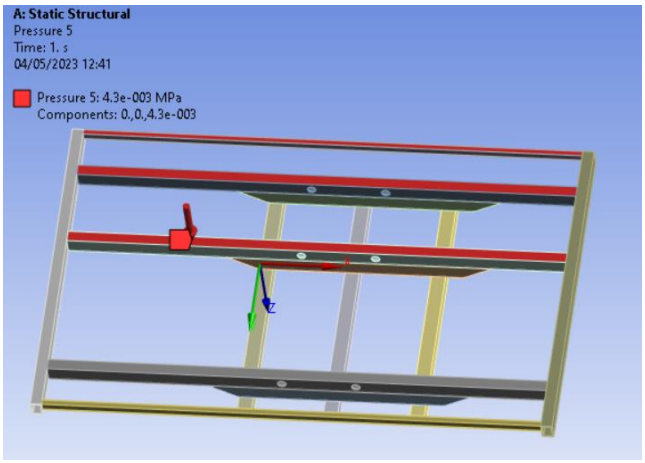

FIGURE 6 Crossbars loaded by the hydraulic drive unit.

Since the hydraulic drive unit is a stationary system, the load will be distributed equally on the 3 crossbars regardless of their size.

-Total mass: m_{total}= 600 kg; g=10 mm/s^2
-Total weight: 6,000 N
-Total area (3 crossbars): 700,000 mm^2
-Total pressure (load): 0.0086 MPa

RESULTS AND DISCUSSION

The total displacement obtained is 11.851 mm in the crossbar area where the robotic arm is in working position. This denotes that the structure loses its stability at the time of use. Figure 7 shows the total displacement analysis obtained in ANSYS.

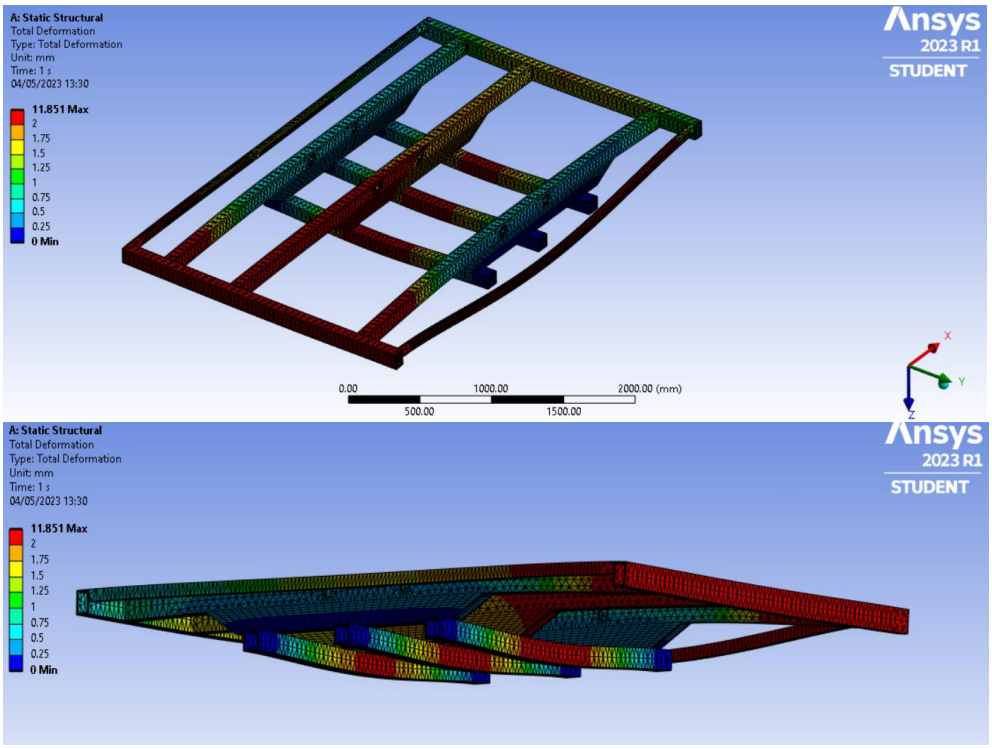

FIGURE 7 Total displacement.

The equivalent stress has a maximum value of 282 MPa in the assembly areas between base crossbars and tracks and outer crossbars and the ends of the chassis. Figure 8 shows the equivalent stress obtained for the chassis.

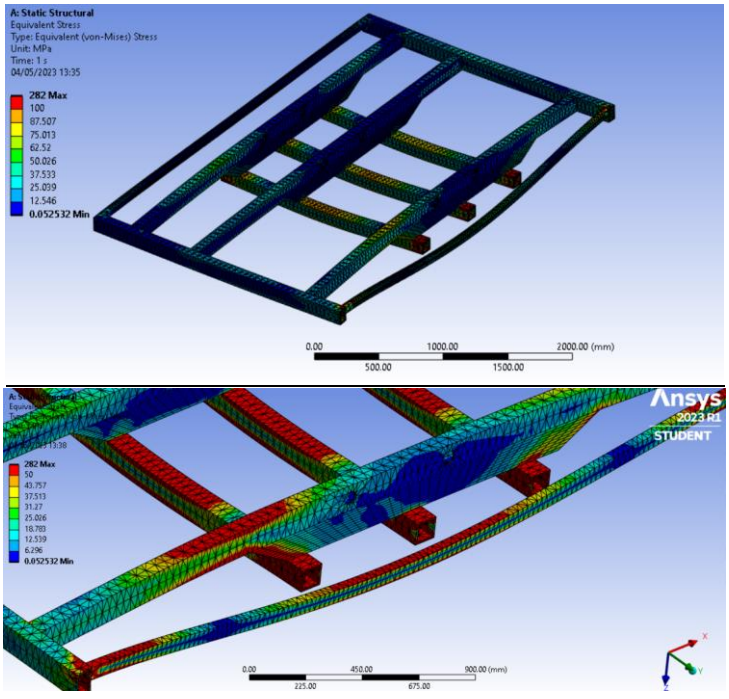

FIGURE 8 Equivalent stress.

CONCLUSIONS

From a structural point of view, the chassis can become unstable when working because its entire structure is fastened on the tracks faces. Over time this can create high stresses in the welded areas, which can cause the fastener to fail.

A solution to this problem can be the implementation of a geometry that has several fasteners and has reinforcement elements within the base crossbars.

From an analytical point of view, the displacement of 11.851 mm of the outer crossbar shows that it is undersized in relation to the load to which it is subjected. In this case it can lose stability, and high equivalent stresses appear in its contact areas with the other elements of its chassis.

A solution to solve this problem is to use a more robust crossbar and reinforce it with elements that prevent bending.

REFERENCES

[1] "Website," [Online]. Available: https://www.abtersteel.com/ro/octg-2/api-5dp-steel-drill-pipe-od-2-78-oil-drill-pipe/.

[2] [Online]. Available: https://tipfor.ro/.

[3] ***Beretta Alfredo SRL, Catalog Utilaj GT 52.

[4] "www.Fraste.com," [Online]. Available: https://www.fraste.com/en/. [Accessed 25 Aprilie 2023].

[5] C. I. SOROHAN Ștefan, "Practica modelării și analizei cu elemente finite," București, 2003, p. 324.

[6] [Online]. Available: https://www.steeldata.info/std/demo/data/5045.html.

[7] S. Ștefan, Notițe de curs PMEF, 2022.

[8] G. M. Silviu BUTNARIU, Analiza cu elemente finite în ingineria mecanică, Brașov: Editura Universității Transilvania din Brașov, 2014.

Wednesday 13 Sep. 2023	**SESSION 12A** Oral Presentations **Interfaces and Interphases**
Session 12A Co-Chairmen:	**Tatjana Glaskova-Kuzmina,** Institute for Mechanics of Materials, University of Latvia, Riga, Latvia **Diana Portan,** Department of Mechanical Engineering and Aeronautics, Laboratory of Biomechanics and Biomedical Engineering, University of Patras, Greece.

HIERARCHICAL INTERFACES AS FRACTURE PROPAGATION TRAPS IN NATURAL LAYERED COMPOSITES

Hanoch Daniel Wagner

Department of Molecular Chemistry and Materials Science, Weizmann Institute of Science, Rehovot, Israel, E-mail: daniel.wagner@weizmann.ac.il

ABSTRACT

Compared with their monolithic version, layered structures are known to be beneficial in the designing of materials, especially ceramics, for enhanced fracture toughness, mechanical strength, and overall reliability. The source of property enhancement is the ability of layered structures to deflect and often arrest propagating cracks along internal interfaces between layers. Similar crack stopping abilities are found in nature for a broad range of fibrillary layered structures. The simultaneous occurrence at several scales of different types of interfaces, designated here as hierarchical interfaces, within judiciously designed layered biological composites, is a powerful approach that constrains cracks to bifurcate and stop. This is examined here using selected biological examples, potentially serving as inspiration for alternative designs of engineering composites.

KEYWORDS: Interfaces, natural composites, layered structures, crack deflection, fracture arrest.

INTRODUCTION

The issue considered in the present communication, in a mostly observational and qualitative way, deals with sophisticated design solutions offered by specific natural architectures to the problem of stalling fracture propagation in layered composite structures. The interest in this problem, extensively examined over the last few decades, originated in the brittle nature of engineering ceramic materials under tension or bending but which otherwise offer excellent thermomechanical properties. Indeed, modern structural materials are often used in critical applications such as aircraft jet engines, where reliability is the key property and thus sudden, unstoppable fracture is unacceptable. It is only recently that physics- and materials-based research has heavily dealt with the quest for materials and/or structures possessing high simultaneous strength and toughness (Launey & Ritchie, 2009). Remarkably, such structures are often found in nature. Here, an account is given of less well-known design patterns produced by nature to generate crack bifurcation and arrest in complex layered structures.

RESULTS AND CONCLUSIONS

Recently we investigated the microstructural features of the Scorpio maurus palmatus (SP)(Greenfeld et al., 2020). High-resolution scanning and transmission electron microscopy (SEM and TEM, respectively) and atomic force microscopy (AFM) images of the cylindrical SP tibia cuticle revealed an unusual Bouligand architecture. It included varying chitin-protein fiber orientations, including in-

plane twisting of laminae around their corners rather than through their centers, and a second orthogonal rotation angle that gradually tilts the laminae out-of-plane. The resulting Bouligand laminate unit (BLU) is highly warped, such that neighboring BLUs are tightly nested and mechanically interlocked. SEM images revealed that moving radially from the external side of the cylindrical cuticle down to its hollow core, the layers become increasingly thinner (Figure 1).

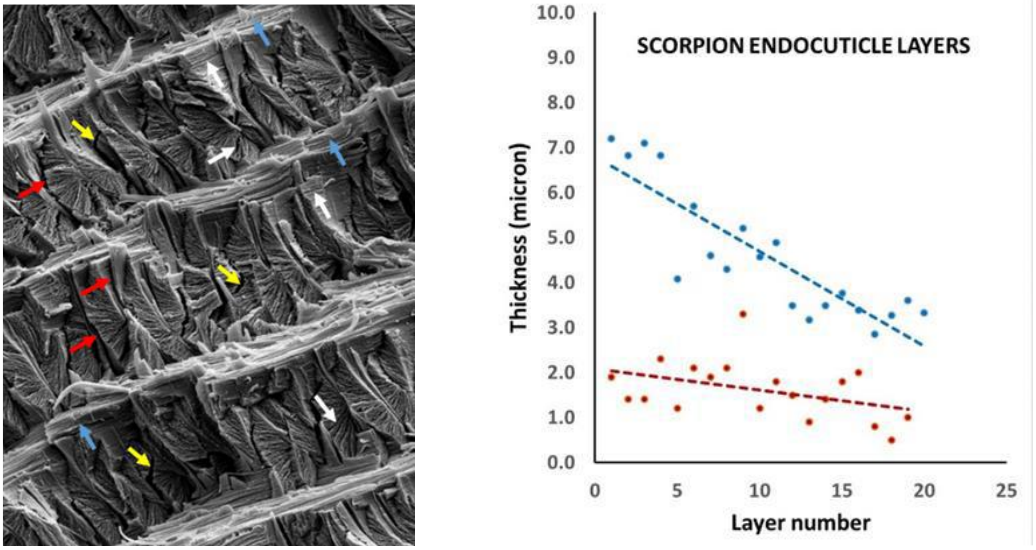

(a) (b)

FIGURE 1 (**a**) Scanning electron microscope imaging of the scorpion layered endocuticle and Bouligand laminate units (BLU) layers. White, red and blue arrows point to different interfacial failure types termed here hierarchical interface failures: White, interlamellar (nanoscale) within BLUs; Red, intralayer (microscale) between BLUs; Blue, interlayer (microscale) between layers; Yellow arrows designate non-interfacial (Griffith) internal cracks within BLUs; (b) Endocuticle layer thickness (blue symbols) against distance from the external side of the cylindrical cuticle (layer 1) down to its hollow core (layer 20). The much smaller interlayer thickness (red symbols, from 1 to 19) is plotted for comparison

By comparison, in the silica sponge spicule, the thickness of silica sponge layers diminishes with radial distance from the core, reaching a minimum value at the outer surface where, under bending, the stress is highest and tensile in nature (Monn et al., 2015). In the scorpion cuticle, however, the minimum thickness of the layers is at the core (thus the inner surface), likely because when a scorpion undergoes sharp blows or indentations from unfriendly incidents, the highest stress occurs at the core and is again tensile. Since for layered architectures the stress needed to cause cracking of an individual layer of thickness t is proportional to t-1/2, the thinnest layer should have the highest strength. Thin layers also significantly limit the depth of straight crack penetration into the structure interior. The key point is that layer thickness variations appear to be a natural consequence of increased applied stress to the scorpion cuticle and sponge spicules. In addition, strength no longer depends on size if a characteristic dimension of a structure is smaller than a certain critical length scale (Gao et al., 2003). In other words, at that point, nature needs not generate thinner layers.

REFERENCES

1. Gao, H.; Ji, B.; Jäger, I.L.; Arzt, E.; Fratzl, P. Materials become insensitive to flaws at nanoscale: Lessons from nature, *Proc. Natl. Acad. Sci*. 2003, 100(10), 5597–5600.

2. Greenfeld, I; Kellersztein, I; Wagner, H.D. Nested helicoids in biological microstructures, *Nature Communications* 2020, 11, 1-12.

3. Launey, M.E.; Ritchie, R.O. On the Fracture Toughness of Advanced Materials, *Advanced Materials* 2009, 21, 2103-2110.

4. Monnm M.A.; Weaver, J.C.; Zhanga, T.; Aizenberg, J.; Kesaria, H. New functional insights into the internal architecture of the laminated anchor spicules of Euplectella aspergillum, *Proc. Natl. Acad. Sci.* 2015, 112, 4976–4981.

NUMERICAL AND EXPERIMENTAL STUDY OF TWO DIFFERENT SANDWICH BEAMS SUBJECTED TO THREE POINTS BENDING

A.M. Tălîngă[1], G. Jiga[1], F. Baciu[1], M. Ciolcă[1*]

[1] *Department Strength of Materials, Faculty of Industrial Engineering and Robotics, University POLITEHNICA of Bucharest, ROMANIA*

***** *Corresponding author: miruna.ciolca@upb.ro*

ABSTRACT

Sandwich beams are used to strengthen a structure. Some models can also be used in aircraft due to their low weight. As they are strength elements, it is very important to know their behavior when subjected to bending. Once the materials were selected, the geometry was performed in CATIA V5 and later, imported into Ansys Workbench. Generally, a sandwich beam is characterized by a multi-layer surface structure, usually consisting of three layers. In this paper the authors analyzed numerically and experimentally the behavior of two different types of sandwich panels subjected to three points bending. For comparison, for an imposed deformation the efforts for two different models of core were determined. The core was made from PLA (Polylactic acid), an orthotropic material. In accordance with the numerical simulations in Ansys Workbench, in order to check the validity of the results, a set of five specimens with two different core configurations have been tested on an universal INSTRON testing machine according to ASTM C393.

Keywords: 3D printing; composites; sandwich materials; bending; FEA; displacement.

INTRODUCTION

The use of Ansys Workbench and CATIA V5 was chosen for this project. The CATIA V5 software was used for the design of the structure, the next stage being the import of the structure into Ansys Workbench for Finite Element Analysis (FEA).

The fibers are the element that gives the assembly the characteristics of resistance to stress. Compared to the matrix, the stress that can be taken is clearly higher, while the corresponding elongation is reduced.

Usually, a sandwich type assembly is characterized by a multilayer surface structure (Figure 1), consisting of:

• Two covering layers also called "face sheets", which form the load-bearing structure (disc, plate or membrane), layers made of a rigid and resistant material;

• An intermediate layer called "core", much thicker than the two covers, of low weight, having the role of separating the two face sheets and ensuring the transmission of efforts from one sheet to another. Usually, this core can be honeycomb (aluminum, paper, plastic), foam (polyurethane, polystyrene) or profiles (metal, plastic). [1]

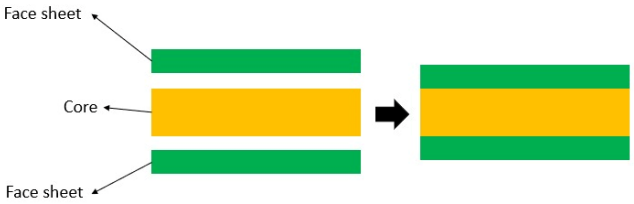

FIGURE 1 Sandwich material structure

From the specific weight point of view, the attachment of the face sheets to the core is essential for the quality of the sandwich structure. From an optimal point of view, the weight of the core should be two-thirds of the total weight of the sandwich structure, so it is important that the core be as light as possible.

The sandwich surface element is essentially different from the usual isotropic and orthotropic multilayers, through the characteristic properties of the core. The core must distance and support the load-bearing sheets and take only the loads that act perpendicular to the surface of the structure.

Over the last fifty years composite materials have developed the fastest. Due to a special versatility, the volume and number of fields that use composite materials products have grown constantly, developing new solutions that improve the quality of the products and their attractiveness for new markets. Composites are no longer the preserve of aerospace, defense, or high-value goods. They have quickly become a way to achieve high structural performance at low cost and began to be found all around us.

These composite materials are often used in areas such as: watercrafts, automobiles, vehicles for heavy transport, constructions, corrosion resistant elements, aeronautics, and military industry. For this study, there were used two different sandwich beams, with face sheets made of aluminum and core made of PLA (Polylactic acid). The aim of the paper was to analyze the bending behavior of a sandwich type beam, following the application of a speed of 1 mm/min. So, the reactions of the forces at the support points were determined, for two configurations of honeycomb cores, with a variation of the inclination angle of the walls, α, of 30^o respectively of 60^o. Figure 2 shows the angle that is modified during tests. The cores are denoted by: F1, honeycomb with an inclination angle of 30^o and F2, honeycomb with an inclination angle of 60^o.

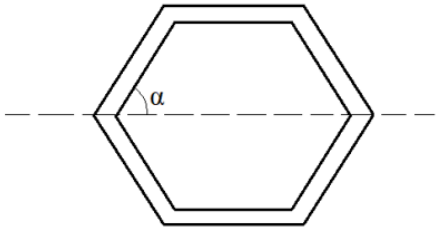

FIGURE 2 Honeycomb cell, highlighting angle α

EXPERIMENTAL STUDY OF A SANDWICH BEAM SUBJECTED TO THREE-POINT BENDING

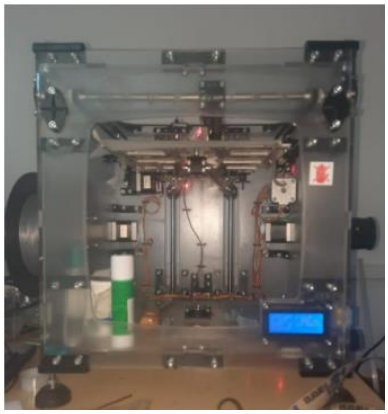

3D printing is a process of forming a three-dimensional solid object of any shape, achieved through an additive manufacturing process, where successive layers of material are deposited in different shapes. 3D printing is also distinct from traditional machining techniques, which are based on the removal of extra material through processes such as cutting, drilling, casting, etc.

FIGURE 3 shows the Vertex 3D printer that was used to print the PLA core.

Figure 4 shows the 3D printer that was used, marked with index 1. The two print heads of the printer were noted with index 2. One printhead is inactive, and the second one is assigned to the PLA material. On the right side of Figure 4, a virtual version of the 3D printer is generated so that the operator can estimate the maximum dimensions that can be used for a structure. After the structure has been sized and positioned inside the virtual printer, a preview command can be launched to make sure everything is compliant. The transfer of data from the program to the 3D printer was done using an SD card. To be able to access the geometry, the printer is equipped with a digital screen illustrated in Figure 5. The screen provides information related to the printing process. For example, the indication on the display screen 190/200° refers to the printer head temperature, while 22/0° indicates the temperature of the ambient environment. "SD" means that the structure, which is printed, is on an SD card.

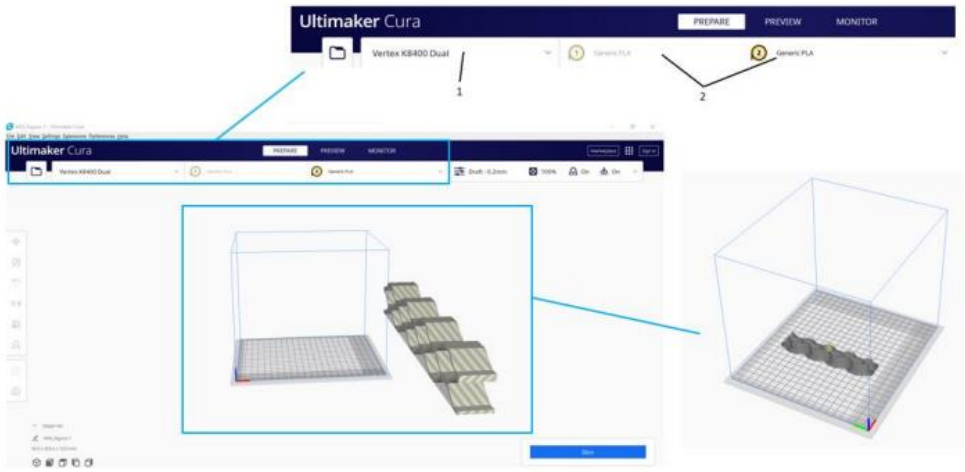

FIGURE 4 Interface of Ultimaker Cura software [5]

FIGURE 5 3D printer digital screen

It is not mandatory for the geometry to be on the card, the printer can also print directly from the computer, using a transfer cable. But using a transfer cable has a major disadvantage because there is the possibility of a time lag, which could affect the structure, leaving gaps in it. The value of 22% refers to the percentage reached by the piece during printing, and below the word "Printing.." suggests that the printing process is in progress.

This printer can use one or two print heads. If both print heads are used, the structure can have two colors, and the printing speed will increase considerably. In the case studied, only one print head was used.

Figure 6 presents on the left side the PLA filament roll and on the right side the print head, the red LED indicating that the structure is being printed.

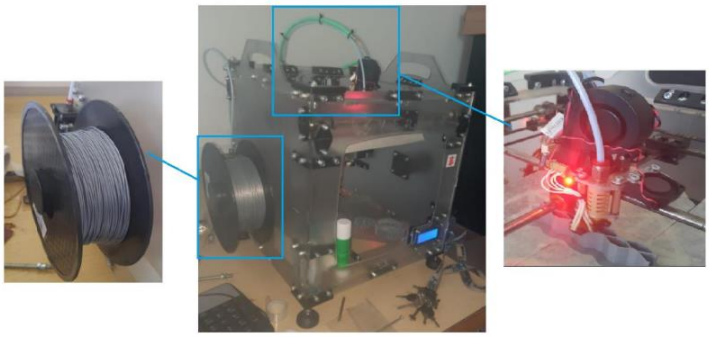

FIGURE 6 3D printer, with its components

After the specimens were printed, their dimensions were checked. Thus, it was observed that there were errors between the geometry imported into the 3D printer and that obtained physically. The surfaces were highlighted, which are to be measured according to Figure 7, where *a, b, c, d, e* represent the core geometry dimensions, *h* the total height of the structure, *pt* the thickness of the aluminum plate.

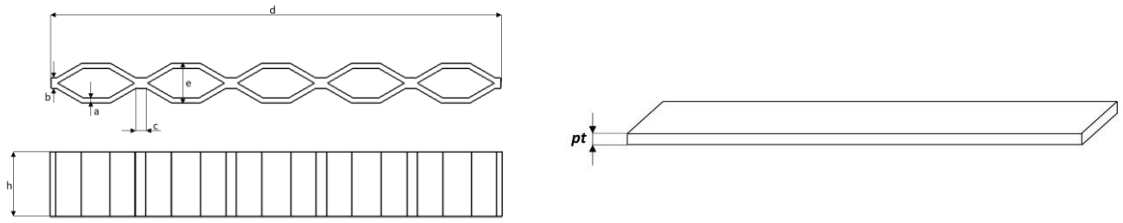

(a) (b)

FIGURE 7 Sandwich structure measured dimensions: (a) core (PLA); (b) face sheet (Aluminun plate)

To perform the tests 5 specimens were printed for each angle inclination. The dimensions of each specimen were checked, and their arithmetic average was made, as can be seen in Table 1.

TABLE 1 Measured dimensions for the 5 specimens.

Sandwich structure														
No.	**F1**							**F2**						
	a	**b**	**c**	**d**	**e**	**h**	**gp**	**a**	**b**	**c**	**d**	**e**	**h**	**gp**
1	3.43	4.24	4.4	172	16.2	28.55	0.53	2.53	4.47	3.95	172	15.81	28.14	0.55
2	2.68	4.38	4.57	172	15.71	28.31	0.6	3	4.36	4.15	172	16.07	28.21	0.6
3	2.68	4.38	4.51	172	15.56	28.59	0.51	2.89	4.45	4.07	172	15.76	27.35	0.65
4	2.45	4.39	4.53	172	15.48	28.85	0.57	2.42	4.47	3.96	172	15.4	28.34	0.58
5	2.85	4.46	4.22	172	15.97	28.32	0.65	3.1	4.42	3.89	172	15.57	28.18	0.73
Avg.	2.818	4.37	4.446	172	15.784	28.524	0.572	2.788	4.434	4.004	172	15.722	28.044	0.622

The force values corresponding to displacements of approximately 0.5 mm were selected. After carrying out the bending test, it can be observed that the F1 structure whose inclination angle is 30^o supports the highest force. The failure of the structures was predominantly caused by the peeling of the adhesive. Table 2 presents the corresponding values between forces and displacements, for F1 and F2 cores.

TABLE 2 Experimental results for the 5 specimens.

Sandwich structure				
No.	**F1**		**F2**	
	Force [N]	**Displacement [mm]**	**Force**	**Displacement [mm]**
1	813.5	0.5023	861.2	0.501
2	558.5	0.5018	840.6	0.499
3	547.8	0.5057	269	0.497
4	932.7	0.5044	315.8	0.508
5	659.7	0.4999	568.4	0.502
Average	702.44	0.5028	571	0.501

NUMERICAL ANALYSIS OF A SANDWICH BEAM SUBJECTED TO THREE-POINT BENDING

Table 3 shows the values chosen for the material characteristics, in the case of Poisson's ratio the differences are not very big, but in the case of Young's modulus, aluminum has a value approximately 33 times higher than PLA. Due to the very thin thickness of the adhesive (0.1 mm), it was modeled as a "Bonded" contact element.

TABLE 3 Materials characteristics for the sandwich structure.

No.	**Material**	**Density** $[\mathbf{kg/m^3}]$	**Young's modulus [MPa]**	**Poisson's ratio**
1	Aluminum	2770	70000	0.33
2	PLA	1400	2131	0.322

After the materials were defined, the geometry was modeled in CATIA V5 software and then imported into Ansys Workbench. The variants to be analyzed can be observed in Figure 9.

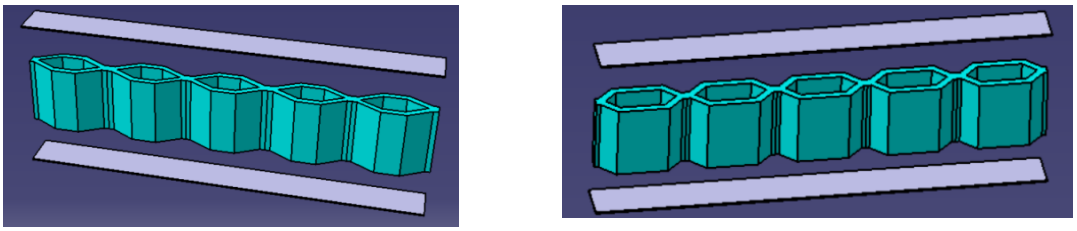

(a) F1 (b) F2

FIGURE 9 Sandwich beam geometry.

For the two sandwich structures, three surfaces were created in Space Claim to be able to apply the blockages and displacement. As can be seen in Figure 10, on the lower sheet there are two surfaces, these having a width of 2 mm, and on the upper sheet there is a single surface of 2 mm. These dimensions were chosen because it was desired to respect the dimensions of the jaws that were used in the experimental study.

For the two configurations, a controlled discretization was used, so that the elements are predominantly tetrahedral. Thus, 26,070 nodes and 6,796 elements were obtained for the F1 configuration and 46,762 nodes and 7,957 elements for the F2 configuration. Figure 11 shows that the size of the element varies according to each component. The boundary conditions for the two configurations were imposed, as can be seen in Figure 12. A force, which was previously obtained from the experimental test, was applied to the upper part, and a displacement support and a joint were applied to the lower part to reproduce the experimentally simulated locking mode. For the first block, only the rotation on Y was left free, and for the second, the movement on X and the rotation on Z were left free.

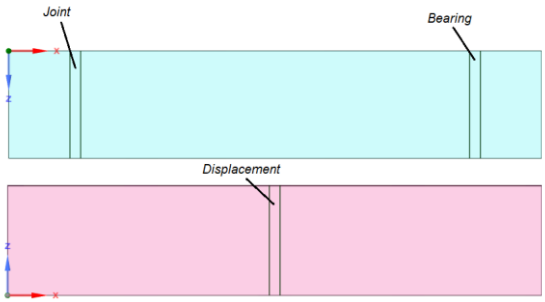

FIGURE 10 Geometry of the face sheets

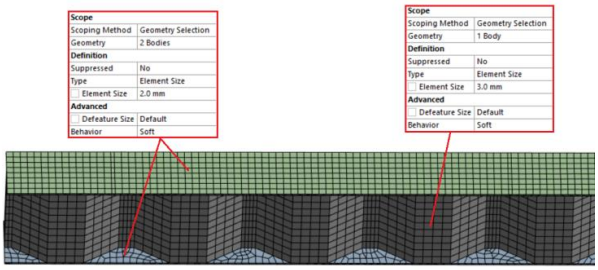

FIGURE 11 Sandwich structure discretization.

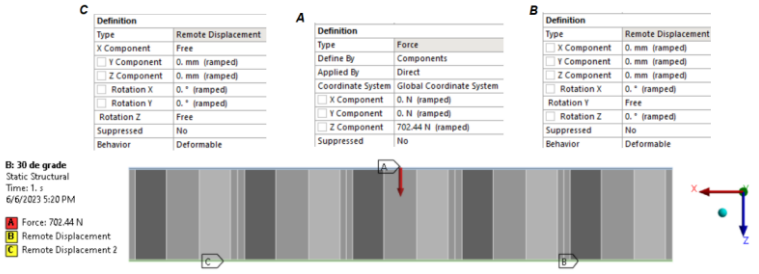

FIGURE 12 Blocking and loading used for the sandwich structure.

For the first configuration, F1, deformations of approximately 0.58 mm were obtained, found on the aluminum plate. As can be seen in Figure 13, the largest displacements are in the middle of the piece, becoming smaller towards the outside.

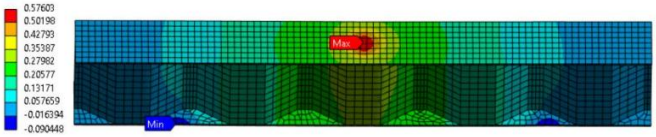

FIGURE 13 Displacements obtained along the Z-axis direction for F1 mode

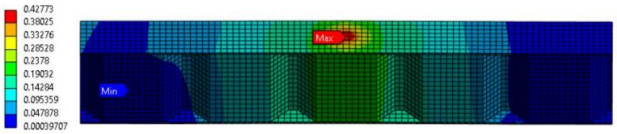

FIGURE 14 Total displacements for F2 model.

For the second configuration, F2, displacements of approximately 0.43 mm were obtained, this value being found in the center of the part, as in the case of the previous configuration, as seen in Figure 14.

From the results obtained, it was observed that aluminum plates are loaded more than the core, the PLA core taking approximately 32% of the total displacement.

RESULTS AND CONCLUSIONS

Following the numerical analysis with the finite element method, could be observed that the sandwich structure with a honeycomb core, with an angle inclination of 30°, supports the highest force, its value decreasing as the angle increases. Table 4 shows that the displacements of the assembly are identical to the displacements of the aluminum plates. This suggests that the aluminum plates take up most of the total loads.

TABLE 4 Centralization of the obtained results.

Model	Structure	Total displacements [mm]	Force [N]
F1	Assembly	0.576	702.44
	Aluminum	0.576	
	PLA	0.403	
	Experimental	0.502	702.44
F2	Assembly	0.427	571
	Aluminum	0.427	
	PLA	0.291	
	Experimental	0.501	571

After comparing the experimental results with the numerical ones, admissible errors with a value below 15% were obtained, which can validate the experimental study. Figure 15 shows the errors obtained between experimental and numerical analysis for obtained displacements in the two configurations.

A first factor that contributes to these errors is that the material used for the core is not homogeneous, showing voids, cracks, or areas of reduced density. This feature cannot be accurately simulated in ANSYS.

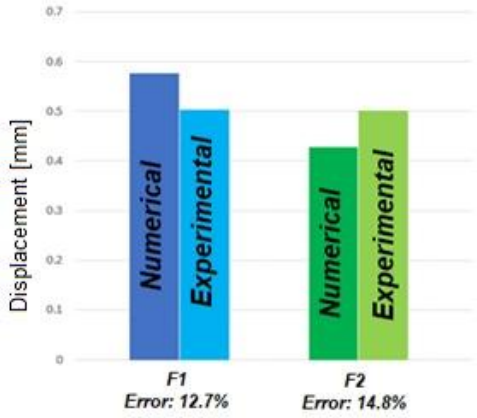

FIGURE 15 Comparison of results obtained with experimental and numerical analysis, for F1 and F2 models

Another reason for errors results from the printing process. Although a specific geometry is entered into the 3D printer, further checks on the parts revealed different dimensions. Therefore, the specimens were re-measured, and an arithmetic average was calculated for different areas. These new values were used to adjust the initial geometry to reproduce reality as closely as possible.

The appearance of impurities and the method of preparation of the adhesive can represent another factor responsible for the appearance of errors. To obtain the correct mechanical properties of the adhesive, an equal amount of base and hardener is required, and the mixture between the two components must be perfectly homogeneous, without the appearance of air bubbles.

REFERENCES

1. Liu, W.K.; Li, S.; Park, H.S. Eighty Years of the Finite Element Method: Birth, Evolution, and Future, *Archives of Computational Methods in Engineering* 2022, 29, 4431–4453.

2. Mallick, P.K. Fiber-Reinforced Composites, Materials, Manufacturing, and Design, Third Edition, CRC Press, 2007.

3. Shahrubudin, N.; Lee, T.C.; Ramlan, R. An Overview on 3D Printing Technology: Technological, Materials, and Applications, *Procedia Manufacturing* 2019, 35, 1286-1296.

4. https://ultimaker.com/learn

Monday 11 Sep. 2023	**Rapid-Fire Poster Session** **(HALL A)**
Session RFPS Co-Chairmen:	**Gabriel Jiga,** University POLITEHNICA of Bucharest, Romania **Stephanos Zaoutsos,** University of Thessaly, Greece

LAVENDER ESSENTIAL OIL ENRICHED HYDROXYAPATITE IN CHITOSAN MATRIX FOR BIOMEDICAL APPLICATIONS

Y. Benali[1], D. Predoi[2,*], C.S. Ciobanu[2], S.L. Iconaru[2], G. Jiga[3,*], R. Trusca[4], L. Ghegoiu[2], A.A. Ancuta[3], A.M. Talanga[3], M. Costea[3], T.F. Stefanescu[5], K. Boughzala[1], M.L. Badea[6]

[1]Higher Institute of Technological Studies of Ksar Hellal, 5070 Ksar-Hellal, Tunisia

[2]National Institute of Materials Physics, Atomistilor Street, No. 405A, P.O. Box MG 07, 077125 Magurele, Romania
[3]Department of Strength of Materials, University Politehnica of Bucharest, Faculty of Engineering and Management of Technological Systems, 313 Splaiul Independentei, Bucharest, Romania
[4]National Centre for Micro and Nanomaterials, University Politehnica of Bucharest, 060042 Bucharest, Romania
[5]C.A. Rosetti Highschool, Giuseppe Garibaldi Street No. 11, 014192Bucharest, Romania
[6]Faculty of Horticulture, University of Agronomic Sciences and Veterinary Medicine, 59 Marasti Blvd., 011464 Bucharest, Romania
** Correspondence to: Daniela Predoi (dpredoi@gmail.com); Gabriel Jiga (gabijiga@yahoo.com).*

ABSTRACT

Due to the increase of microbial strains resistance, development of new biomaterials with enhanced antimicrobial properties are of great interest. Herein, we report the synthesis and the characterization of lavender essential oil enriched hydroxyapatite in chitosan matrix (HACh-L). The structural changes induced by the presence of lavender essential oil and chitosan was evaluated by X-ray diffraction (XRD). Morphology and chemical composition were investigated by scanning electron microscopy (SEM) and energy dispersive spectroscopy (EDS). Fourier transform infrared (FTIR) spectroscopy studies reveal the presence of characteristic vibrational bands in the HACh-L samples. The antimicrobial activity of HACh-L was evaluated against *Staphylococcus aureus, Escherichia coli* and *Candida albicans* reference microbial strains. The findings of the antimicrobial assays prove that HACh-L possess good antimicrobial activity against all the tested microbial strains for all tested time intervals. The *in vitro* cytotoxicity assays determined that the exposure of the primary human osteoblast cells (hFOB 1.19) to HApCh-L did not reduce the cell viability. The results suggested that this new type of biomaterial (HACh-L) could be an appropriate candidate for the development of future novel antimicrobial agents with applicability in biomedical engineering.

INTRODUCTION

According to the WHO, antimicrobial resistance occurs because bacteria, viruses, fungi and parasites change and therefore no longer respond to regular drugs, making infections harder to treat [1]. This behaviour can lead to severe illness and even death. Thus, the development of new drugs and/or materials with good antimicrobial properties is of interest for the pharmaceutical and medical fields [2-3]. Hydroxyapatite (HA) is used in various biomedical applications including dentistry or orthopedy. But it is well known that HA has no antimicrobial activity. Even though, HAp is the object of study for many promising applications, numerous parameters such as shape, size, dopant or coating elements as well as surface properties could influence its properties and could enhance its

performance in different applications. Nowadays there are tremendous ongoing studies that continues to explore new ways to expand the properties of hydroxyapatite for various biomedical purposes [4-8]. Chitosan is a natural polysaccharide which is derived from the chitin found in the exoskeletons of crustaceans. During the years, chitosan has been studies for its various ubiquitously biological activities, including its antimicrobial properties which are often attributed to its unique chemical structure and cationic nature [9]. Chitosan has been studied due to its properties for numerous applications such as food preservation, wound healing, and as a coating for different medical devices [9]. The excellent antimicrobial activity of chitosan against *Streptococcus, Staphylococcus* and *Pseudomonas* species was previously proved by Jayakumar et al [10]. On the other hand, lavender oils are popularly known due to their pleasant aroma and they are used for since many years in aromatherapy, and also in the fabrication of perfumes, and various skincare products. Due to its chemical constituent, the lavender essential oils are believed to possess good biological properties and also a strong antimicrobial and antifungal activity [11-12]. In the study conducted by Roller et al. [13] it was highlighted that lavender oils possess great potential to be used in controlling the spread of MRSA in the hospitals. Other reported studies have also demonstrated that the antibacterial activity of the lavender essential oils are more pronounced against Gram positive bacteria, such as *Staphylococcus aureus, Bacillus cereus*, and *Listeria innocua*, compared to the Gram negative bacteria, like *Escherichia coli, Clostridium perfringens*, *Pseudomonas aeruginosa* and *Salmonella Typhi* [14-15]. Here, we report the fabrication of lavender essential oil enriched hydroxyapatite in chitosan matrix (HACh-L) using an adapted method. The characterisation of the HACh-L sample was made using techniques such as: XRD, SEM, EDS and FTIR spectroscopy. The antimicrobial activity of HACh-L samples was evaluated against *S. aureus, E. coli* and *C. albicans* reference microbial strains. Our results indicate that the new material based on lavender essential oil enriched hydroxyapatite in chitosan matrix may be an appropriate candidate for the development of new antimicrobial agents with applicability in biomedical engineering.

EXPERIMENTAL

HACh-L sample were obtained using an adapted method. $(NH_4)_2HPO_4$, $Ca(NO_3)_2*4H_2O$ and chitosan were used as precursors. The lavender essential oil (*Lavandula angustifolia Sevastopolis*) used in this study was obtained by steam distillation [16] and the fabrication of HACh-L was made in agreement with the steps previously reported [16]. The XRD studies of HACh-L were done using a Bruker D8 Advance diffractometer [16]. HACh-L morphology and composition was analysed by SEM, with the aid of a Quanta Inspect F microscope. FTIR spectra were obtained using a Perkin Elmer SP 100 spectrometer operated in attenuated total reflection (ATR) mode. The second derivative spectra of HACh-L sample was obtained following the experimental procedure described in detail in our previous works [16, 17]. The antimicrobial properties of HACh-L samples were assessed *in vitro* using *Staphylococcus aureus* ATCC 25923, *Escherichia coli* ATCC 25922 and *Candida albicans* ATCC 10231 (ATCC, Old Town Manassas, VA, USA) reference microbial strains. The *in vitro* experiments were performed in accordance with the method previously described in [16]. For this purpose, the samples were incubated for three different time intervals with microbial suspensions and their antimicrobial activity was determined. The experiments were performed in triplicate and the data was presented as mean ± SD.

The cytotoxicity of the HACh-L nanocomposites was also evaluated using a primary osteoblast culture (hFOB 1.19) prepared according to Gallagher et al. [18]. The *in vitro* cell viability experiments were conducted using the methodology previously described in [19].

RESULTS AND DISCUSSION

The structure of the HACh-L nanocomposites was investigated by X-Ray Diffraction. The XRD patterns of HACh-L powders as well as the pattern for pure hydroxyapatite with the reference hexagonal structure ICDD-PDF# 9-432 are presented in Figure 1. The diffraction peaks of HACh-L samples, correspond to the vertical lines that represent the positions of diffraction lines of pure HA with the reference hexagonal structure ICDD-PDF # 9-432, therefore indicating the obtaining of a single phase of HA. Moreover, the results also suggested that the presence of chitosan led to a slight shift of the peaks to larger angles.

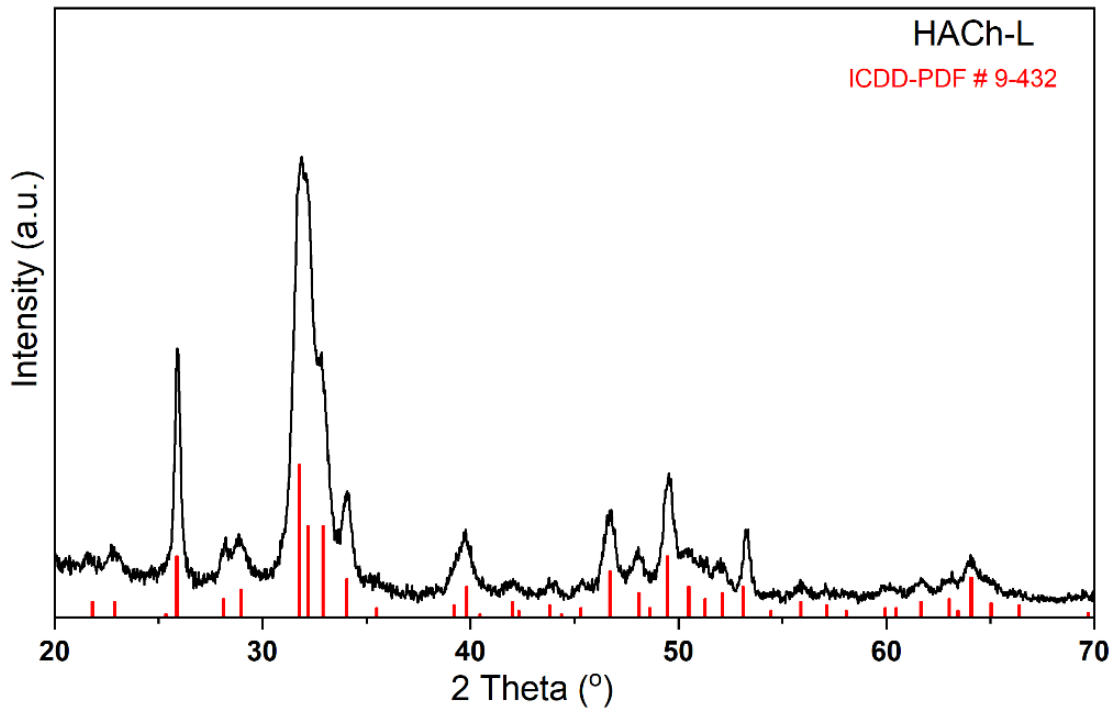

FIGURE 1 X-ray patterns of HACh-L powders (black), and pattern for the reference hexagonal structure JCPDF 9-432 (red lines).

The morphology of HACh-L powders was studied using SEM (Figure 2a). The recorded SEM images suggest that the HACh-L samples were obtained at nanometric scale and exhibit an acicular morphology. In the EDS spectra (Figure 2b) could be noticed only the presence of C, O, P, Ca, and N lines (the main constituents of the lavender essential oil enriched hydroxyapatite in chitosan matrix sample).

The results of the FTIR studies conducted on HACh-L sample are revealed in Figure 3 a,b. The spectra it is mainly dominated by the phosphate vibration bands that are characteristic to HA structure at around 475 cm^{-1} (ν_2), 562, 601, 631 cm^{-1} (ν_4), 960 cm^{-1} (ν_1), 1029, 1090 cm^{-1} (ν_3) [16]. The vibration bands found at around 875 and 1450 cm^{-1} belongs to the vibrations of the carbonate group. The weak vibration bands observed at around 690, 915, 1370 cm^{-1} belongs to C–H vibrations from the lavender essential oil [16].

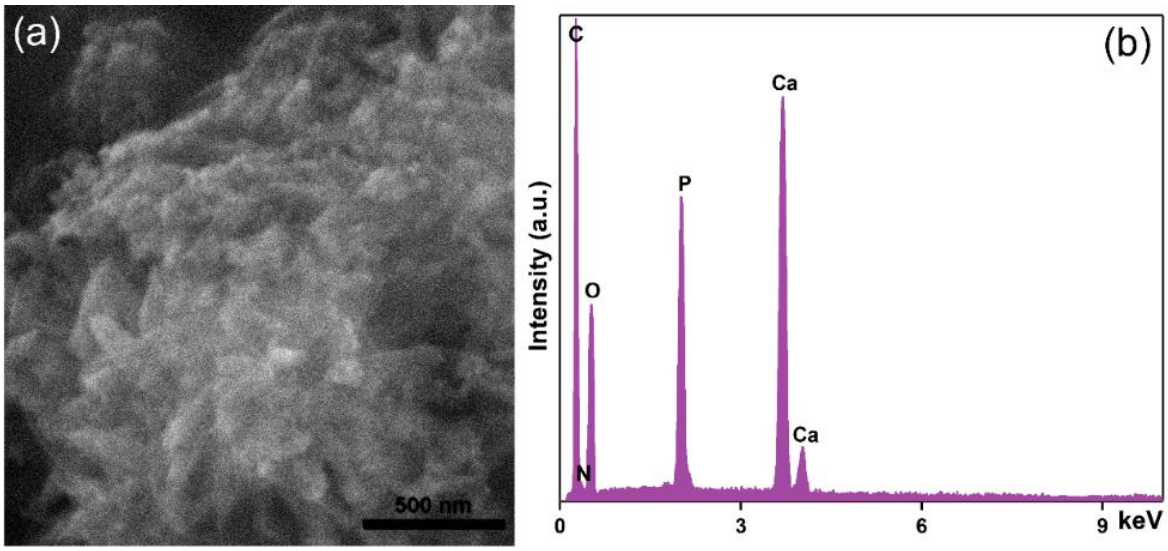

FIGURE 2 SEM images (**a**) and EDS spectra (b) of HACh-L sample.

The vibration band found at about 1640 cm^{-1} could be attributed to the C=C stretching vibrations from the lavender essential oil [16]. The maxima found at around 1733 cm^{-1} that belongs to the C=O stretching vibration indicate the presence of the lavender essential oil in the HACh-L sample [16]. The presence of the chitosan in the HACh-L sample it is indicated by the presence of the weak and broad maxima at 1540 cm^{-1} that is specific to NH_2 groups vibration in chitosan [16]. The maxima specific to $–NH_2$ group from the chitosan that could be found at 1465 cm^{-1} it is overlapped with the maxima specific to the carbonate group from the HA [16]. Other vibration bands that are characteristic to the lavender essential oil or to the chitosan are overlapped with the bands specific of the HA.

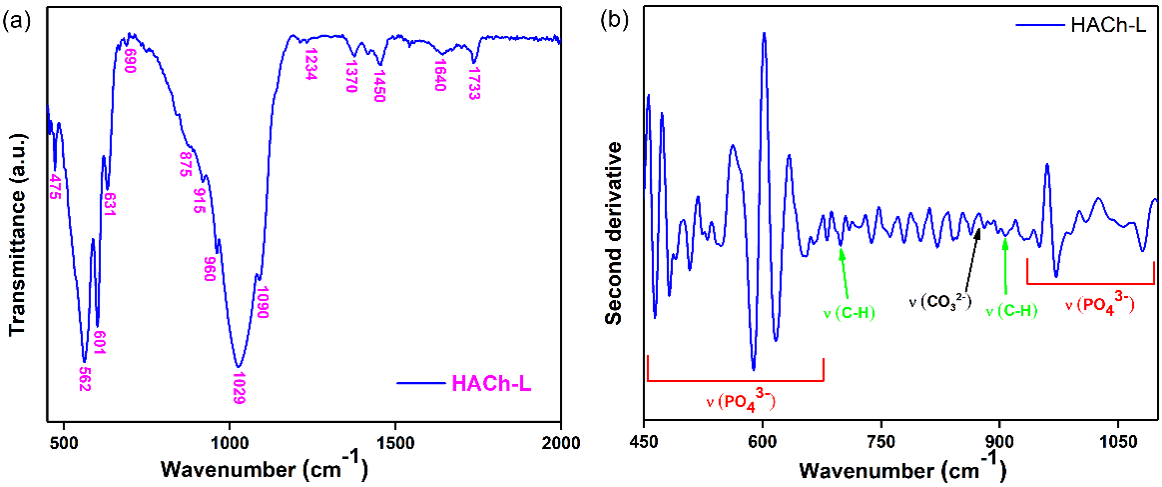

FIGURE 3 FTIR spectra (a) and FTIR-second derivative spectra obtained for HACh-L sample.

In FIGURE 3b it is depicted the second derivative spectra obtained for HACh-L sample in the 450-1100 cm^{-1} spectral domain. In this range could be easily observed the presence of the intense vibrational bands that are attributed to the fundamental vibration (ν_1, ν_2, ν_3, ν_4) of phosphate groups from HA [16, 17]. Moreover, in the FIGURE 3b could be observed the presence of the vibrational

band that is characteristic to ν(C–H) vibration from the lavender essential oil [16]. Another vibrational band that appears in the second derivative spectra of HACh-L sample could be attributed to the ν(CO_3^2) vibration [16]. According to the studies reported by Shahzad, S. et al. [20], the shoulder observed at about 895 cm^{-1} it is specific to the saccharide ring stretching from chitosan. Furthermore, in the second derivative spectra of HACh-L sample, intense vibration bands that can be attributed to impurities cannot be observed. Therefore, we could conclude that these results are in good agreement with the results of Fourier transform infrared (FTIR) spectroscopy studies.
The antimicrobial activity of the HACh-L sample was determined against *Staphylococcus aureus* ATCC 25923, *Escherichia coli* ATCC 25922 and *Candida albicans* ATCC 10231 reference microbial strains for three different time intervals (24, 48 and 72 h). The results of the antimicrobial assays highlighted that the sample exhibited great antimicrobial activity. This behaviour could be attributed to the fact that the presence of chitosan and lavender essential oil conferred the hydroxyapatite both bactericidal and fungicidal effects (Figure 4).

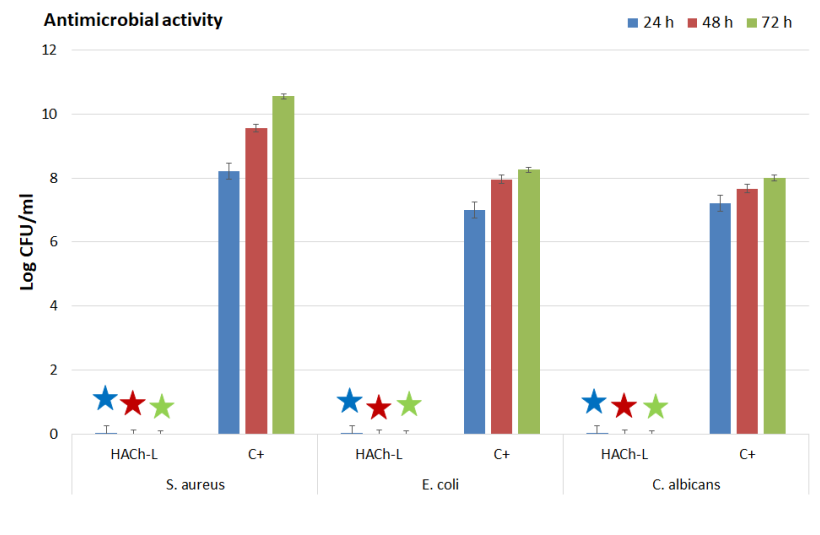

FIGURE 4 Graphical representation of the antimicrobial activity of HACh-L against *Staphylococcus aureus* ATCC 25923, *Escherichia coli* ATCC 25922 and *Candida albicans* ATCC 10231 *microbial strains*.

Furthermore, the data obtained from the antimicrobial assays suggested that the HACh-L samples exhibited bactericidal and fungicidal properties after 48 h of incubation. Nonetheless, the findings also showed that the sample possess extraordinary antimicrobial activity since the early stages of bacterial and fungal cell development. The results evidenced that the HACh-L samples completely eradicate the microbial strains for all the time-tested interval. The results presented in this paper are in good agreement with previously reported data on the antimicrobial properties of composites materials based on hydroxyapatite, chitosan and essential oils [16, 21-23]. Even though antimicrobial materials have been extensively studied, the exact mechanism responsible for their antimicrobial properties are not yet fully understood. Moreover, the antimicrobial properties of materials are attributed to the properties of their chemical constituents as well as the synergies that appear between them.

Furthermore, the cytotoxicity assay demonstrated that the HApCh-L nanocomposites exhibited a good biocompatibility in the presence of primary human osteoblast cells (hFOB 1.19). The results of

the MTT assay regarding the cell viability of the hFOB 1.19 cells exposed to HApCh-L nanocomposites for 24, 48 and 72 h were represented graphically and are depicted in Figure 5.

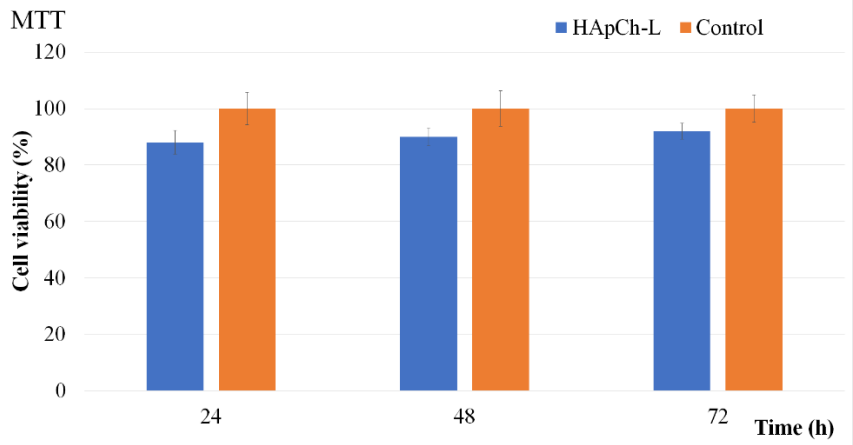

FIGURE 5 Graphical representation of the cell viability of primary human osteoblast cells (hFOB 1.19) incubated with HApCh-L for 24, 48 and 72 h. The results are depicted as mean ± SD and $p \leq 0.05$ was accepted as statistically significant.

The results of the MTT assay presented in Figure 5 emphasized that the cell viability of the hFOB 1.19 cells exhibited a value above 88% after being exposed to the HApCh-L nanocomposites in the first 24 h. More than that, the findings also demonstrated that after 48 h and 72 h of exposure, the cell viability of the hFOB 1.19 cells elevated, going up to 90% and 92%, respectively. These results are in good agreement with other studies on the topic of the biological properties of hydroxyapatite enriched with essential oils [16]. In their study, Prashar et al reported that the *in vitro* testing of lavender oil exhibited a cell viability of 80–100% for an oil concentration of 0.125% (v/v) against three cell types 153BR, HNDF and HMEC-1 and that the increase in the oil concentration affected greatly the cell's viability. Even though the lavender essential oils are wide spread in industries such as cosmetic, perfumery, aromatherapy, to this day there are only few reports regarding its cytotoxicity in general and there is a need of more elaborate studies in order to better comprehend the complexity of their biological properties [25]. Meanwhile, the preliminary findings of our study highlighted that the novel lavender essential oil enriched hydroxyapatite in chitosan matrix nanocomposites exhibit good biological properties having both a good biocompatibility and possessing strong antimicrobial activity which make them suitable candidates for being considered for further biomedical applications.

CONCLUSIONS

In this work we report the obtaining of a new biomaterial based on lavender essential oil enriched hydroxyapatite in chitosan matrix (HACh-L) by an adapted method. The features of the HACh-L samples were studied by XRD, FTIR, SEM and EDX measurements. The results of the SEM studies highlight the acicular morphology of the HACh-L sample. The presence of the chitosan, lavender essential oil and HA in the studied samples was proved by the results of the EDX, XRD and FTIR studies. Our preliminary *in vitro* biological assay regarding the cytotoxicity properties as well as the antimicrobial activity evidenced that lavender essential oil enriched hydroxyapatite in chitosan matrix composites are promising materials for the future development of novel composite materials

possessing enhanced biological properties that could promote the osteogenic process of bone healing and also exhibit antimicrobial properties.

ACKNOWLEDGEMENTS
This work was funded by the Core Program of the National Institute of Materials Physics, PC1-PN23080101 and by the Project 35PFE/2022 Project granted by the Romanian Ministry of Research, Innovation and Digitalization.

REFERENCES
1.https://www.who.int

2. Timková, I.; Maliničová, L.; Nosáľová, L.; Kolesárová, M.; Lorková, Z.; Petrová, N.; Pristaš, P.; Kisková, J. Genomic insights into the adaptation of Acinetobacter johnsonii RB2-047 to the heavy metal-contaminated subsurface mine environment, *Biometals* 2023. 10.1007/s10534-023-00555-0.

3.El-Gendy, M.M.A.A.; Abdel-Moniem, S.M.; Ammar, N.S.; El-Bondkly, A.M.A. Bioremoval of heavy metals from aqueous solution using dead biomass of indigenous fungi derived from fertilizer industry effluents: isotherm models evaluation and batch optimization, *Biometals* 2023, 36, 1307–1329, 10.1007/s10534-023-00520-x.

4. Fiume, E.; Magnaterra, G.; Rahdar, A.; Verné, E.; Baino, F. Hydroxyapatite for Biomedical Applications: A Short Overview, *Ceramics* 2021, 4, 542-563, https://doi.org/10.3390/ceramics4040039.

5. Predoi, D.; Ciobanu, S.C.; Iconaru, S.L.; Predoi, M.V. Influence of the Biological Medium on the Properties of Magnesium Doped Hydroxyapatite Composite Coatings, *Coatings* 2023, *13*, 409.

6. Munir, M.U.; Salman, S.; Ihsan, A.; Elsaman, T. Synthesis, Characterization, Functionalization and Bio-Applications of Hydroxyapatite Nanomaterials: An Overview, *Int J Nanomedicine* 2022, 17, 1903-1925.

7. Predoi, D.; Iconaru, S.-L.; Predoi, M.-V.; Buton, N. Development of Novel Tetracycline and Ciprofloxacin Loaded Silver Doped Hydroxyapatite Suspensions for Biomedical Applications, *Antibiotics* 2023, *12*, 74.

8. Predoi, D.; Iconaru, S.L.; Predoi, M.V. Dextran-Coated Zinc-Doped Hydroxyapatite for Biomedical Applications, *Polymers* 2019, *11*, 886.

9. Ke, C.-L.; Deng, F.-S.; Chuang, C.-Y.; Lin, C.-H. Antimicrobial Actions and Applications of Chitosan, *Polymers* 2021, *13*, 904.

10. Jayakumar, R.; Prabhakaran, M.; Sudheesh Kumar, P.T.; Nair, S.V.; Tamura, H. Biomaterials based on chitin and chitosan in wound dressing applications, *Biotechnol. Adv.* 2011, 29, 322-337.

11. Lesage-Meessen, L.; Bou, M.; Sigoillot, J.C. ; Faulds, C.B.; Lomascolo, A. Essential oils and distilled straws of lavender and lavandin: a review of current use and potential application in white biotechnology, *Appl Microbiol. Biotechnol.* 2015, 99, 3375–3385.

12. Wells, R.; Truong, F.; Adal, A.M.; Sarker, L.S.; Mahmoud, S.S. Lavandula Essential Oils: A Current Review of Applications in Medicinal, Food, and Cosmetic Industries of Lavender, *Nat. Prod. Commun*. 2018, 13(10).

13. Roller, S.; Ernest, N.; Buckle, J. The antimicrobial activity of high-necrodane and other lavender oils on methicillin-sensitive and -resistant Staphylococcus aureus (MSSA and MRSA), *Altern. Complement Med.* 2009, 15, 275-279.

14. Nikolić, M.; Jovanović, K.K.; Marković, T.; Marković, D.; Gligorijević, N.; Radulović, S.; Soković M. Chemical composition, antimicrobial, and cytotoxic properties of five Lamiaceae essential oils, *Ind. Crops Prod.* 2014, 61, 225–232.

15. De Rapper, S.; Kamatou, G.; Viljoen, A.; van Vuuren S. The In Vitro Antimicrobial Activity of Lavandula angustifolia Essential Oil in Combination with Other Aroma-Therapeutic Oils, eCAM, ISSN/ISBN: 1741-427X, 2013, 1-10.

16. Predoi, D.; Groza, A.; Iconaru, S.L.; Predoi, G.; Barbuceanu, F.; Guegan, R.; Motelica-Heino, M.S.; Cimpeanu, C. Properties of Basil and Lavender Essential Oils Adsorbed on the Surface of Hydroxyapatite, *Materials* 2018, *11*, 652.

17. Predoi, S.A.; Ciobanu, S.C.; Chifiriuc, C.M.; Iconaru, S.L.; Predoi, D.; Negrila, C.C., Marinas, I.C.; Raaen, S.; Rokosz, K.; Motelica-Heino, M. Sodium bicarbonate-hydroxyapatite used for removal of lead ions from aqueous solution, *Ceram. Int.* 2024, 50(1), 1742-1755.

18. Gallagher, A.J.; Gundle, R.; Beresford, N.J. Isolation and culture of bone forming cells (osteoblasts) fromhuman bone, Human Cell Culture Protocols, *Hum. Cell Cult. Protoc*. 1996, 2, 233–263.

19. Predoi, D.; Iconaru, S.L.; Predoi, M.V. Bioceramic Layers with Antifungal Properties, *Coatings* 2018, 8, 276.

20. Shahzad, S.; Shahzadi, L.; Mahmood, N.; Siddiqi, S.A.; Rauf, A.; Manzoor, F.; Chaudhry, A.A.; ur Rehman, I.; Yar, M. A new synthetic methodology for the preparation of biocompatible and organo-soluble barbituric- and thiobarbituric acid based chitosan derivatives for biomedical applications, *Mater. Sci. Eng. C* 2016, 66, 156-163.

21. Cavanagh, H.M.A.; Wilkinson, J.M. Biological activities of lavender essential oil, *Phytother. Res.* 2002, 16, 301–308.

22. Zhang, H.; Liang, Y.; Li, X.; Kang, H. Effect of chitosan-gelatin coating containing nano-encapsulated tarragon essential oil on the preservation of pork slices, *Meat Sci.* 2020, 166, 108137

23. Yan, D.; Li, Y.; Liu, Y.; Li, N.; Zhang, X.; Yan, C. Antimicrobial Properties of Chitosan and Chitosan Derivatives in the Treatment of Enteric Infections. *Molecules* 2021, 26, 7136.

24. Prashar, A.; Locke, I.C.; Evans, C.S. Cytotoxicity of lavender oil and its major components to human skin cells, *Cell Prolif.* 2004, 37, 221–229.

25. Tisserand, R.; Balacs, T. Essential Oil Safety: A Guide for Health Care Professionals. 2000, London: Churchill.

NEW COMPOSITES BASED ON HYDROXYAPATITE AND MONTMORILLONITE FOR LEAD WATER DECONTAMINATION APPLICATIONS

Y. Benali[1], D. Predoi[2,*], S.L. Iconaru[2,*], C.S. Ciobanu[2], L. Ghegoiu[2], G. Jiga[3,*], M. Motelica-Heino[4], C.C. Negrila[2], M.L. Badea[5], A.A. Ancuta[3], A.M. Talanga[3], M. Costea[3], K. Boughzala[1], R. Trusca[6], T.F. Stefanescu[7]

[1]Higher Institute of Technological Studies of Ksar Hellal, 5070 Ksar-Hellal, Tunisia
[2]National Institute of Materials Physics, Atomistilor Street, No. 405A, P.O. Box MG 07, 077125 Magurele, Romania
[3]Department of Strength of Materials, University Politehnica of Bucharest, Faculty of Engineering and Management of Technological Systems, 313 Splaiul Independentei, Bucharest, Romania
[4]Institut des Sciences de la Terre D'Orleans (ISTO), UMR, 327, Centre National de la Recherche Scientifique CNRS Université d'Orléans, 1A rue de la Férollerie, CEDEX 2, 45071 Orléans, France
[5]Faculty of Horticulture, University of Agronomic Sciences and Veterinary Medicine, 59 Marasti Blvd., 011464 Bucharest, Romania
[6] National Centre for Micro and Nanomaterials, University Politehnica of Bucharest, 060042 Bucharest, Romania
[7]C.A. Rosetti Highschool, Giuseppe Garibaldi Street No. 11, 014192Bucharest, Romania
** Correspondence to: Daniela Predoi (dpredoi@gmail.com); Simona Liliana Iconaru (simonaiconaru@gmail.com); Gabriel Jiga (gabijiga@yahoo.com).*

ABSTRACT

Nowadays, the water contamination with various ions represents a serious problem worldwide, having a major impact on people's health. Tremendous efforts were made in order to develop new materials that could be successfully used for water decontamination processes as adsorbents. Herein, is reported the development of a new composite material based on hydroxyapatite and montmorillonite (HAp_MMT). The scanning electron microscopy (SEM) images of HAp_MMT reveal their acicular morphology. Additional information regarding the surface morphology of the HAp_MMT pellets were obtained through atomic force microscopy (AFM) studies. No additional maxima/lines could be identified in the Fourier transform infrared (FTIR) spectra, Raman spectra and/or in energy dispersive spectroscopy (EDS) spectra, fact that indicate the sample's purity. The results of the XPS studies highlighted the purity of HAp_MMT sample. The results of batch adsorption experiments highlight that HAp_MMT composites exhibit a strong affinity towards lead ions and that were extremely efficient in removing the metallic ions from the contaminated solutions. These results suggest that HAp_MMT composites could be promising candidates for the development of novel technologies for water decontamination.

INTRODUCTION

Worldwide, heavy metal contamination of both water and soil is a significant concern for the environment. Contamination of water and soil with heavy metals can have extremely harmful effects

on both ecosystems and human health. Heavy metals, such as lead, mercury, cadmium, arsenic and chromium, are natural elements that can accumulate in the environment through various industrial, agricultural and human activities [1-2]. Heavy metals are considered among the most toxic and can accumulate in living organisms, leading to serious health problems or even death in certain cases. For example, exposure to lead can cause neurological damage, especially in children, while mercury can damage the central nervous system and affect brain development [1-2]. In this context, the family of clay minerals represent an important category of adsorbent materials that could be used for the adsorption of contaminants from aqueous systems. From this family of adsorbents, those based on montmorillonite (MMT), a 2:1 type clay mineral, have been extensively studied. MMT is a clay-type mineral with a special structure, which gives it a good cation exchange capacity [3-4]. Regarding the use as adsorbent, MMT and its derivatives have numerous advantages: (a) MMT is cheap and could be used as a highly efficient adsorbent for various cationic contaminants [5-7] and also the MMT surface can be relatively easily modified to obtain new types of adsorbents [8-9]; (c) adsorbents based on MMT can be used for the adsorption of a wide range of contaminants [9-10]. Therefore, tacking in consideration all these aspects, the MMT-based adsorbents have attracted the attention of researchers who are seeking new materials with high adsorption capacities for removing various type of pollutants from contaminated waters/soils. Also, hydroxyapatite (HAp) and its derivatives could represent an alternative solution for the treatment of wastewater contaminated with heavy metals [11-14]. This is mainly due to its unique properties and structure that give it a high ion exchange capacity and high adsorption affinity towards many pollutants [15-18]. Thus, we obtained a new composite based on HAp and MMT (HAp_MMT), using a cheap and efficient synthesis method, and preliminary studies of its structure, chemical composition and morphology were carried out. Moreover, preliminary studies were done in order to evaluate the lead adsorption capacity of these new composites. Our first results suggest that materials based on the HAp_MMT are promising candidates for water decontamination applications.

EXPERIMENTAL

In order to obtain the new composite material based on hydroxyapatite and montmorillonite (HAp_MMT) appropriate amounts of $(NH_4)_2HPO_4$ and $Ca(NO_3)_2*4H_2O$ were used to prepare aqueous solutions. Further, MMT (10 g) was added to the $(NH_4)_2HPO_4$ solution and stirred at 40 ^oC for 30 min. The solution of $Ca(NO_3)_2*4H_2O$ was added in the solution containing MMT stirred for 4 h. The obtained precipitate was washed with double-distilled water and dried at 100^oC. A Quanta Inspect F type microscope coupled with an EDAX/2001 device was used to analyze the HAp_MMT morphology and composition. Image J software was used for the 3D representation of the SEM micrographs [19]. For the AFM studies, pellets were made from HAp_MMT composites, whose surface was investigated. The topography of the pellets obtained from HAp_MMT nanocomposites was obtained by atomic force microscopy studies performed in semi-contact mode under normal atmospheric conditions and at room temperature. The topographies were recorded on an area of 10x10 μm^2. FTIR spectra were collected with the aid of a Perkin Elmer SP 100 spectrometer equipped with an attenuated total reflection (ATR) module. Raman spectra was recorded with the aid of an LABRAM HR Evolution spectrometer. Raman spectroscopy studies were performed at room temperature, using a HeNe laser (633nm/17 mW). For the X-ray photoelectron spectroscopy (XPS) studies, a SPECS Spectrometer with a PHOIBOS 150 analyser was used. Specs XR-50M RX source operated on a non-monochromatic Mg anode (Ex=1253.6eV) at 300W. The acquisition was made with a Pass Energy of 50eV for the extended spectrum. All recorded XPS spectra were analyzed

using Spectral Data Processor v. 2.3 (SDP) software. The capacity of HAp_MMT nanocomposites in removing lead ions from contaminated solutions was evaluated using batch adsorption experiments. The experiments were conducted at room temperature and in atmospheric conditions in agreement with the previous studies [17].

RESULTS AND DISCUSSION

Results regarding the morphology of HAp_MMT composites were obtained by atomic force microscopy (AFM) and scanning electron microscopy (SEM) studies. The results obtained by AFM scanning of the surface of the HAp_MMT pellets are presented in Figure 1. The results of the atomic force microscopy studies performed on the HAp_MMT nanocomposites revealed that the pellets surface is relatively smooth and homogeneous, being composed of nanometer-sized particles. In addition, the results of the AFM studies also highlighted the fact that the nanocomposites do not form visible conglomerates. Information about the surface roughness of the HAp_MMT pellets was also obtained by determining the R_{RMS} (roughness parameter) from the two-dimensional image of the surface topography. The determined R_{RMS} value was approximately 55.80 nm for the entire image. AFM studies revealed that the obtained nanocomposites have nanometric dimensions, do not form conglomerates and are homogeneous.

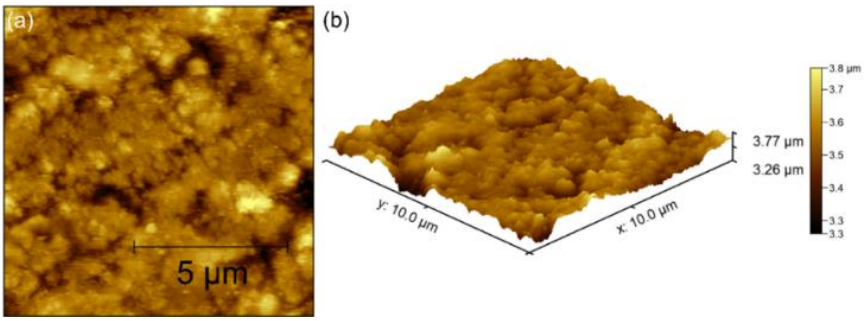

FIGURE 1 Two-dimensional AFM image of the topography of the tablet surface obtained from HAp_MMT nanocomposites (a) and its three-dimensional representation (b).

The morphology of HAp_MMT nanocomposites was studied by scanning electron microscopy (SEM), and the results are shown in Figure 2 a,b. In the SEM micrographs, it can be observed that particles possess nanometric dimensions. Also, the SEM results highlight an ellipsoidal morphology of the nanoparticles. It can be observed in Figure 2a the tendency of HAp_MMT nanoparticles to agglomerate. Information on the chemical composition of the HAp_MMT sample was obtained both EDS and XPS studies. The EDS spectra (Figure 3a) shows the presence of both the chemical elements found in the composition of HAp and of MMT. In the EDS spectra, only the presence of Ca K, P K, O K, Mg K, Al K, Si K, Na K and Fe K without highlighting the presence of additional lines that could be associated with the presence of impurities in the analyzed sample. Therefore, the results of the EDS studies showed that the HAp_MMT type nanocomposites are pure.

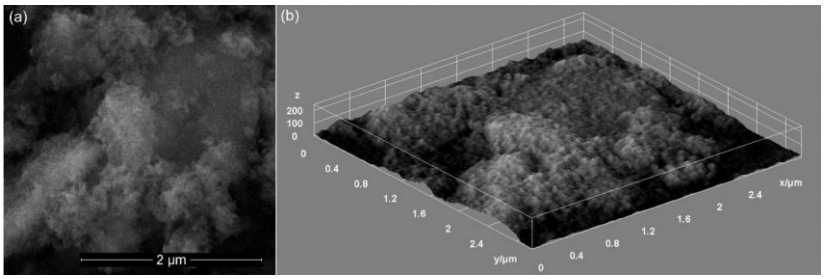

FIGURE 2 SEM micrograph (**a**) characteristic of HAp_MMT nanocomposites. 3D representation of the 2D SEM micrograph (**b**).

The results of the XPS studies highlighted both the presence of hydroxyapatite and montmorillonite in the analyzed sample (HAp_MMT). The general spectrum of HAp_MMT type nanocomposites was presented in Figure 3b.

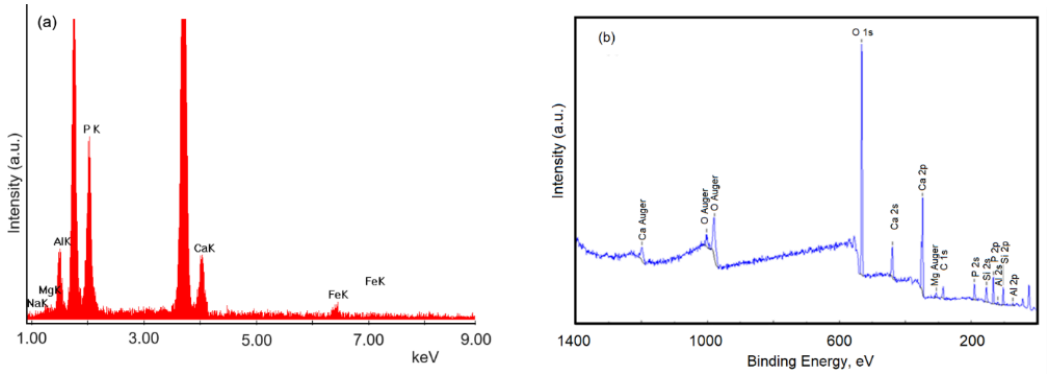

FIGURE 3 EDS (a) and XPS survey spectra of HAp_MMT (b)

In the general XPS spectrum of the HAp_MMT sample, the presence of peaks corresponding to C1s, Ca2p, P2p, O1s, Si2p, Al2p and Mg2p can be observed. The spectra were calibrated considering the C1s peak associated with C-C and C-H bonds located at 284.8eV. The peaks corresponding to the binding energies of Ca2p, O1s and P2p are specific to hydroxyapatite. On the other hand, the maxima associated with the bond energies of Si2p, Al2p and Mg2p are specific to montmorillonite and demonstrate its presence in the studied nanocomposite (HAp_MMT). At the same time, the absence of additional peaks in the XPS spectrum shows that the synthesized nanocomposite is pure.

The FTIR spectra (figure 4) obtained for HAp_MMT demonstrates the presence of the vibration bands associated with the phosphate groups in the HAp structure, but also the vibration bands associated with the groups from the MMT structure. In the case of MMT, the presence of maxima that can be attributed to Si-O bonds can be observed at approximately 799 cm^{-1} [20]. The vibration bands associated tothe MMT structure, are overlapped with the maxima associated with the vibration of the phosphate groups in the 900-1200 cm^{-1} spectral region. Other maxima that could be associated with vibrations (Al–O–Si) in the MM K10 structure is observed at 527 cm^{-1} [20]. The presence of the fundamental vibrational modes of the phosphate groups, they can be observed in the FTIR spectra (figure 2a) at approximately 466 cm^{-1} (ν_2), 565 and 603 cm^{-1} (ν_4), 962 cm^{-1} (ν_1) and 1020-1120 cm^{-1} (ν_3) [21]. The vibration bands found at 631 and 3411 cm^{-1}, belong to the OH^- groups in the HAp structure [21]. The broad vibration bands found in the spectral domains 1600-1700 cm^{-1} [22-23] and 3400-3800 cm^{-1} can be attributed to water adsorbed on the surface [21].

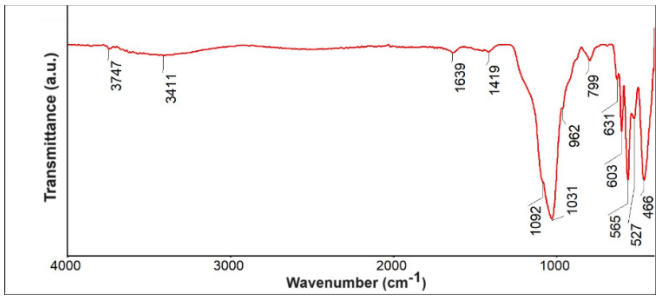

FIGURE 4 FTIR spectra obtained for the HAp_MMT powder.

Through Raman spectroscopy studies, complementary information is obtained regarding the presence of vibration bands specific to the HAp/MMT type nanocomposite structure. The Raman spectrum of the HAp/MMT sample is shown in Figure 5. The analysed sample (HAp/MMT) has a vibration band at 962 cm-1 which can be associated to specific vibration modes of symmetric elongation of P-O bonds (ν_1). The vibration band observed at 490 cm^{-1} is specific to O-P-O bonds (ν_2). Also, the vibration bands observed at approximately 1065 cm^{-1}, 1021 cm^{-1} and 1048 cm^{-1} correspond to the asymmetric elongation of the P-O bonds (ν_3) [24]. Moreover, the maxima at approximately 508 cm^{-1}, 567 cm^{-1} and 602 cm^{-1} are mainly attributed to the O-P-O bond (ν_4) [24]. Regarding the vibrational bands associated with the groupings in the MMT structure, they generally have specific maxima at approximately ~430 and 710 cm^{-1}. The specific vibration bands of Al–OH–Al and SiO_4 from the MMT K10 structure are found at 914 and 710 cm^{-1}, respectively, in the Raman spectrum [20].

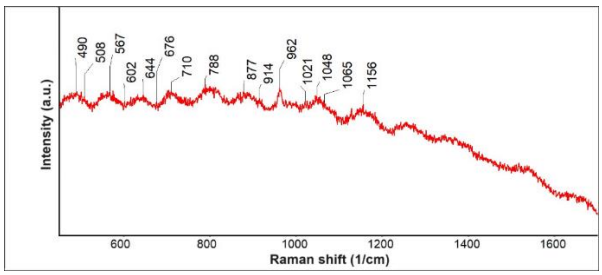

FIGURE 5 Raman spectra obtained for the HAp_MMT powder.

In general, the peaks in the Raman spectrum associated with MMT have a low intensity. Also, according to studies reported by A. Wang et al. [25] in the region of 1100 to 600 cm^{-1} there are numerous maxima specific to MMT. The maximum at 788 cm^{-1} could be associated with the ν(AlOH) vibration from the MMT structure [26]. Therefore, we can conclude that the results obtained by Raman spectroscopy are in good agreement with the results obtained by FTIR spectroscopy.
Preliminary information regarding the efficiency of HAp_MMT nanocomposites in removing Pb^{2+} was determined using the data obtained from the batch adsorption experiments and is depicted in Figure 6a. The percentage of removal efficiency (R%) and its correlation with the initial concentration of Pb^{2+} from the contaminated aqueous solutions is depicted in Figure 2b. The results highlighted that the removal efficiency of lead ions by HAp_MMT nanocomposites was higher than 95% and that was influenced by the initial Pb^{2+} concentration from the contaminated solution. The

influence of the pH value on the removal efficiency of lead ions by HAp_MMT nanocomposites was also evaluated in the range of 2-7 with contaminated solutions having a Pb^{2+}concentration of 50 mg/L. The results of the experiments depicted in Figure 6 b determined that the efficiency of HAp_MMT in the removal of Pb^{2+} increased greatly with the increase of the pH value from 2 to 4. More than that, the results also highlighted that between the pH values of 4 and 7 the removal efficiency (R%) remained constant. These results were in accord with previously reported data [17, 27-30]. In their study, Liao et al [30] reported that the inferior removal efficiency of Pb^{2+} at a low pH value might be due to fact the low pH supports the increase of the $CaOH_2^+$ and POH^0 populations that contribute to the achievement of a positive charge which creates a less favourable medium for the complexation of Pb^{2+}.

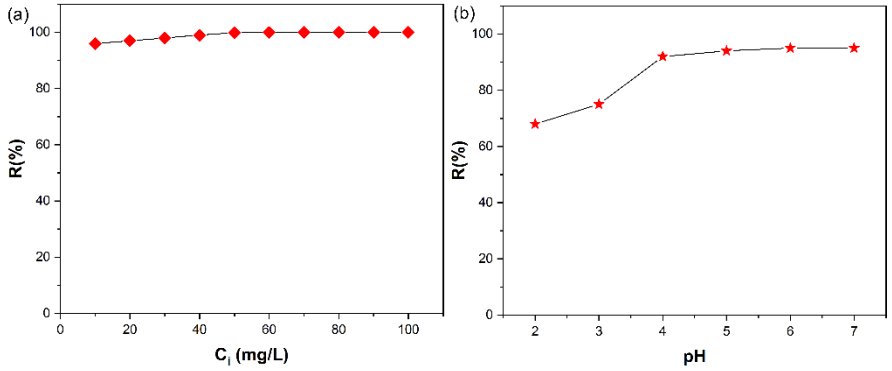

FIGURE 6 The removal percentage of Pb^{2+} ions from contaminated aqueous solutions using HAp_MMT nanocomposites (**a**) and the removal efficiency (R%) at different pH values (**b**)

CONCLUSIONS

In this study, were obtained new nanocomposite based on HAp and MMT with potential applications in the decontamination of polluted waters. Preliminary studies were carried out regarding the composition, structure and morphology of the new nanocomposites. The results of the EDX studies demonstrate the purity of the composite based on HAp_MMT. The presence of vibration bands specific to both the HAp structure and those specific to the MMT structure was highlighted by the results of the FTIR studies. The results of the SEM studies demonstrate, the nanometric size and the acicular morphology of the HAp_MMT powders. The results obtained for the removal efficiency (R%) emphasized that HAp_MMT nanocomposites exhibited a strong affinity towards Pb^{2+} ions having a percentage of removal efficiency higher than 98% for initial Pb^{2+} concentration above 30 mg/L. The preliminary results suggest that the HAp_MMT composite materials could be used in applications in the decontamination of polluted waters.

ACKNOWLEDGEMENTS

This work was funded by the Core Program of the National Institute of Materials Physics, granted by the Romanian Ministry of Research, Innovation and Digitalization through the Project PC1-PN23080101 and by the Project to Support Institutional Excellence contract 35PFE/2022 (funded by the Romanian Ministry of Research, Innovation and Digitization).

REFERENCES

1.Lin, L.; Yang, H.; Xu, X. Effects of water pollution on human health and disease heterogeneity: a review. *Front. Environ. Sci.* 2022,10, 880246.

2.Xu, X.; Yang, H.; Li, C. Theoretical Model and Actual Characteristics of Air Pollution Affecting Health Cost: A Review, *Int. J. Environ. Res. Public Health* 2022, 19, 3532.

3.Zhu, R.; Chen, Q.; Zhou, Q.; Xi, Y.; Zhu, J.; He, H. Adsorbents based on montmorillonite for contaminant removal from water: A review, *Appl. Clay Sci.* 2016, 123, 239-258.

4.Brigatti, M.F.; Galan, E.; Theng, B.K.G., Structure and mineralogy of clay minerals. In: Bergaya, F., Lagaly, G.,Eds.; Handbook of Clay Science, Part A, second ed. Elsevier, Amsterdam, 2013, pp. 21–82.

5.Lagaly, G., Surface and interlayer reactions: bentonites as adsorbents. In: Churchman, G.J., Fitzpatrick, R.W., Eggleton, R.A.,Eds.; Clays Controlling the Environment Proceedings of the 10th International Clay Conference, Adelaide, Australia 1993. CSIRO Publishing, Melbourne, 1995, pp. 137–144.

6.Bailey, S.E.; Olin, T.J.; Bricka, R.M.; Adrian, D. A review of potentially low-cost sorbents for heavy metals, *Water Res.* 1999, 33, 2469–2479.

7.Lagaly, G., Ogawa, M., Dekany, I. Clay mineral–organic interactions. In: Bergaya, F., Lagaly, G., Eds.; Handbook of Clay Science, Part A, second ed. Elsevier, Amsterdam, 2013, pp. 435–506.

8.Ake, C.L.; Wiles,M.C.; Huebner, H.J.;McDonald, T.J.; Cosgriff, D.; Richardson, M.B.; Donnelly, K.C.; Phillips, T.D. Porous organoclay composite for the sorption of polycyclic aromatic hydrocarbons and pentachlorophenol from groundwater, *Chemosphere* 2003. 51, 835–844.

9.Yuan, G.D.; Theng, B.K.G.; Churchman, G.J.; Gates, W.P. Clays and clay minerals for pollution control. In: Bergaya, F., Lagaly, G.,Eds.; Handbook of Clay Science, Part A, second ed. Elsevier, Amsterdam, 2013, pp. 587–644.

10.Alkaram, U.F. ; Mukhlis, A.A.; Al-Dujaili, A.H. J. The removal of phenol from aqueous solutions by adsorption using surfactant-modified bentonite and kaolinite, *Hazard. Mater*. 2009, 169, 324–332.

11.Amenaghawon, A.N.; Anyalewechi, C.L.; Darmokoesoemo, H.; Kusuma, H.S. Hydroxyapatite-based adsorbents: Applications in sequestering heavy metals and dyes, *Environ. Manage.* 2022, 302, 113989.

12.De Gisi, S.; Lofrano, G.; Grassi, M.; Notarnicola, M. Characteristics and adsorption capacities of low-cost sorbents for wastewater treatment: A review, *Sustain. Mater. Technol*. 2016, 9, 10–40.

13.El-Gendy, M.M.A.A.; Abdel-Moniem, S.M.; Ammar, N.S.; El-Bondkly, A.M.A. Bioremoval of heavy metals from aqueous solution using dead biomass of indigenous fungi derived from fertilizer industry effluents: isotherm models evaluation and batch optimization, *Biometals* 2023, 36, 1307-1329, 10.1007/s10534-023-00520-x.

14.Timková, I.; Maliničová, L.; Nosáľová, L. ; Kolesárová, M.; Lorková, Z.; Petrová, N.; Pristaš, P.; Kisková, J. Genomic insights into the adaptation of Acinetobacter johnsonii RB2-047 to the heavy metal-contaminated subsurface mine environment, *Biometals* 2023. 10.1007/s10534-023-00555-0.

15.Ciobanu, C.S.; Predoi, M.V.; Buton, N.; Megier, C.; Iconaru, S.L.; Predoi, D. Physicochemical Characterization of Europium-Doped Hydroxyapatite Thin Films with Antifungal Activity, *Coatings* 2022, 12, 306.

16.Predoi, D.; Iconaru, S.L.; Predoi, M.V.; Motelica-Heino, M. Removal and Oxidation of As(III) from Water Using Iron Oxide Coated CTAB as Adsorbent, *Polymers* 2020, 12(8), 1687.

17.Predoi, S.A. ; Ciobanu, S.C. ; Chifiriuc, C.M. ; Iconaru, S.L. ; Predoi, D. ; Negrila, C.C. ; Marinas, I.C. ; Raaen, S. ; Rokosz, K. ; Motelica-Heino, M. Sodium bicarbonate-hydroxyapatite used for removal of lead ions from aqueous solution, *Ceram. Int.* 2023, 50(1), Part B, 1742-1755.

18.Predoi, D.; Predoi, M.V.; Iconaru, S.L.; Ech Cherif El Kettani, M.; Leduc, D.; Prodan, A.M. Ultrasonic Measurements on β Cyclodextrin/Hydroxyapatite Composites for Potential Water Depollution, *Materials* 2017, 10(6), 681.

19.Image J Website. Available online: http://imagej.nih.gov/ij.

20.Vaculíková, L.; Plevová, E.; Ritz, M. Characterization of Montmorillonites by Infrared and Raman Spectroscopy for Preparation of Polymer-Clay Nanocomposites, *Nanosci. Nanotechnol*. 2019, 19(5), 2775–2781.

21.Ciobanu, C.S.; Predoi, D.; Chapon, P.; Predoi, M.V.; Iconaru, S.L. Fabrication and Physico-Chemical Properties of Antifungal Samarium Doped Hydroxyapatite Thin Films, *Coatings* 2021, 11(12), 1466.

22.Laisney, J.; Chevallet, M.; Fauquant, C.; Sageot, C.; Moreau, Y.; Predoi, D.; Herlin-Boime, N.; Lebrun, C.; Michaud-Soret, I. Ligand-Promoted Surface Solubilization of TiO_2 Nanoparticles by the Enterobactin Siderophore in Biological Medium, *Biomolecules* 2022, 12(10), 1516.

23.Laisney, J.; Rosset, A.; Bartolomei, V.; Predoi, D.; Truffier-Boutry, D.; Artous, S.; Bergé, V.; Brochard, G.; Michaud-Soret, I. TiO_2 nanoparticles coated with bio-inspired ligands for the safer-by-design development of photocatalytic paints, *Environ. Sci. Nano* 2021, 8(1),297-310.

24.Iconaru, S.L.; Predoi, D.; Ciobanu, C.S.; Motelica-Heino, M.; Guegan, R.; Bleotu, C. Development of Silver Doped Hydroxyapatite Thin Films for Biomedical Applications, *Coatings* 2022, 12(3), 341.

25.Wang, A.; Freeman, J.J.; Jolliff, B.L. Understanding the Raman spectral features of phyllosilicates, *Raman Spectrosc.* 2015. 46(10),829-845.

26.Ritz, M.; Vaculíková, L.; Kupková, J.; Plevová, E.; Bartoňová, L. Different level of fluorescence in Raman spectra of montmorillonites, *Vib. Spectrosc*. 2016, 84,7-15.

27.Predoi, S.-A.; Ciobanu, C.S.; Motelica-Heino, M.; Chifiriuc, M.C.; Badea, M.L.; Iconaru, S.L. Preparation of Porous Hydroxyapatite Using Cetyl Trimethyl Ammonium Bromide as Surfactant for the Removal of Lead Ions from Aquatic Solutions, *Polymers* 2021; 13(10), 1617.

28.Hasan, S.H.; Srivastava, P.; Talat, M. Biosorption of lead using immobilized Aeromonas hydrophila biomass in up flow column system: Factorial design for process optimization, *Hazard Mater.* 2010, 177, 312-322.

29.Mousa, S.M.; Ammar, N.S.; Ibrahim, H.A. J. Removal of lead ions using hydroxyapatite nano-material prepared from phosphogypsum waste, *Saudi Chem. Soc.* 2016, 20, 357-365.

30.Liao, D.; Zheng, W.; Li, X.; Yang, Q.; Yue, X.; Guo, L.; Zeng, G. Removal of lead(II) from aqueous solutions using carbonate hydroxyapatite extracted from eggshell waste, *J. Hazard Mater* 2010, 177, 126-130.

DYNAMIC MECHANICAL CHARACTERIZATION OF 3D-PRINTED PLA PLATES WITH DIFFERENT PRINTING ORIENTATIONS AND NOZZLE TEMPERATURES

A. Georgali -Fickel[1], S.P. Zaoutsos[2], L.C. Kontaxis[1], G.C. Papanicolaou[1*]

[1]Dept. of Mechanical Engineering and Aeronautics, University of Patras, Greece, [*]E-mail: gpapan@upatras.gr

[2]Department of Energy Systems, University of Thessaly, Greece.

ABSTRACT

Polylactic acid or polylactide (PLA) is a biodegradable and bioactive thermoplastic aliphatic polyester derived from renewable sources such as corn starch. PLA is widely used in rapid prototyping and additive manufacturing applications. The present work is focused on the evaluation of the dynamic mechanical properties of 3D printed structures manufactured by FDM (Fused Deposition Modeling) method in dependence on the printing nozzle temperature and printing orientation. Poly-lactic acid (PLA) was chosen as the material for FDM. Measurement of dynamic mechanical properties was conducted by dynamic mechanical analysis (DMA). The results showed that PLA dynamic mechanical properties as well as Tg-values strongly depended on both the printing temperature and printing orientation. Also, the glass transition temperature increased with increasing nozzle temperature.

INTRODUCTION

Additive manufacturing (commonly known as 3D printing) responds to industry demands for quick, high-quality, and low-cost development. Many other types of 3D printing techniques have been developed over the years, including SL (stereolithography), SLS (selective laser sintering), SLM (selective laser melting), LOM (laminated object manufacturing), FDM (fused deposition modeling), and others. The key advantages of 3D printing are the ability to create complicated structures, the process's high controllability, and the lack of the need for molds. The properties of the printed structure differ dramatically from the properties of the base material created by molding or other traditional production methods. In terms of mechanical properties, the testing specimens are weaker and exhibit anisotropy, which could be attributed to the printing orientation and the non-ideal adhesion of layers together. Many process variables, such as machine calibration, nozzle temperature, nozzle diameter, bed temperature, ambient temperature, printing head movement speed, printing orientation, and so on, influence the attributes of printed structures. Because polymers are particularly sensitive to their temperature history, the procedure affects mechanical and thermal properties. In the present work, the effect of both nozzle temperature and printing orientation on both the Tg temperature and storage modulus of 3D printed PLA plates is studied.

MATERIALS AND EXPERIMENTAL METHODS

DMA measurements were executed using PLA rectangular specimens with mean dimensions 3.50x12x60mm cut from 3D Printed PLA plates. Three different printing orientations (0^0, 45^0 and 90^0) and four different nozzle temperatures (210, 220, 230 and 240^0C) were applied to study the effect of these manufacturing parameters on both the Tg and the storage modulus values of PLA specimens.

RESULTS AND DISCUSSION

A. Effect of nozzle temperature:

Thermoplastics, during their preparation stage, may develop crystallites. The formation of crystallites occurs during the cooling phase. The faster the cooling rate, the smaller the crystallites. Conversely, the slower the cooling rate, the larger the crystals that will grow. The nozzle temperature has a significant impact on the mechanical properties of the 3D printed object [1,2]. Specifically, the nozzle temperature influences the rheology of the polymer melts passing through the nozzle, as well as the crystallinity of the 3D printed structure, which are the major characteristics influencing the mechanical properties of the 3D printed structure. Furthermore, the nozzle temperature might alter the properties of a fully 3D printed layer while printing the subsequent layers. At temperatures exceeding the melting temperature, Tm, there is a lot of energy in the system, and the segmental motion of the polymer chains is too fast for stable nuclei to form and crystalline development to happen [3,4]. However, as the temperature is dropped below Tm, melt viscosity increases, increasing the possibility of nucleation and the formation of a microstructure of few but very big crystals. As the temperature is dropped further and the viscosity increases, the rate of crystallization reaches a maximum where conditions favor both nucleation and development of crystallites [3]. When approaching Tg, the system has substantially less energy and the molecular mobility of the polymer chains is greatly diminished. There is a much lower nucleation barrier opposing the creation of stable nuclei in such a viscous condition, however transport of the chains to the crystal growth front is hampered due to reduced molecular mobility [4]. This results in a microstructure with a greater number of crystallites but a much smaller size. Below Tg, the polymer chains are effectively 'frozen' in situ, and no further crystallization can occur [5, 6].

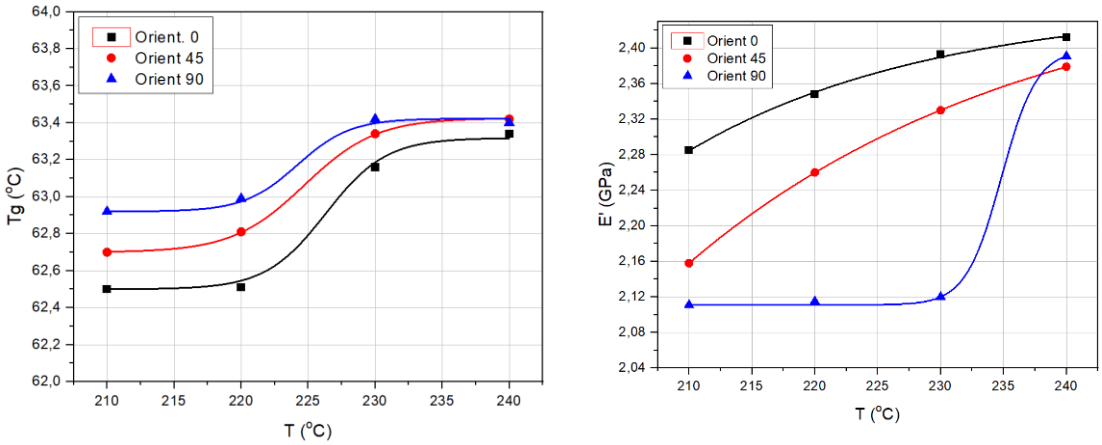

FIGURE 1 Effect of nozzle temperature on Tg and E' values for different printing orientations

Crystals perturb the amorphous phase and diminish its segmental mobility, giving the amorphous phase a Tg distribution. Amorphous regions adjacent to the crystal surface will experience the greatest degree of restriction, with the effect decreasing as you advance through the interface and reach the amorphous phase unconstrained by crystallites and with properties equivalent to those of the bulk amorphous material [7, 8]. As a result of the above-mentioned mechanisms, both Tg and storage modulus values are expected to increase with increasing nozzle temperature. These results are shown in Fig. 1.

B. Effect of printing orientation:

The printing orientation affect the mechanical properties of the FDM 3D-printed parts because it affects the anisotropy of the printed part (see Figure 2) [9]. Therefore, this study aimed to examine the 3D printing orientation on the dynamic mechanical properties of PLA 3D-printed specimens.

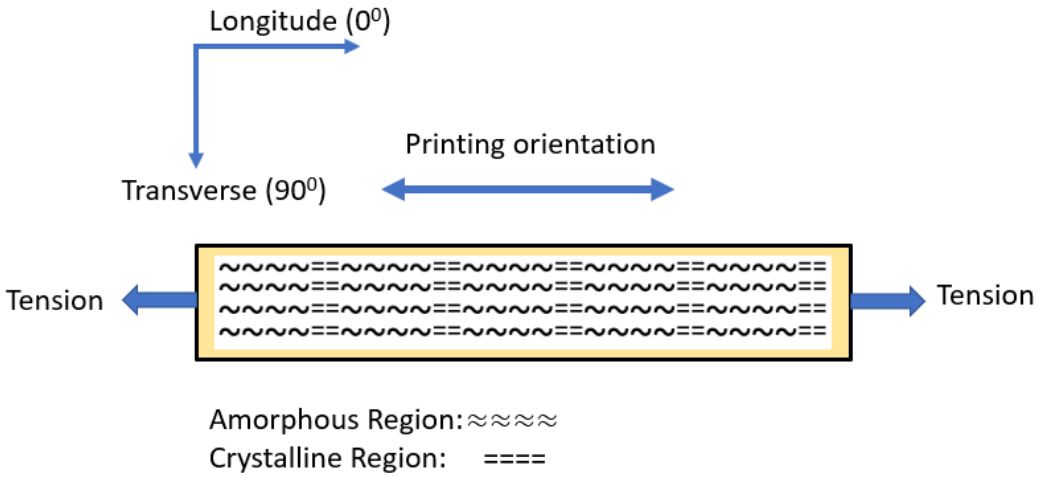

FIGURE 2 Effect of printing orientation on the crystallite's orientation and PLA plate anisotropy

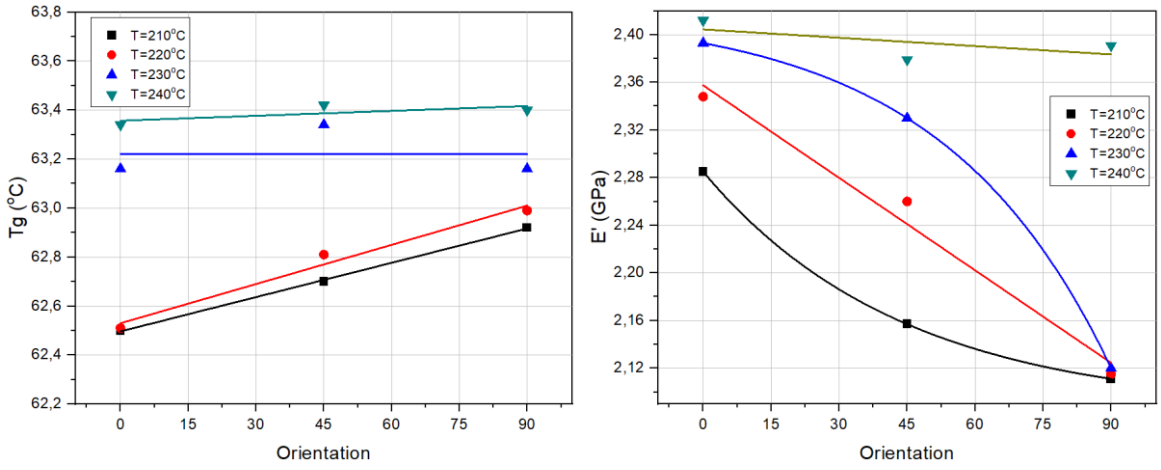

FIGURE 3 Effect of printing orientation on the Tg and E' values for different nozzle temperatures

As already discussed, by increasing the nozzle temperature an increase in the degree of crystallinity results. On the other hand, printing orientation introduces anisotropy on the printed PLA specimens. Thus, the properties of the printed PLA specimens on the printing longitudinal direction are mainly

affected by the crystals developed within the PLA structure, while the respective properties in the transverse direction, are mainly dominated by the amorphous phase properties. In Figure 3, the variation of both Tg and storage modulus values are plotted vs the printing orientation angle. It can be observed that as the printing angle is increased, Tg values increase while storage modulus values decrease, while at the same time, in both cases, by increasing nozzle temperature, an increase in Tg and a respective increase in storage modulus values is observed due to the increase in the degree of crystallinity.

CONCLUSIONS

In the present work, the effect of nozzle temperature and printing orientation of 3D-printed PLA plates on the Tg and storage modulus values was investigated. The main conclusions derived are as follows:

- For all printing orientations, both Tg and storage modulus values increase with increasing nozzle temperature.
- As the printing angle is increased, Tg values increase while storage modulus values decrease, while at the same time, in both cases, by increasing nozzle temperature, an increase in Tg and a respective increase in storage modulus values is observed due to the increase in the degree of crystallinity.

REFERENCES

1. Syrlybayev, D.; Zharylkassyn, B.; Seisekulova, A.; Akhmetov, M.; Perveen, A.; Talamona, D. Optimisation of Strength Properties of FDM Printed Parts—A Critical Review, *Polymers* 2021, 13, 1587.

2. Vanaei, H.R.; Shirinbayan, M.; Deligant, M.; Khelladi, S.; Tcharkhtchi, A. In-Process Monitoring of Temperature Evolution during Fused Filament Fabrication: A Journey from Numerical to Experimental Approaches, *Thermo* 2021, 1, 332–360.

3. Cowie, J.M.G. Polymers: chemistry and physics of modern materials. 2nd Ed. London: Blackie Academic & Professional 1991, 448 p.

4. Di Loernzo, M.L.; Silvestre, C. Non-isothermal crystallisation of polymers, *Progress in Polymer Science* 1999, 24, 917-950.

5. Gibbs, J.H.; Di Marzio, E. Nature of the glass transition and the glassy state. *The Journal of Chemical Physics* 1958, 28(3), 373-383.

6. Richardson, M.J. The glass transition region, In: Mathot, V.B.F. (ed.) Calorimetry and thermal analysis of polymers, Munich: Hanser Publishers 1994, 169-188.

7. Struik, L.C.E. The mechanical and physical ageing of semicrystalline polymers 1, *Polymer* 1987, 28(9), 1521-1533.

8. Struik, L.C.E. The mechanical behaviour and physical ageing of semicrystalline polymers 2, *Polymer* 1987, 28, 1534-1542.

9. Yang, C.; Tian, X.; Li, D.; Cao, Y.; Zhao, F.; Shi, C. Influence of thermal processing conditions in 3D printing on the crystallinity and mechanical properties of PEEK material, *Journal of Materials Processing Technology* 2017, 248, 1-7.

MODELING OF THE THERMAL FIELD IN THE CASE OF AUTOMATED WELDING IN A PROTECTIVE GAS ENVIRONMENT

D.F. Nitoi[1], O. Chivu[1], C. Enache[1], A. Crangureanu[1], M. Faladau[2]

[1] University Politechnica of Bucharest, Splaiul Independentei no. 313, sect. 6, 060032 Bucharest, Romania, Corresponding Author: nitoidan@yahoo.com (Dan Florin Nitoi)

[2]University Lucian Blaga of Sibiu, Bulevardul Victoriei 10, 550024, Sibiu, Romania,

ABSTRACT

The technological process of welding is currently a very well-known technology that is used in extremely many engineering fields. One of the problems of the welding process is the definition of the parameters of the technological regime that must be calculated in each individual case, as well as the analysis of the physico-chemical phenomena that take place in the bath of molten metal as well as in the thermally influenced zone. Research using the finite element method can be applied with very good results in work areas where mounting sensors that can make direct measurements is very difficult or impossible. The studies presented in the article present the analysis of the thermal phenomena in the thermally influenced zone and in the molten metal bath in the case of butt welding in a protective gas environment of two metal plates.

INTRODUCTION

Typically, mechanics and heat transfer problems are initially approached with analytical tools. If the geometry and physics are simple enough, it gives accurate results. Clever application of simplifications can increase the level of complexity that can be analyzed. The reality of complex industrial products and processes is that simple physical relationships are quickly replaced by complex partial differential equations and complicated geometries. An alternative solution is to use advanced computer-based work tools such as Finite Element Analysis (FEA). The main advantage of FEA is that it produces a much more detailed set of results than experimental investigations and is often faster and less expensive [1-5]. Considering that, the researches presented refer to the determination of the temperature field in the case of making a welded joint of two metal plates of type EH 35 for which the working technological parameters are presented. Starting from these elements, an analysis with finite elements implemented through the Ansys program was used. Here, the following are considered as input data: the geometric shape of the two metal plates, the mechanical and thermal characteristics of the base materials, as well as the temperature applied in the area of the welded seam determined experimentally. Figure 1a presents the experimental stand with the two metal plates and the theoretical geometric shape of the welded joint, figure1b the welded seam and figure 1c the theoretical shape of the welded seam that represents the input data for the mathematical model.

(a) (b) (c)

FIGURE 1 Input data from experiments: (a) experimental stand for plates welding; (b) welded seam; (c) theoretical section of welded seam

Paper presents also mechanical and thermal properties of the material from which the two plates are made depending on the temperature and also the type of element used in the spatial discretization of geometries.

EXPERIMENTAL

Based on the analysis with finite elements, the evaluation of the state of temperatures, deformations and stresses inside the completed structure was carried out. For this, according to the experiments, an analysis was made for each of the two welding cords, the first basic one and the second one that makes the elevation. In each case, the length of the welded cord was divided into 60 steps within the time t = 450 sec in which it is made. Since it is very difficult to represent all the steps, the results were calculated for steps 4, 15, 30, 45 and 57. In all the points thus selected, the following was determined: the temperature map, the heat flow, the mechanical deformations and the stress state resulting from the application of the temperature of the electric arc.

RESULTS AND DISCUSSION

The results of the analysis with finite elements are based on a series of calculations that manage to create an image of what happens inside the welded seam and in the thermally influenced zone. As an example, in figure 1a, for step 30, the thermal field in cross section is shown, in figure 1b the thermal gradient, in figure 1c the temperature variation over time and in figure 1d mechanical stress on OZ axis [6-11].

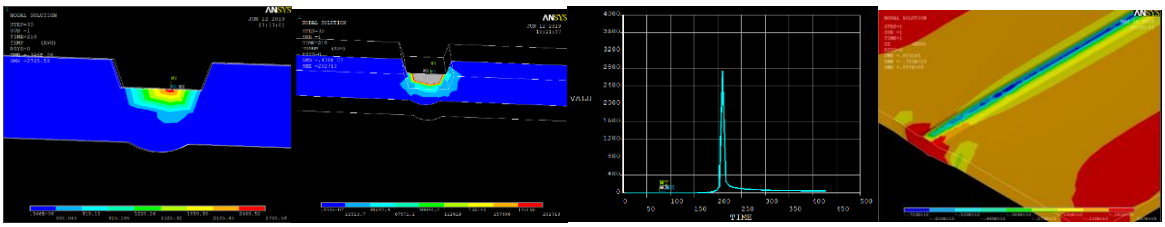

(a) (b) (c) (d)

FIGURE 2 FEM analysis in the midpoint of the welded seam: (a) temperature variation; (b) thermal gradient; (c) temperature variation in time; (d) OZ stress

CONCLUSIONS

Modeling and simulation using the finite element method is currently a very important theoretical research method that can provide answers, very close to the studied phenomena, in fields of work where experimental methods cannot be applied. In the case of studying the thermal phenomena and the stress state that occur during electric arc welding of metallic materials, this method can be applied directly and provides answers (such as the temperature inside the molten metal bath or the state of stress inside material structure, very clear and often impossible by experimental methods. In this sense, the thermal and mechanical phenomena that occur when welding two metal plates by depositing two layers were studied. The input data are made up of the geometry of each individual point and the mechanical and thermal properties of the materials used in the welded joint. As output data, obtained after a transient analysis (over time), the following were obtained:

- thermal fields studied at several points of the welding process. These were studied in top view as well as in transverse and longitudinal sections;
- thermal flow fields also analyzed in longitudinal and transverse sections;
- thermal gradients in the same sections.

In addition to these output data, the time variations of the temperatures in certain points of the structure for certain steps were also presented.

REFERENCES

1. Rao, S.S. The finite element method in Engineering, Butterworth-Hainemann, Elsevier 2018.

2. Huebner, K.H. Dewhirst, D. L.; Smith, D.E.; Byrom, T. G. The finite element method for engineers, John Wiley & Sons – 2001, 744 pp.

3. Larson, M.G.; Bengzon, F. The finite element method: Theory, Implementation and Applications, Springer Berlin, Heidelberg 2010, 395 pp.

4. Madenci, E.; Guven, I. The finite element method and applications in engineering using ANSYS, Springer International Publishing 2015, 657 pp.

5. Petcu, C.M.; Nițoi, D.F.; Mercut, V.; Tuculina, M.J.; Iliescu, A.A.; Croitoru, C.; Diaconu, O.A.; G., Gheorghita, L.M.; Iliescu, A. Masticatory tensile developed in upper anterior teeth with chronic apical periodontitis. A finite-element analysis study, *Romanian journal of morphology and embryology* 2013, 54(3), 587-592.

6. Wang, R.; Zhang, J.; Serizawa, H.; Murakawa, H. Study of welding inherent deformations in thin plates based on finite element analysis using interactive substructure method, *Materials & Design.* 2009, 30(9), 3474-3481.

7. Jang, C.D.; Lee, C.H.; D.E. Ko, D.E. Prediction of welding deformations of stiffened panels, Proc Inst Mech Eng Part M: *J Eng Maritime Environ* 2002, 216 (2), 133-143.

8. Seo, S.I.; Jang, C.D. A Study on the Prediction of Deformations of Welded Ship Structures, *J Ship Prod.* 1999, 15 (02), 73-81.

9. Deng, D.A.; Liang, W.; Murakawa, H. Determination of welding deformation in fillet-welded joint by means of numerical simulation and comparison with experimental measurements, *J Mater Process Technol*, 2007, 183(2–3), 219-225.

10. Ueda, Y.N.; Ma, X. Measuring method of three-dimensional residual stress with aid of distribution function of inherent strain, *Trans Jpn Weld Res Inst* 1994, 23 (1), 123-130.

11. Yuan, M.G.; Ueda, Y. Prediction of residual stresses in welded T- and I-joints using inherent strains, *J Eng Mater Technol*. 1996, 118 (2), 229-234.

PARAMETRICAL OPTIMIZATION OF SANDWICH STIFFENING BARS USED IN A HEAT PUMP DEVICE

A.A. Ancuta[1*], G.G. Jiga[1], M. Costea[2]

[1] *Strength of Materials Department, University POLITEHNICA of Bucharest, Splaiul Independentei nr. 313, Sector 6, Bucharest, Romania, RO-060042*

[2] *Robots and Manufacturing Systems, University POLITEHNICA of Bucharest, Splaiul Independentei nr. 313, Sector 6, Bucharest, Romania, RO-060042*

[*] *Corresponding Author: andrei.ancuta2210@upb.com*

ABSTRACT

In the present paper the authors proposed a study on the identification of the optimum variant of a sandwich structure with the purpose of replacing the bulk steel stiffening bars to obtain a lighter and a cheaper structure for a heat pump device. The material variants proposed for the sandwich structure consists in a core of plastic materials such as ABS [1] or PLA [2] and two skins made of metallic materials such as aluminium or mild steel. The optimization process doesn't just refer to the materials but also to the number of cells and thickness of the pattern infill defining the internal structure, as well as the plate thickness and width. The number of stiffening bars will be also taken into the optimization process. The objective function is to reduce the mass considering two restrictions: a minimum lifetime of 36500 cycles and a safety coefficient of stability equal or higher than four [3].

INTRODUCTION

The present study represents an extension of a previous proposal [4] where the only components which were modified are the stiffening bars. This approach was considered to obtain a lighter and a cheaper structure.

Due to the embedding of these bars in the deformable plate, the struts are loaded as well in compression as in bending. Consequently, there is a tendency for the buckling phenomenon to not occur on the direction with the minimum moment of inertia. For this unique reason, the idea of replacing the bulk material with a sandwich structure was approached.

Regarding the device lifetime, due to the lack of documentation about the proposed device, an indicative value was chosen representing a lifetime of 100 years under the conditions of a single work cycle per day. One year in ANSYS analysis is considered one fatigue block. At its turn, one fatigue block is defined by 365 cycles, each cycle having a minimum and a maximum value, representing a percentage of the static stress, where the value of 36500 cycles comes from.

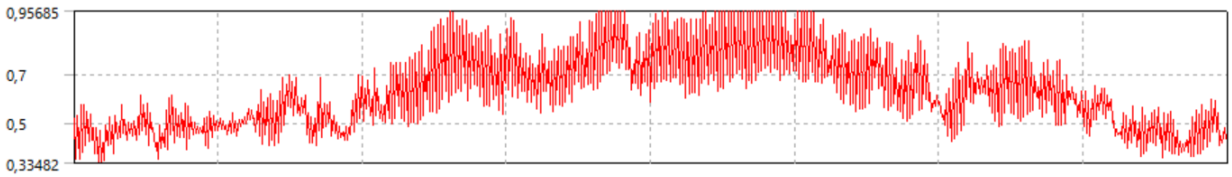

FIGURE 1 The graphic representation of a fatigue block [4]

The fatigue block depicted in Fig. 1 represents the variation of the working fluid pressure on the piston lids, due to the daily change of temperature measured every day over one year. To define this block, daily temperature data with minimum and maximum values for a period of one year were taken from [5]. Using a C++ code, these temperatures were intersected with the pressure-temperature expression of the vapour-liquid curve of the working fluid (CO_2) [6], resulting thus the pressure variation over one year [4].

In Fig. 2 is depicted the proposed structure in reference [4].

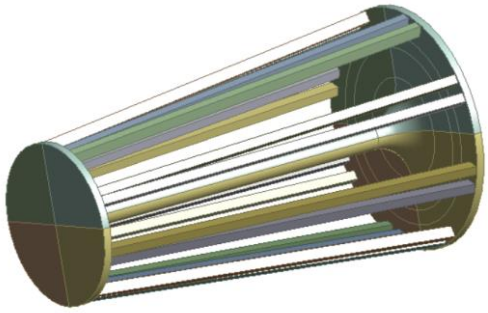

FIGURE 2 The proposed structure in reference.

NUMERICAL ANALYSYS

The numerical analysis is focused on four combinations of skins (Steel + Aluminum) and cores (PLA and ABS). As regards the optimization process, several parameters have been taken into account:

The number of stiffening bars, varying from 3 to 16; The skin plate thickness, varying from 5 to 20 [mm]; A percentage of the maximum width of the sandwich structure, depending on the number of bars and position on the lid; The infill height, varying from 10 to 110 [mm]; The number of infill cells, varying from 2 to 20; The wall thickness of the infill cell, varying from 1 to 380 [mm]; The thickness of the additional stiffening plate from the higher diameter lid, varying from 10 to 100 [mm].

For all these analyses, the authors applied the minimizing criterion of the objective function dependent on the optimization variables.

The authors taken into account a bilinear characterization of the fatigue behaviour for the two specified materials: PLA [7] and ABS [8]. Since the materials included in this study have and yield limit, the criterion taken into account in the FEM model is the Soderberg mean stress theory. In Fig. 3 is depicted the starting model from where this study has been initiated.

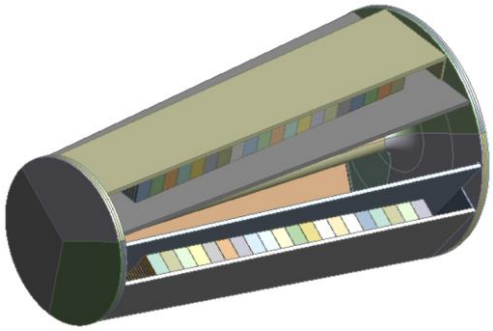

FIGURE 3 Version with 3 stiffening bars of the starting model for the present study.

RESULTS AND DISCUSSION

TABLE 1 Concatenated results

Output parameters	Steel stiffening bars	PLA/ Steel sandwich structure	ABS/ Steel sandwich structure	PLA/ Aluminium sandwich structure	ABS/ Aluminium sandwich structure
Lifetime [cycles]	38061	860925	10^6	10^6	10^6
Max von Mises stress [MPa]	202	282	88	120	82
Buckling safety factor	4.67	4.4	15.1	4.9	6
Stiffening structure total mass [kg]	640.6	703	747	511.6	615.5

CONCLUSIONS

As a conclusion, the identified optimized version for the sandwich stiffening bars structure has aluminum skins and PLA core, it weights a total of 486 kg (10 bars of 48.6 kg each). The entire piston resulted has a buckling safety factor of 4.9 and a theoretically lifetime of 10^6 cycles. The infill core has 2 rectangular cells (on both directions), a 30 mm thick wall, and a height of 90 mm. The resulted auxiliar stiffening plates has 30 mm in thickness. The skins have 80% of the maximum width for this version and a thickness of 18 mm. Overall, the mass of the stiffening structure was reduced by 25%.

REFERENCES

1. Markiz, N.; Horvath, E.; Ficzere, P. Influence of printing directions on 3D printed ABS specimens, *Production Engineering Archives* 2020, 26(3), 127-130.

2. Attoye, S., Malekipour, E., El-Mounayri, H., Correlation Between Process Parameters and Mechanical Properties in Parts Printed by the Fused Deposition Modeling Process, Proceedings of the 2018 Annual Conference on Experimental and Applied Mechanics, Mechanics of Additive and Advanced Manufacturing, Volume 8, pp 35-41.

3. Bambach, M.R. Strengthening of thin-walled (hollow) steel sections using fibre-reinforced polymer (FRP) composites, in: Rehabilitation of Metallic Civil Infrastructure Using Fiber Reinforced Polymer (FRP), Composites, Vistasp M. Karbhari, Ed., Woodhead Publishing, 2014, pp. 140-168.

4. Ancuța, A.A. Dissertation thesis – Proiectarea, optimizarea și verificarea integrității structurale a pistonului unui sistem având rol funcțional de pompă de căldură, July 2023, University POLITEHNICA of Bucharest.

5. Dumitrescu, A., Birsan, M.V., ROCADA: a gridded daily climatic dataset over Romania (1961–2013) for nine meteorological variables. Nat Hazards 78, 2015, pp. 1045–1063.

6.https://encyclopedia.airliquide.com/carbon-dioxide#properties, Accessed May 14, 2022, Thermodynamic properties of the carbon dioxide.

7. Ezeh, O.H., Susmel, L. Fatigue strength of additively manufactured polylactide (PLA): effect of raster angle and non-zero mean stresses, *International Journal of Fatigue* 2019, 126, 319-326.

8. Mura, A.; Ricci, A.; Canavese, G. Investigation of Fatigue Behavior of ABS and PC-ABS Polymers at Different Temperatures, *Materials* 2018, 11(10), 1818; https://doi.org/10.3390/ma11101818.